EFFECTS OF ZINC IMPURITIES ON THE STRUCTURE AND REACTIVITY OF MANGANESE OXIDES

A Dissertation
Presented to
The Academic Faculty

by

Shiliang Zhao

In Partial Fulfillment
of the Requirements for the Degree
Doctor of Philosophy in the
School of Earth and Atmospheric Science

Georgia Institute of Technology
May 2018

EFFECTS OF ZINC IMPURITIES ON THE STRUCTURE AND REACTIVITY OF MANGANESE OXIDES

Approved by:

Dr. Yuanzhi Tang, Advisor
School of Earth and Atmospheric Science
Georgia Institute of Technology

Dr. Martial Taillefert
School of Earth and Atmospheric Science
Georgia Institute of Technology

Dr. Chris Reinhard
School of Earth and Atmospheric Science
Georgia Institute of Technology

Dr. Jennifer Glass
School of Earth and Atmospheric Science
Georgia Institute of Technology

Dr. Mengqiang Zhu
Department of Ecosystem Science and Management
University of Wyoming

Date Approved: March 28th, 2018

ACKNOWLEDGEMENTS

Firstly, I want to express my greatest apprication to my advisor, Dr. Yuanzhi Tang, for her continuous support during my PhD study in the past five years. Without her professional, caring, and enthusiastic mentoring, this study would not have been completed. I would like to thank my committee members, Dr. Martial Taillefert, Dr. Mengqiang Zhu, Dr. Jennifer Glass, and Dr. Chris Reinhard for their time, interests, collaboration opportunities, and helpful recommendations.

Thanks to my lab members, Rixiang, Emily, Ashley, Biao, Pan, Ben, Yaneira, Chenning, Haesung, Nadia, Ci, River, and Weishi for their help in my research. Thanks to Dr. Emily Saad for ICP-MS help and passionate encouragement all the time in the past five years. Thanks to Dr. Rixiang Huang for his help with XAS experiments and inspiring suggestions for my paper writing. This group has been a family to me.

I would also like to thank my research collaborators: Dr. Mengqiang Zhu and his student Qian Wang for Mn XAS data analysis; Dr. Shuo Chen and her student Jingying Sun for HRTEM analysis; Dr. Evert Elzinga for his support in birnessite transformation study; Dr. Hailong Chen for his crystallographic knowledge in Mn oxide structure study; Dr. Chris Reinhard, D. and Dr. Xiangli Wang for Cr isotope work; Dr. Martial Taillefert and his student Eryn Eitel for collaboration in Mn oxide redox reactivity project; Dr. Olaf Borkiewicz for PDF data collection.

Finally, I want to express my deepest gratitude to my family and friends. Especially, I want to thank my mother, Mrs. Chunying Xu, for her unconditional love and understanding throughout my life.

TABLE OF CONTENTS

LIST OF TABLES

LIST OF FIGURES

LIST OF SYMBOLS AND ABBREVIATIONS

ads	Adsorption
AOS	Average oxidation state
BET	Brunauer, Emmett and Teller
bioMnOx	Biogenic Mn oxyhydroxides
CFSE	Crystal field stability energy
cppt/coppt	Coprecipitation
DCS	Double corner sharing
DFT	Density function theory
EXAFS	Extended X-ray absorption fine structure
HRTEM	High resolution transmission electron microscope
INC	Incorporation
^{IV}Zn	Zn tetrahedral complex
MCO	Multi-copper oxidase
Mn oxides	Mn oxyhydroxides
OMS	Octahedral molecular sieves
PDF	Pair distribution function
ROS	Reactive oxygen species
TCS	Triple corner sharing
TES	Triple edge sharing
XANES	X-ray absorption near edge structure
XAS	X-ray adsorption spectroscopy
XRD	X-ray diffraction
^{VI}Zn	Zn octahedral complex

SUMMARY

Manganese (Mn) oxides are among the most ubiquitous and reactive mineral phases in natural environments. They can significantly influence the cycling of critical nutrients (such as carbon and nitrogen), as well as the transport and fate of a wide range of metals and organic contaminants. The structure and reactivity of Mn oxides have been extensively studied. However, most studies used pure Mn oxide minerals, which are not commonly found in geological or engineering settings. Considering the prevalent interactions between metal cations and Mn oxides in the natural environments, it is highly desired to obtain an in-depth understanding on the effects of metal impurities on the structure and reactivity of Mn oxides, which will provide a better understanding of a range of biogeochemical processes involving Mn oxides under complex environmental conditions.

This dissertation systematically explored the effects of Zn coprecipitation on the structure, reactivity, and transformation of biotic and abiotic Mn oxides, and compared these with the effects of Zn sorption on Mn oxides. Among all transition metals that are commonly found to associate with Mn oxides (Co, Ni, Cu, Fe, Zn), Zn is the least compatible with Mn oxide layers, and can cause significant structure modifications in Mn oxides during coprecipitation. This research used a suite of complementary microscopy, spectroscopy, and scattering techniques to probe the changes in Mn oxide surface, morphology, and structure properties, such as surface area, surface charge, particle size, morphology, oxidation state, phase, structural order, vacancy site density, and local coordination environment. Significant Mn oxide structural modifications by Zn coprecipitation were observed, such as decreased particle size, increased average oxidation state, and increased vacancy site density. Based on the observed structure modifications,

controlled laboratory sorption experiments were conducted using cation (Cd) and anion probes (AsO_4^{3-} and PO_4^{3-}) to elucidate the effects of Zn coprecipitation on the sorptive reactivity of Mn oxides. The kinetics and pathways of Mn^{2+}-induced reductive transformation of Zn-coprecipitated Mn oxides were also investigated, in order to assess the long-term stability and reactivity of the oxides. In summary, compared to pure oxide phase, Zn-coprecipitation induced significant structural modifications of Mn oxides, resulting in significantly modified sorptive reactivity, redox reactivity, and transformation kinetics and pathways. Such effects of metal impurities might be common and should also be evaluated for other metals that commonly associate with Mn oxides. The roles of Mn oxides in regulating nutrient, metal, and organic fate and transport, as well as Mn biogeochemical cycling itself, should also be re-visited and take the impacts of metal impurities into consideration.

CHAPTER 1. INTRODUCTION

Manganese (Mn) (oxyhydr)oxides (hereafter referred to as Mn oxides) are commonly found in a large variety of geological and environmental settings, such as soils, marine nodules, hydrothermal deposits, and sediments of fresh lakes and streams [1-3]. Mn oxides can occur as fine-grained particles and coatings of rocks. Due to their high surface area, large amount of vacancy sites, mixed oxidation states, and negative surface charge across a wide range of pH conditions, Mn oxides are highly reactive for the adsorption and/or redox transformation of metals (e.g. Pb, Ni, Cr) [4-7], metalloids (e.g. As, Se) [8, 9], and organic compounds [10, 11], and can exert significant influences on the biogeochemical cycles of many important elements. From the materials chemistry aspect of view, hexagonal phyllomanganates are also important layered octahedral molecular sieves (OMS). The design of OMS with specific composition, structure, and morphology is of great interest to environmental, chemical, and material science research, due to the wide applications of OMS as catalysts, battery electrodes, adsorbents, and semiconductors [12-15].

1.1 Mn cycle in natural environments

1.1.1 Manganese chemistry

Mn can exist in several oxidation states, from 0 to +7, and the most common oxidation states in the natural environments are +2, +3 and +4. Mn^{2+} can be adsorbed on the surface of silicates and metal oxides, complexed with humic substances [16], or precipitate as phosphate and carbonate minerals [17]. Mn^{2+} is thermodynamically stable at low pH and in the absence of oxygen [18]. However, its concentration can also be found to be up to mM level in oxic environments when complexed with ligands [18-20]. Mn(III) is not thermodynamically stable in solutions unless complexed with ligands such as DFOB and

pyrophosphate [19, 21, 22]. Mn(III)-ligand complexes are stable and in some cases can account for the majority of soluble Mn, for example, in suboxic zone in Black Sea and Chesapeake Bay [19, 23]. Mn(III) can exist as adsorbed species on metal oxide surfaces [24, 25], or incorporate into the vacancy sites of Mn oxides and affect the structure and reactivity of Mn oxides [26]. Mn(IV) typically occurs in solid phases and often co-exists with Mn(III), forming a wide range of Mn oxide and (oxy)hydroxide phases, which are important components of soils and sediments [27]. Mn(IV) does not exist in soluble form under neutral conditions [16].

1.1.2 Formation of Mn oxides in natural environments

The oxidation of aqueous Mn^{2+} by oxygen (Figure 1.1), either directly or indirectly, is the primary way of Mn(III/IV) oxide production, and can involve biotic or abiotic processes [18, 28, 29]. Recent study also found fast Mn^{2+} oxidation by the reactive oxygen species generated through nitrate photolysis [30]. Mn^{2+} oxidation by oxygen is thermodynamically favorable but kinetically slow unless under extreme conditions (e.g. boiling temperature, pH over 8) [31, 32] or catalyzed by mineral surfaces and/or microorganisms [28, 29, 33-37]. When catalyzed by mineral surfaces, Mn^{2+} oxidation by oxygen is first order with respect to Mn^{2+}, O_2, and active surface concentrations and second order with respect to OH^- concentration [35, 38]. Different Mn phases have been identified as Mn^{2+} oxidation products, such as hausmannite (Mn_3O_4), feitknechitite (β-MnOOH), manganite (γ-MnOOH), and birnessite (MnO_2) [18, 37, 39, 40].

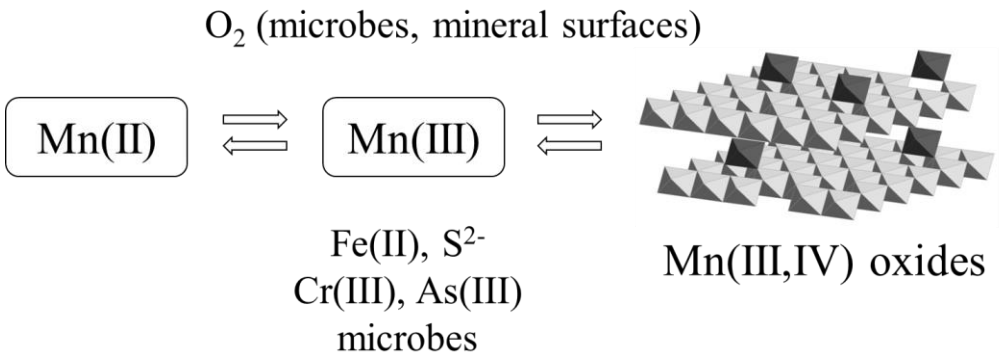

Figure 1.1 Schematic illustration of Mn cycle in natural environments.

Although Mn^{2+} oxidation is accelerated when catalyzed by mineral surfaces, microbe-mediated Mn^{2+} oxidation is several orders of magnitude faster compared to that catalyzed by mineral surfaces [37, 41]. Therefore, natural Mn oxides are typically considered to be biogenic in origin [18, 29, 33, 41]. A range of Mn^{2+} oxidizing bacteria [36, 37] and fungi [25, 29, 42] species were found in a wide range of geochemical environments, including extreme environmental settings such as acid mine drainage (i.e. high acidity) [43] and hydrothermal fluxes (i.e. high temperature) [44]. Despite the diversity of Mn^{2+}-oxidizing bacteria, 16S rRNA gene sequencing showed that all the Mn-oxidizing bacteria belong to the low (Firmicutes) and high (Actinobacteria) G + C Gram-positive and the α-, β-, and γ-Proteobacteria branches [18]. Among all the Mn^{2+}-oxidizers, three model bacteria were most extensively studied: *Leptothrix discophora* SS-1, *Pseudomonas putida* strains MnB1 and GB-1, and *Bacillus sp.* strain SG-1 [25, 41, 45-49]. Different hypotheses have been proposed regarding the physiological reason of microbial Mn^{2+} oxidation, but no consensus have been reached [16].

Microorganisms can participate in the oxidation of Mn^{2+} in direct (i.e. biologically controlled) or indirect (i.e. biologically induced) ways. Microorganisms can change local pH and pE in the aqueous environment, or release metabolic byproducts that are capable of chemically oxidizing Mn^{2+} or catalyzing the process [16, 18]. Multi-copper oxidase (MCO) is the most studied Mn^{2+}-oxidizing enzyme complex. All three model microbes mentioned above have genes that encode this protein that is capable of enzymatic oxidation of Mn^{2+}. Learman et al found superoxide, a type of reactive oxygen species (ROS), produced by marine *Roseobacter* sp. AzwK-3b can also oxidizes Mn^{2+} to Mn oxides extracellularly [36, 50]. In early studies, biogenic Mn oxides produced by *Bacillus sp.* strain SG-1 were mostly Mn(III)-bearing minerals, such as hausmannite [51, 52], despite of the different experimental conditions (i.e. pH 7.5 and 2 μM Mn^{2+} in Hasting et. al 1986 [51], 25 mM Mn^{2+} in Mann et. al 1988 [52]). Later studies have shown oxidation from Mn^{2+} to Mn(IV) by *Bacillus sp.* SG-1 spores without the detection of Mn(III) intermediate solid phases [47, 53]. More recent studies using X-ray adsorption spectroscopy revealed that Mn^{2+} oxidation to Mn(IV) was two subsequent one-electron transfer steps with Mn(III) as an intermediate [41, 54]. The Mn(III) intermediate did not precipitate as solid phases but was trapped by complexing ligands such as pyrophosphate. In several studies with low to medium Mn^{2+} concentrations, the initial phases of biogenic Mn oxides were mostly layered phyllomanganates that are structurally similar to hexagonal δ-MnO_2 or birnessite [28, 34, 36, 37, 55, 56]. The Mn(III)-bearing minerals produced in early studies mentioned above were most likely formed by Mn(IV) minerals reacting with Mn^{2+} [16, 25]. Exception was also found where fungus *Acremonium* sp. KR21-2 produced todorokite-like Mn oxides with a tunneled structure [42]. Co-existing metal cations could affect the structure of biotic Mn oxides. Webb et al identified triclinic

(instead of hexagonal) birnessite formed in the presence of Ca^{2+} [57, 58] and tunneled todorokite-like phase in the presence of uranyl (UO_2^{2+}) [59].

1.1.3 Mn oxide structure

Mn oxide minerals exist in various geological settings but are mostly fine grained and poorly crystalline, making it difficult to characterize their structure [27] . In general, Mn oxides are divided into two categories: 1) layered structure, also named as phyllomanganates, and 2) chain or tunneled structure (Figure 1.2). The basic unit of Mn oxides is MnO_6 octahedron which can share corners and/or edges to form layered sheets or tunneled structure. For tunneled Mn oxides, single units first share edges to construct single (i.e. pyrolusite), double (i.e. hollandite), or triple chains (i.e. todorokite), then chains share corners to form square or rectangle frameworks. Tunneled Mn oxides with different tunnel parameters have different surface area, hydration state, and accessibility of exchangeable cations [18, 27, 28]. Birnessite exhibits two layer symmetries: orthogonal and hexagonal. The latter has more vacancy sites while the former has no vacancies but ordered Mn(III) in the layer structure [18, 26].

Mn oxides contain defects in their structure owing to the absence of Mn(IV) atoms or substitution of Mn(IV) by Mn(III) or other cations (e.g. Co and Ni) with lower oxidation states [14, 60, 61]. To compensate the negative charges caused by the defects, cations such as K^+, Na^+, Mg^{2+}, Ca^{2+}, Cu^{2+}, Ni^{2+} can exist in the tunnels, interlayer region, or edge sites [62, 63]. For layer structured birnessite, relatively small cations such as Zn, Ni, Mn, Co, Ca, Mg are commonly octahedrally coordinated by the O layer bound to the layer vacancies and interlayer H_2O [64]. Cations in the Mn oxides can also affect the stability of the structure. For example, $Mn^{III}O_6$ octahedra are distorted due to the Jahn-Teller effect [65]. In

chalcophanite, the mechanism of layer-layer stabilization is via hydrogen bonding between triple corner sharing Zn^{2+} ions and adjacent layers [66]. Besides cations, water molecules can also exist in the interlayer region of phyllomanganates. For example, phyllomanganates with a 10 Å d-spacing (e.g. lithiophorite) has an extra water layer compared to those with a 7 Å spacing (e.g. birnessite, δ-MnO_2) [18].

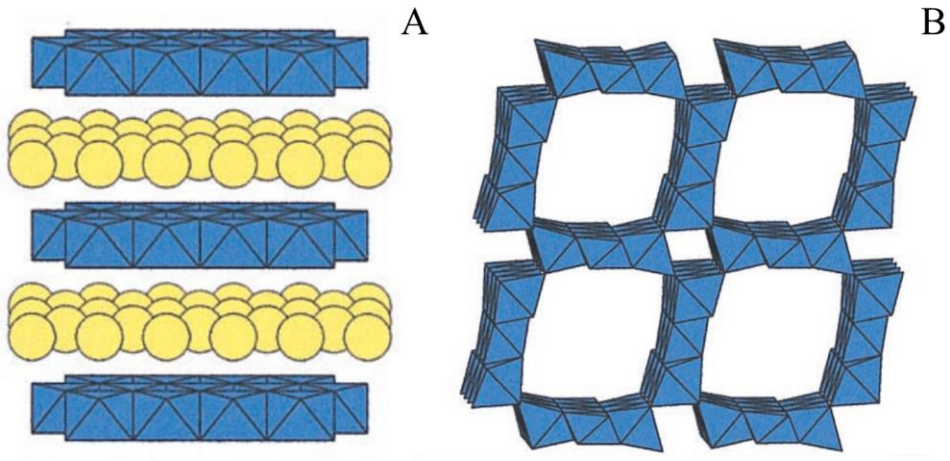

Figure 1.2 Structure of typical layered and tunneled structure of Mn oxides, from Post [67]. A) Na-rich birnessite with Na^+ and H_2O (yellow) within MnO_6 octahedral sheets (blue); B) todorokite with a 2×2 tunneled structure.

1.2 Metal association with Mn oxides

1.2.1 Metal sorption on Mn oxides

Due to the negative surface charge, large surface area, and large amount of vacancy sites, Mn oxides (especially phyllomanganates) have large adsorption capacities toward heavy metals and other trace elements in the soil and aquatic systems [18, 27], and are regarded as "metal scavengers". The adsorption affinity of metal cations on Mn oxides

follows the reverse order of hydrated cation radii [68]. Several studies also revealed the correlation between metal cation affinity and their first hydrolysis constant [69-71]. For example, Zn^{2+} has a smaller ionic radii and acts as a harder Lewis acid than Cd^{2+} [72] and thus has a higher adsorption affinity towards δ-MnO_2.

Metals can interact with Mn oxide surfaces through (1) the formation of inner-sphere triple-corner-sharing (TCS) complexes, or (2) incorporation (INC) into the vacancy sites [73-77] (Figure 1.3). The ratio of INC/(INC+TCS) is metal specific, with Co(III) being 90-100%, Ni(II) 10-45%, Cu(II) 0-20%, and Zn(II) 0% [2, 74, 78]. This ratio was suggested to be dependent on the compatibility of foreign metal ions with the Mn oxides structure, such as metal size/charge similarities to the structural Mn(III)/(IV) ions [14, 61, 79-81]. However, Cu(II) and Zn(II), with only 0.01 Å difference in ionic radii, have 20% difference in their INC/(INC+TCS) ratio. Kwon et al calculated the crystal field stability energy (CFSE) difference for the INC vs. TCS species, and the results were -214, -23, +4 and +34 kJ/mol for Co, Ni, Cu, and Zn, respectively, which correlated better with the INC/(INC+TCS) ratio compared to ionic radii [74]. Solution conditions also affect the incorporation of metals into Mn oxide structure. For example, more Ni(II) and Cu(II) was found to incorporate into birnessite structure at higher pH [58].

In early studies, metal cation sorption on layered Mn oxides were thought to bond to only the vacant sites [2]. More recent studies showed evidences of metal cation adsorption onto the edge sites as well. For example, Pb^{2+} was found to adsorb on the edge sites of biogenic Mn oxides through the formation of triple-edge-sharing (TES) complex [77]. It has been proposed that Zn^{2+} can also adsorb to layered Mn oxide edge sites and affect the further reactions between Mn oxides and other species, such as anion uptake and arsenite

oxidation [62, 63]. Hinkle et al found that Mn(III) occupied vacancy sites during the aging process of phyllomanganates and expelled Ni^{2+} and Zn^{2+} ions to the edge sites [82]. Moreover, Cu^{2+} adsorption on synthetic δ-MnO_2 was found to occur dominantly at edge sites [76]. Considering the nano-scale particle size and large edge area of amorphous biotic and abiotic Mn oxides, the contribution of edge sites in metal uptake by Mn oxides should not be ignored.

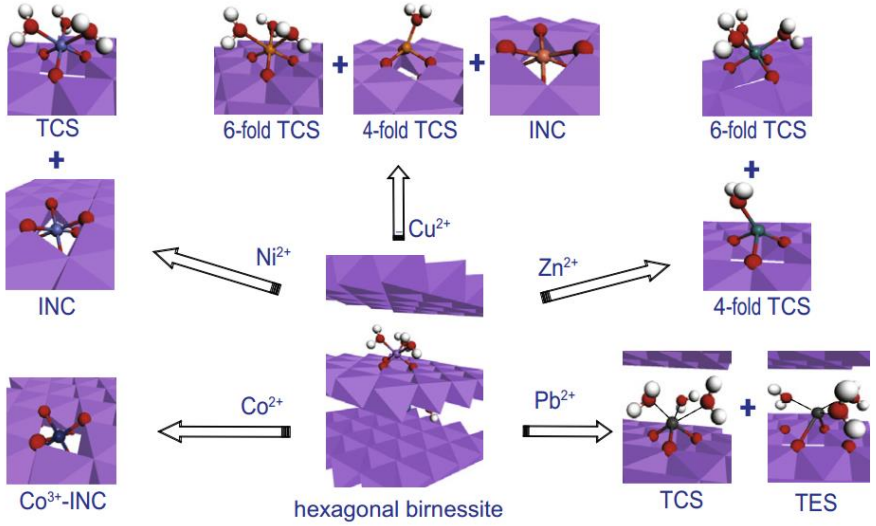

Co(II,III): Manceau et al. (1997).
Ni(II): Manceau et al. (2007); Peacock and Sherman (2007); Peña et al. (2010).
Cu(II): Manceau et al. (2002); Sherman and Peacock (2010).
Zn(II): Manceau et al. (2002); Toner et al. (2006); Kwon et al. (2009a).
Pb(II): Lanson et al. (2002); Kwon et al. (2010).

Figure 1.3 Summary of the structural configuration of adsorbed metal species at hexagonal birnessite vacancy sites, taken from Kwon et al [74]. TCS: triple-corner-sharing surface complex; INC: incorporated at vacancy site; TES: triple-edge-sharing surface complex.

1.2.2 Metal coprecipitation with Mn oxides

Besides metal sorption on pre-formed Mn oxides, several studies have also studied metal coprecipitation with Mn oxides. Chen et al synthesized metal-doped cryptomelane and found that incorporated metal content in the final solids increased in the order of Mg

< Ni ~ Al ~ Zn < Cu < Co [83] , which was correlated to the affinity of these metals to cryptomelane. The coordination environments of coprecipitated metal cations (Ni, Co, Fe, Zn) in synthetic or biogenic layered Mn oxides were found to be the same as their corresponding adsorbed species (i.e. surface complexed and/or incorporated) with no additional phases precipitated [14, 61, 80, 84]. The INC/(INC+TCS) ratio in metal coprecipitation system followed the same trend observed in metal adsorption system: more Co (71–80%) incorporated into birnessite structure compared to Ni (24–34%) due to atomic size/charge difference and CFSE, as discussed above in the metal adsorption section (Section 1.2.1). More metal uptake by Mn oxides was observed during coprecipitation compared to metal adsorption on pre-formed Mn oxides [84, 85], likely resulting from the structural modification of Mn oxides by the coprecipitating metal ions. More detailed discussion on the effect of metal coprecipitation on Mn oxide structure can be found in Section 1.3.2 below.

1.2.3 Metal oxidation by Mn oxides

Mn oxides are among the most redox-active minerals in the environment and can oxidize various organic and inorganic species [67, 86-88]. The standard reduction potential of layered phyllomanganate/Mn(II) (e.g. δ-$Mn^{IV}O_2$/Mn(II) couple, 618 mV) are among the highest Mn oxide/Mn(II) couples [89]. The most prevalent chemical reductants of Mn oxides in the nature are ferrous ion (Fe^{2+}) and hydrogen sulfide [89]. The oxidation of Fe^{2+} by Mn oxides is fast at low pH (<4) and inhibited due to Fe(III) precipitation at higher pH which can block the surface sites [90]. $Mn^{IV}O_2$ can also undergo reductive transformation in the presence of dissolved Mn^{2+} to form other Mn oxides phases. Biotic and abiotic hexagonal birnessite phases can react with low concentration of Mn^{2+} to form triclinic birnessite [25,

[26, 58]. With higher Mn^{2+} concentrations, birnessite can transform to various Mn(II,III)-bearing minerals [47, 91]. Natural organic matters and microbial exudates can also reduce and solubilize Mn oxides [92]. Surface complexation between organics and Mn oxides were thought to form prior to electron transfer [10, 87, 88]. Some organics can promote Mn oxide reduction and stabilize the produced Mn(III) through metal-ligand complexation [93]. In addition to the chemical reduction processes discussed above, Mn oxides can also be reduced by microorganisms (e.g. dissimilatory metal reducing bacteria, DMRB) under anaerobic conditions, which contributes significantly to the degradation of organic carbon [94].

Mn(III,IV) oxides can also oxidize a range of metals and metalloids, such as Se, As, and Cr, thereby influencing metal speciation and related toxicity and bioavailability (Figure 1.1) [18, 67, 95]. For example, Mn oxides are the most important environmental oxidants capable of oxidizing low solubility Cr(III) species to soluble and toxic Cr(VI) species [96-98]. Arsenite can be oxidized by Mn oxides, leading to the formation of As(V) species with lower toxicity [99-103] and high sorption affinity on the oxides, which has found applications in drinking water treatment systems [102].

The oxidation of metals and metalloids by Mn oxides can be affected by many factors, such as pH, ionic strength, and metal concentrations [104]. For example, birnessite can react with Mn^{2+} and produce feitknechtite and manganite (under neutral to alkaline pHs), groutite (at pH 6.0), cryptomelane (at pH 4.0), nsutite and ramsdellite (at pH 2.4) under otherwise the same conditions [47, 91]. High pH favors the adsorption of Cr(III) on negatively charged Mn oxide surface but also can lower the concentration of dissolved Cr(III) [55, 95]. The effects of Mn oxide structure on their redox capability have been

extensively studied, such as surface area, average oxidation state, availability of vacancy sites, and Mn(III) content. For example, Mn(II,III) contents in Mn oxide structure can enhance their oxidation capability towards Cr(III) [6, 105]. Metal cations (e.g. pre-adsorbed Zn [62], released and re-adsorbed Mn^{2+} during redox reaction [61, 62, 106]) were shown to occupy surface sites and slow down oxidation kinetics towards arsenite, Cr(III) and organics [107].

1.3 Effects of metal cations on Mn oxides

1.3.1 Effects of metal adsorption on Mn oxide structure

Adsorbed metal cations can neutralize the surface charge of Mn oxides, which is typically negative over a wide range of pH [18, 29]. Adsorbed Ni [108], Pb, Zn, and Cd [78] can replace interlayer Mn(II) and alkaline cations (such as K^+) but show little influence on the Mn(III,IV) in birnessite layer. Therefore, it was generally assumed that few structural changes would occur during the sorption of non-reductive metals onto Mn oxides. However, Grangeon et al [109] found that the adsorbed Zn expelled the Mn(II, III) on vernadite (δ-MnO_2) surface and interlayer region, increasing average oxidation state (AOS). More interestingly, equilibrium of Zn^{2+} with vernadite caused vernadite dissolution and resulted in a smaller coherent scattering domain size in the a-b plane. The Mn(III) content incorporated in vernadite layer vacancy sites was also reduced by adsorbed Zn leaving more vacancy sites (capped by Zn). These findings have never been observed before in other metal adsorption processes and demonstrated the unique role of Zn in affecting Mn oxide structure.

Redox-active metal cations (such as Co^{2+} and Mn^{2+}) can react with Mn oxides and cause more significant structural changes compared to non-redox active metal cations. For

example, equilibrium of Co^{2+} with acid birnessite caused a higher specific surface area (SSA) and no other obvious changes in crystallinity and morphology [106]. Mn^{2+} reaction with Mn(III, IV) oxides induced various transformation processes to mineral phases causing changes in symmetry (e.g. hexagonal to triclinic [26]), average oxidation state (e.g. from birnessite to manganite [110-112]), and morphology (e.g. from layered to tunneled structure [112, 113]).

1.3.2 Effects of metal coprecipitation on Mn oxide structure

1.3.2.1 Effects of metal coprecipitation on Mn oxide chemical composition

Metal coprecipitation with Mn oxides affects Mn(II, III, IV) contents and Mn AOS, and these effects are metal-specific. Alkaline and alkali metals (e.g. Ca^{2+} and Na^{+}) have sizes that are too large for substitution and can barely affect structural Mn(III/IV) contents in phyllomanganates. Adsorption of Ca^{2+} and Na^{+} is too weak to compete with absorbed Mn(II/III) and thus barely affects adsorbed Mn(II,III) species. However, presence of alkaline metals could stabilize Mn(III) in birnessite layer and favor orthogonal symmetry of biogenic Mn oxides [58].

Regarding transition metals, the effects depend on metal surface complexation and substitution/incorporation behaviors. Fe(III) was found to preferentially substitute for Mn(IV), reducing Mn(IV) amount and causing a decrease in Mn AOS [80, 114, 115]. When Ni interacted with Mn oxides, a portion of Ni was found to substitute for Mn(III), with the rest of Ni competing with Mn(II/III) and forming surface complexed species. These two factors reduced Mn(II, III) contents and increased Mn AOS [61]. Different effects were observed for Co coprecipitation with Mn oxides: 1) Co coprecipitation with acid birnessite resulted in a large decrease of Mn AOS [14] and was attributed to Co substitution for Mn(IV); 2) Co

coprecipitation with cryptomelane [7] and triclinic birnessite [79] increased Mn AOS and was attributed to Co(III) substitution for Mn(III). This implies that Co substitution during coprecipitation might depend on Mn mineral phases. Similar to the case of metal sorption system, coprecipitated metals (e.g. Cu, Co, Ni) were also found to decrease the K^+ content (important for structure stabilization) in cryptomelane tunnels [83] and phyllomanganate interlayer regions [14, 61, 79, 80].

1.3.2.2 Effects of metal coprecipitation on Mn oxide surface properties

Mn oxide surfaces are negatively charged at a wide of pH values due to the absence of Mn(IV) atoms or substitution by atoms with lower oxidation states such as Mn(III) [18]. Several factors can change Mn oxide surface charge during metal coprecipitation: 1) The negative surface charge can be neutralized by the adsorption of metals; 2) Mn(III,IV) substitution by lower oxidation state atoms may generate more negative surface charges; 3) The incorporation of foreign metal cations other than Mn can cause structure modification and generate more vacancy sites [14, 80, 114], thus increasing negative surface charges. The overall effects of these three competing factors are metal-specific and depend on the extent of substitution (i.e. INC/(INC+TCS) ratio) of the involved foreign metal cation.

Specific surface area (SSA) of Mn oxides has commonly been considered as one of the key parameters influencing Mn oxide adsorption and redox reactivities. The SSA by multi-point BET method is related to the particle size and crystallinity of phyllomanganates. Acid birnessite and δ-MnO_2 have similar stacking layered structure, but acid birnessite has a much lower surface area due to larger particle size and better crystallinity (larger layers and more layer stacking along c axis) [34, 63]. Storage conditions can also change BET

surface area, likely due to aggregation. For example, δ-MnO_2 stored at pH 3.6 resulted in a higher surface area (155 m^2/g) than that at pH 8.1 (121 m^2/g) [34]. Metal coprecipitation with phyllomanganates can significantly affected the SSA through the following processes.: 1) metal presence can interrupt the layer stacking and sometimes reduce layer size, resulting in a smaller particle size and increased SSA [61, 79, 80, 84, 109, 115]; 2) Coprecipitated metals can neutralize negative surface charge and decrease crystallinity, thus causing greater aggregation and decreased SSA [61, 79, 80, 84, 109, 115]. These two competing effects are metal-specific, e.g. increased SSA for Fe and Ni coprecipitated birnessite, decreased SSA for V coprecipitated birnessite, and more complicated trend for Co coprecipitated birnessite [14, 61, 80, 81].

1.3.2.3 Effects of metal coprecipitation on Mn oxide bulk structure

In previous studies, coprecipitated transition metals could hinder crystal growth of Mn oxides and decrease Mn oxide crystallinity [48, 58, 85]. Crystallite size calculated using the Scherrer equation from XRD data and direct observation from scanning electron microscope (SEM) showed that metal (Ni, Co, Fe, Cu, Zn, and V) coprecipitated synthetic birnessite and biogenic Mn oxides were thinner vertically compared to pure ones. The presence of foreign metals during Mn oxide formation interrupted the layer stacking along c axis [14, 61, 80, 84, 115]. This is probably because: 1) metals existed above or below vacancy sites and hindered the layer stacking; 2) foreign metals replaced interlayer alkali cations (e.g. K^+) which helped stabilize layer stacking. Compared to the vertical dimension, the characterization of phyllomanganates in *a*-*b* domain (lateral layer structure) was more complicated. Lateral size determination using microscopy (e.g. high-resolution transmission electron microscopy, HRTEM) was difficult due to the heavy aggregation of

phyllomanganates. Grangeon et al used XRD simulations to calculate the coherent scattering domain (CSD) size of layered δ-MnO_2 and found decreased CSD size in *a*-*b* domain of Zn adsorbed δ-MnO_2 [109]. Yin et al related the variation of unit cell parameter *b* to the lateral layer modification caused by Ni, Co, and Fe coprecipitation with acid birnessite [80].

During transition metal coprecipitation with Mn oxides, the interruption of Mn oxide crystallinity depends on the compatibility of metals (i.e. INC/(INC+TCS) ratio) in Mn oxide structure. The extent of birnessite layer collapse caused by metal coprecipitation increased in the order of Co < Ni < Fe, which correlates reversely with the INC/(INC+TCS) ratio of Co > Ni > Fe [14, 80, 116]. The variation of crystallite parameter *b* caused by metal coprecipitation also increased in the order of Co < Ni < Fe [14, 80, 116]. This indicates that metals that can freely incorporate into Mn oxide layer has less effects on the layer structure. Zn shows the least compatibility compared to other transition metal cations and 0% Zn substitution for Mn(III/IV) has been observed [74]. The coprecipitation of Zn is thus expected to significantly affect the Mn oxide layer and interlayer structure and systematic studies are required to explore the possible structure and reactivity modifications.

Vacancy sites due to the absence of Mn(IV) atoms in hexagonal phyllomanganates is one of the key factors making Mn oxides the most reactive phases in the environment. Vacancy sites can be occupied by Mn(III), and layer Mn(III) content has been used to represent vacancy site amount in Mn oxide layers [18, 58, 109]. Liu et al found that vanadium coprecipitation increased vacancy site amount in synthetic birnessite, either because V expelled the Mn(III) within layers or V hindered crystal growth [58, 81, 115]. Mn K-edge extended X-ray absorption fine structure (EXAFS) analysis indicated that Zn

coprecipitated biogenic Mn oxide has lower layer Mn(III) content (e.g. more vacancy sites) compared to pure oxide, although the authors concluded no Mn oxide structural changes [58, 73]. More detailed work is required to examine the effects of Zn coprecipitation on layer Mn(III) content and vacancy sites density.

1.4 Research Justification

Mn oxides are among the most ubiquitous and reactive mineral phases in natural environments and can significantly influence the cycles of essential elements such as C and N, as well as the transport and fate of a wide range of metals [28, 67, 88]. The structure and reactivity of Mn oxides have been extensively studied but most of these studies used pure oxide mineral phases, which are rarely found in geological or engineering settings. Although numerous studies have investigated the adsorption of metal cations on Mn oxides, more understanding is required on the effects of metal coprecipitation on the structure and reactivity of Mn oxides, considering the prevalent interactions between metal cations and growing Mn oxide phases in the natural environments.

Zn is the least compatible in Mn oxide structure among all the heavy metals commonly associate with Mn oxides (e.g. Co, Ni, Cu, Fe, Zn) [2, 74, 78, 117], and can likely cause the greatest structure modifications during coprecipitation with Mn oxides [14, 61, 80]. Zn adsorption on synthetic vernadite caused smaller vernadite layer size and more vacancy sites, which has never been observed during the adsorption of other metal cations, indicating the unique property of Zn [109]. The overall goal of this study is to systematically explore the effects of Zn coprecipitation on the structure, reactivity, and transformation of Mn oxides, and compare with the effects of Zn adsorption system. This dissertation consists of four parts (Figure 1.4), as detailed below.

Chapter 2 addresses the effects of Zn coprecipitation on the structure of synthetic Mn oxides (two biogenic Mn oxide analogs acid birnessite and δ-MnO_2), including chemical composition, surface property, and layer and interlayer structure. The Zn/Mn molar ratio used in this study was 0–0.2, within the range observed in natural environments (0–0.005 in marine nodules and basin soils [118-120], as high as 0.03 in coal mine drainage treatment system, [121] and 0.46 in contaminated sediments [122]). We combined a suite of complementary techniques that are capable of probing mineral surface properties, morphology, and structure orders at various range of scales, including BET surface area analysis, zeta-potential measurements, Zn and Mn X-ray absorption spectroscopy (XAS), X-ray diffraction (XRD), pair distribution function (PDF) analysis of X-ray total scattering, and high-resolution transmission electron microscopy (HRTEM).

Chapter 3 addresses the effects of Zn coprecipitation on the sorptive reactivity of Mn oxides towards both representative cations and anions. Controlled laboratory sorption experiments were conducted (e.g. sorption isotherm, kinetics, and pH edge experiments) using Cd as a cation probe and phosphate and arseante as anion probes. Cd is a toxic metal contaminant and its fate in the environment is strongly influenced by sorption onto metal oxyhydroxides, especially MnOx [68, 123, 124]. Both phosphate and arsenate are important environmental anions, and their fate and transport are strongly influenced by interactions with geomedia [61, 99, 125-130]. Spectroscopy techniques such as XRD and XAS were combined to elucidate the mechanisms of the sorption processes.

Chapter 4 addresses the effects of Zn coprecipitation on the reductive transformation of Mn oxides. With the structural modifications of Mn oxide phases detailed in Chapter 2, Zn coprecipitation can potentially affect Mn cycling by influencing the

reductive aging/transformation process to other phases such as Mn oxides with lower Mn AOS and tunneled structure. The kinetics and pathways of Mn(II)-induced reductive Mn oxide transformation were investigated under oxic or anoxic conditions to examine the long-term stability of Zn coprecipitated Mn oxides. On the other hand, the reductive transformation process (i.e. a redox reaction between Mn oxides and Mn^{2+}), which can also shed light on how Zn coprecipitation would affect the redox reactivity of Mn oxides.

Chapter 5 addresses the effects of Zn coprecipitation on the Zn coordination environment in Mn oxides. Several studies showed that Zn coordination environment in synthetic biogenic or natural Mn oxide samples did not agree well with the trend obtained from Zn adsorption on synthetic Mn oxides [109, 122, 130]. Zn coordination was systematically studied during Zn adsorption or coprecipitation with synthetic and biogenic Mn oxides with different crystallinity, in order to explore the various factors that might affect Zn coordination environment, such as Zn loadings, Zn presence during/after Mn oxide formation (i.e. coprecipitation vs. adsorption), crystallinity, and involvement of microbes. Results from this chapter elucidated how the structural modifications caused by Zn coprecipitation would affect Zn coordination environment in Mn oxides and explained the phenomenon that the portion of octahedrally coordinate Zn was generally low in natural or biogenic Mn oxides.

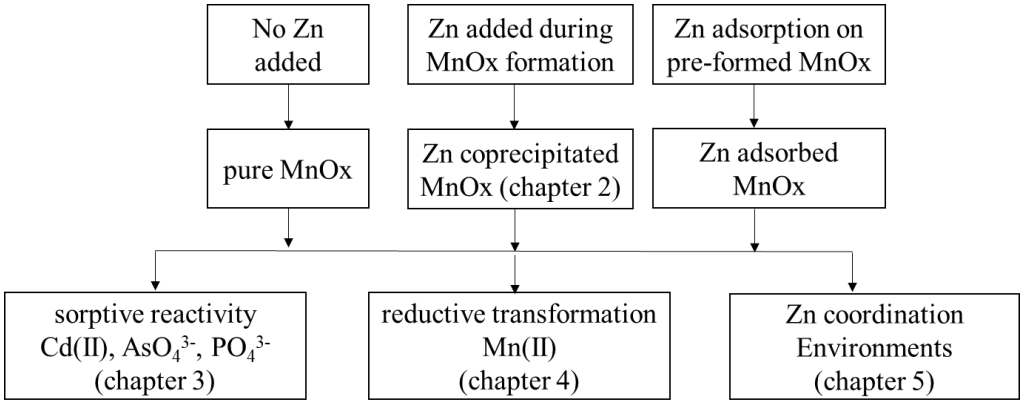

Figure 1.4. Schematic flowchart showing the overall research design.

CHAPTER 2. EFFECT OF ZN PRESENCE DURING MINERAL FORMATION ON THE STRUCTURE OF SYNTHETIC LAYERED MANGANESE OXIDES [1]

2.1 Abstract

Mn oxides, a group of ubiquitous metal oxides in the environment, significantly affect the biogeochemical cycles of metals, nutrients, and organic and inorganic contaminants. Due to their negative surface charge across a wide range of environmental conditions, metal cations have strong affinities for Mn oxides, and the presence of metal cations during or after the formation of Mn oxides significantly affects their structure and properties. This study systematically investigates the effects of Zn presence during mineral formation (i.e. coprecipitation) on the structure of acid birnessite and δ-MnO_2, two synthetic analogs that are structurally similar to fresh biogenic Mn oxides but with different crystallinity. For both acid birnessite and δ-MnO_2, Zn existed as surface adsorbed species at vacancy sites, interrupted layer stacking along *c* axis, and caused reductions of the lateral particle size. Zn also reduced the Mn(III) contents in δ-MnO_2 layers, leaving more vacancy sites (capped by adsorbed Zn). The reduction of layer stacking was more obvious for acid birnessite, while the modification of layer structure was more significant for δ-MnO_2. These structural changes will likely lead to modified reactivity of Mn oxides in natural systems.

2.2 Introduction

[1] Shiliang Zhao, Qian Wang, Jingying Sun, Olaf J. Borkiewicz, Rixiang Huang, Emily M. Saad, Ben Fields, Shuo Chen, Mengqiang Zhu, Yuanzhi Tang. Effects of Zn^{2+} presence during mineral formation on the structure of layered Mn oxides. *Chemical Geology*. Under review.

Mn oxides are a group of metal oxides that are ubiquitous in nearly all environmental settings, such as fresh waters, marine nodules, soils, and sediments [122, 131, 132]. Mn oxides can form through the oxidation of Mn^{2+} and this process is much faster when catalyzed by mineral surfaces or microorganisms. Previous studies have shown that the initial biogenic Mn oxides phases produced by bacteria [36, 37] and fungi [25, 42] at circumneutral pH are typically highly disordered and nanocrystalline phases that are structurally similar to hexagonal phyllomanganates (e.g. acid birnessite and δ-MnO_2) [18]. Due to their high surface area, large amount of vacancy sites, and negative surface charge across a wide range of pH conditions, Mn oxides are highly reactive for the adsorption and redox transformation of metals (e.g. Pb, Ni, Cr) [4-7], metalloids (e.g. As, Se) [8, 9], and organic compounds [10, 11], and can exert significant influences on the biogeochemical cycles of many important elements. From the materials chemistry aspect of view, hexagonal phyllomanganates are also important layered octahedral molecular sieves (OMS). The design of OMS with specific composition, structure, and morphology is of great interest for environmental, chemical, and material science research, due to their wide applications as catalysts, battery electrodes, adsorbents, and semiconductors [12-15].

Metal cations such as Ni^{2+}, Co^{2+}, Cu^{2+}, Pb^{2+}, and Zn^{2+} can either be adsorbed onto and/or incorporated into the layer vacancies and edge sites of birnessite [76, 77, 133-135]. Adsorption of non-redox sensitive metals on Mn oxides was shown to have limited effects on Mn oxide layer structure [62, 63] (except a recent study on Zn sorption [109], as discussed later). Although numerous studies have examined the sorption and/or incorporation of metal cations on pre-formed Mn oxides (i.e. sorption system), much remain unknown on the impact of metal cation presence during Mn oxide formation (i.e. coprecipitation system)

on the oxide structure, reactivity, and transformation, despite the obvious relevance in complex environmental settings. Several recent studies demonstrated significant impacts of metal coprecipitation on the structural properties of Mn oxides, such as Mn(II, III) contents, vacancy site density, crystallinity, thermal stability, and surface area [14, 61, 79-81, 106, 107, 136]. For biogenic phyllomanganates, the presence of Ni can enhance vacancy site formation while Ca^{2+} and Na^{+} were shown to stabilize layer Mn(III) [58]. For abiotic hexagonal birnessite, coprecipitation of Ni, Co, Fe, and V were found to modify the surface area, layer stacking, oxidation states, and coherent scattering domain size of Mn oxides [14, 61, 81, 136]. These influences were shown to be metal specific and dependent on the compatibility of foreign metal ions with the Mn oxide structure, such as size/charge similarities to the structural Mn(III)/(IV) ions and crystal field stability energy (CFSE) [14, 61, 79-81]. The degree of compatibility and amount of metal ion incorporation increase in the order of Zn < Cu < Ni < Co and their impact on structure modification is in the reverse order [14, 61, 80]. These modified structural properties led to differences in adsorptive capacities towards metal cations (Pb^{2+}, Zn^{2+}) [7, 81, 106, 116, 136] and anions (AsO_4^{3-}) [63], oxidative abilities, as well as catalytic [137, 138] and electrochemical properties [115].

Among all the transition metals (e.g. Pb, Co, Ni, Cu, Fe, Zn) that were found to associate with Mn oxides in natural environments, Zn shows the least structural compatibility [14, 61, 74, 80]. Zn was not found to incorporate at the layer vacancy sites of synthetic or biogenic birnessite, but was predominantly adsorbed above/below the vacancy sites. Interestingly, the coordination environment of Zn on Mn oxides was dependent on Zn concentration as well as Mn oxide crystallinity [109]. Tetrahedrally coordinated Zn (Zn^{IV}) at low Zn concentrations can change to octahedral coordination (Zn^{VI}) with increasing Zn

loading [2, 139, 140]. A recent study showed that adsorbed Zn can reduce the Mn(III) ions in δ-MnO_2 layers, leaving more vacancy sites (capped by adsorbed Zn) [109]. Zn adsorption also causes the dissolution of birnessite and results in smaller coherent scattering domain size in the *a-b* plane as calculated by X-ray diffraction (XRD) fitting [109]. Only two previous studies have examined the effect of Zn coprecipitation on Mn oxide structure, but no consensus was reached. Yu et al found that the presence of Zn during the formation of fungal Mn oxides inhibited the crystal growth and modified the layer stacking of Mn oxides [84]. Boonfueng et al found that the presence of Zn during biogenic Mn oxide formation resulted in large Zn sequestration (likely due to surface sorption), but with no obvious changes in Mn oxide local structure [73]. Given the low compatibilities of Zn with phyllomanganate structure, as well as its unique dependence of coordination environment on phyllomanganate crystallinity, a systematic study is highly desired to reveal the impact of this environmentally abundant element on the composition, surface properties, morphology, structural properties, as well as subsequent reactivity (e.g. sorptive, redox) of Mn oxides.

This study examines the impact of Zn coprecipitation on the structural properties of two phyllomanganates with different structural order, acid birnessite and δ-MnO_2. Zn association with natural Mn oxides was found to be 0–0.5% (Zn/Mn molar ratio) in Sicilian [118] and New Zealand marine nodules [119] and Mississippi Basin soils [120]. This ratio can reach 3% in coal mine drainage treatment systems where Mn^{2+}-oxidizing microbes thrive [121], and can be as high as 46% in contaminated sediments [122]. With the high affinity of Zn to Mn oxides, this ratio can be even higher locally [8]. Since Zn sequestration is known to be affected by phyllomanganate structure and crystallinity, we compared acid birnessite

and δ-MnO_2, two structurally similar phyllomanganate phases but with different structural order. Compared to δ-MnO_2, acid birnessite has better crystallinity, more layer stacking along *c* axis, larger layer dimension, and lower surface area [34, 67, 141]. Because Zn octahedral (Zn^{VI}) stabilization is weaker between incoherently stacked and laterally smaller layers [142], its prevalence on δ-MnO_2 was shown to be two times lower than on acid birnessite at similar Zn/Mn loadings [84, 109]. Therefore, it is possible that Zn coprecipitation can have different effects on the structural properties of these two Mn oxide phases with different crystallinity.

Compared to previous studies on Zn sorption on pre-formed Mn oxides [73, 109], in this study Zn was added during the formation of Mn oxides (i.e. Zn coprecipitation). Although Zn was also found to exist as surface adsorbed species in this coprecipitation system (details in results section), more significant effects were observed on the Mn oxide structure compared to Zn sorption systems. By exploring two synthetic Mn oxide phases with similar structure but different structure order, our system eliminated the potential toxicity effects associated with biogenic Mn oxide systems, and allowed thorough investigation on the effect of Mn oxide structure order. We conducted thorough and systematic characterization of the Zn-coprecipitated Mn oxide phases, by combining a suite of complementary techniques that are capable of probing mineral surface properties, morphology, and structure orders at various ranges, including BET surface area analysis, zeta-potential measurements, Zn and Mn X-ray absorption spectroscopy (XAS), X-ray diffraction (XRD), pair distribution function (PDF) analysis of X-ray total scattering, and high resolution transmission electron microscopy (HRTEM). Information obtained from this study provides an overall view of the impacts of Zn coprecipitation on the structural

properties of two environmentally relevant Mn oxide phases, and points to the importance of considering metal coprecipitation effects for studies centered on Mn oxide reactivity in natural systems.

2.3 Methods

2.3.1 Synthesis of δ-MnO_2 and acid birnessite in the presence of Zn

Both δ-MnO_2 and acid birnessite phases were synthesized in the absence or presence of a range of Zn concentrations. δ-MnO_2 synthesis followed a previous procedure [141] where 160 mL $MnSO_4$ solution (0.30 mol L^{-1}) was pumped into a mixture of 160 mL $KMnO_4$ (5.0 g) and 180 mL NaOH (3.5 g) solutions at a speed of 25 mL min^{-1} under vigorous stirring. Calculated amounts of $ZnSO_4$ was dissolved in the $MnSO_4$ solution to achieve Zn:total Mn molar ratio of 0–20%. For acid birnessite synthesis, $ZnSO_4$ was dissolved in 45 mL of 6 mol L^{-1} HCl solution to achieve Zn/total Mn molar ratio of 0–20%. This solution was then pumped at 1 mL min^{-1} into 300 mL of boiling 0.667 mol L^{-1} $KMnO_4$ solution under vigorous stirring [34]. Previous studies on Mn oxide formation in the presence of Zn used Zn/Mn ratios of ~1–22% [84]. After synthesis, the suspensions were cooled down (for birnessite) and the solid precipitates vacuum filtered (0.2 μm), rinsed with deionized (DI) water, dialyzed, and freeze-dried. Samples were labeled according to the starting Zn/Mn molar ratio and are referred to as pure or Zn coprecipitated samples (see Table 2.1 for details). A portion of the dried solids was digested by aqua regia and analyzed for elemental composition using inductively coupled plasms – mass spectrometry (ICP-MS). Samples were also characterized for their morphology, surface, and structure properties using BET surface area analysis, zeta potential analysis, HRTEM, XRD, PDF,

and XAS, as detailed below and in APPENDIX A. Supplementary materials for chapter 2 Text A1-A6.

2.3.2 X-ray adsorption spectroscopy analysis

Mn and Zn K-edge XAS data were collected on both pure and Zn-coprecipitated birnessite and δ-MnO_2 to investigate their structural characteristics. Suspensions containing Mn oxides were vacuum filtered through 0.2 μm polycarbonate membranes and rinsed with DI water. The moist filter membranes loaded with Mn oxide wet pastes were mounted in an acrylic sample holder covered with Kapton tape. Samples were stored at -20 °C and thawed prior to analysis. XAS data were collected at Beamline 4-1 of the Stanford Synchrotron Radiation Lightsource (SSRL; Menlo Park, CA) using Si (220) monochromator and Beamlines 5-BM-D and 12-BM-B at the Advanced Photon Source (APS; Argonne National Laboratory, Lemont, IL) using Si (111) monochromators, all with 40% detuning to avoid higher order harmonics. Energy calibration used Mn or Zn foil. XAS data were collected in both transmission and fluorescence mode using a Lytle detector (Beamlines 4-1 at SSRL and 12-BM-B at APS) or a vortex detector (Beamline 5-BM-D at APS). Both XANES (X-ray absorption near edge structure) and EXAFS (extended X-ray absorption fine structure) data were collected. Two to six scans were collected and averaged. Analysis of the Mn XANES spectra for each sample showed no photo-reduction of Mn oxides under the X-ray beam.

XAS data analysis was performed using the programs SIXPACK [143], Ifeffit [144], and WINXAS [145]. Linear combination fitting (LCF) of the Mn XANES region was conducted to determine the relative percentage of Mn(II), Mn(III), and Mn(IV) species and the average oxidation state (AOS), using reference compounds $MnSO_4$(aq), $MnPO_4$,

ramsdellite, and KBr and following the method described in Manceau et al [146]. Shell by shell fitting was also conducted for both Mn and Zn EXAFS spectra to elucidate local coordination structures.

2.4 Results

2.4.1 Chemical compositions

Composition analysis of the Zn-coprecipitated Mn oxides showed significant amount of Zn sequestration by the oxides (Table 2.1). Zn/Mn molar ratio in the final solids increased with increasing values of initial Zn/Mn ratio. However, under 20% Zn/Mn starting condition, acid birnessite was only able to sequester ~16% Zn/Mn, as compared to ~21% for δ-MnO_2. This higher Zn uptake capacity of δ-MnO_2 might be due to its intrinsic structural properties, as discussed later.

The presence of Zn significantly decreased the interlayer cation (K^+) content for birnessite, but has little impact on the content of interlayer cations (K^+ and Na^+) of δ-MnO_2 (Table 2.1). Total Mn content was relatively stable for birnessite or δ-MnO_2 at different Zn loadings, except for a slight decrease at 20% Zn/Mn loading for acid birnessite. This suggests that Zn might have preferably replaced the interlayer cations in acid birnessite instead of substituting for Mn(III, IV) ions within the MnO_6 layers. This is consistent with previous studies where no Zn substitution into the layer structure was observed when Zn was sorbed on Mn oxides or was present during biogenic Mn oxide formation [2, 84].

Table 2.1 Sample label, chemical composition, BET surface area, HRTEM revealed numbers of stacking layer per particle, as well as XRD determined crystallite size along *c* axis for the Zn coprecipitated birnessite and δ-MnO_2 samples.

Initial Zn/Mn molar ratio	Sample label	Chemical composition of the final solids					BET specific surface area (m^2/g)	Number of stacking layers (by HRTEM)	Crystallite size along *c* axis (nm, by XRD)
		Mn (wt%)	Zn (wt%)	K (wt%)	Na (wt%)	Zn/Mn molar ratio			
Acid birnessite									
0	p-bir	45.2	0	10.5	-	0	27.4±0.4	11±3	6.4
1%	1Zn-bir	44.9	0.6	9.5	-	1.1%	30.2±0.5	11±3	6.7
5%	5Zn-bir	45.9	2.9	8.1	-	5.7%	32.5±0.3	9±4	5.6
10%	10Zn-bir	43.8	6.0	4.9	-	12.4%	29.2±0.2	7±2	5.1
20%	20Zn-bir	43.3	8.0	1.4	-	15.9%	19.3±0.2	5±1	4.5
δ-MnO_2									
0	p-dMn	37.2	0	1.0	2.0	0	221.9±1.3	5±1	-
1%	1Zn-dMn	37.4	1.3	1.7	1.7	2.2%	159.2±1.0	5±1	-
5%	5Zn-dMn	38.3	2.4	2.1	1.8	4.2%	123.9±0.7	5±1	-
20%	20Zn-dMn	37.3	9.8	2.1	1.2	21.2%	131.6±1.0	4±1	-

2.4.2 Morphology of Mn oxides as revealed by HRTEM

HRTEM images revealed significant morphological modifications of Zn coprecipitated birnessite and δ-MnO_2 phases, as compared to their pure phases (Figure 2.1 and Figure A.1). Birnessite samples in general contain larger particles with multiple layer stacking along the *c* axis, while δ-MnO_2 samples show much limited layer stacking and smaller lateral particle size along the *a*-*b* plane. All phases aggregate heavily with curling features, and the aggregation was enhanced by Zn-coprecipitation, consistent with BET surface area measurements showing decreased surface area with increasing Zn/Mn value (Table 2.1). All δ-MnO_2 samples showed more intense curling morphology compared to acid birnessite samples.

In general, the presence of Zn caused less layer stacking and smaller lateral layer size. The numbers of stacking layers along *c* axis for each sample are summarized in Table 2.1. Pure δ-MnO_2 sample contained 5 ± 1 layers and acid birnessite 11 ± 3 layers. With increasing Zn/Mn ratio, layer stacking decreased dramatically from 11 ± 3 to 5 ± 1 for acid birnessite and from 5 ± 1 to 4 ± 1 for δ-MnO_2. It was difficult to quantitatively measure the lateral particle size from HRTEM images due to strong aggregation, but a general decrease in lateral particle size in the presence of Zn was observed in all acid birnessite and δ-MnO_2 samples (Figure 2.1 and Figure A.2).

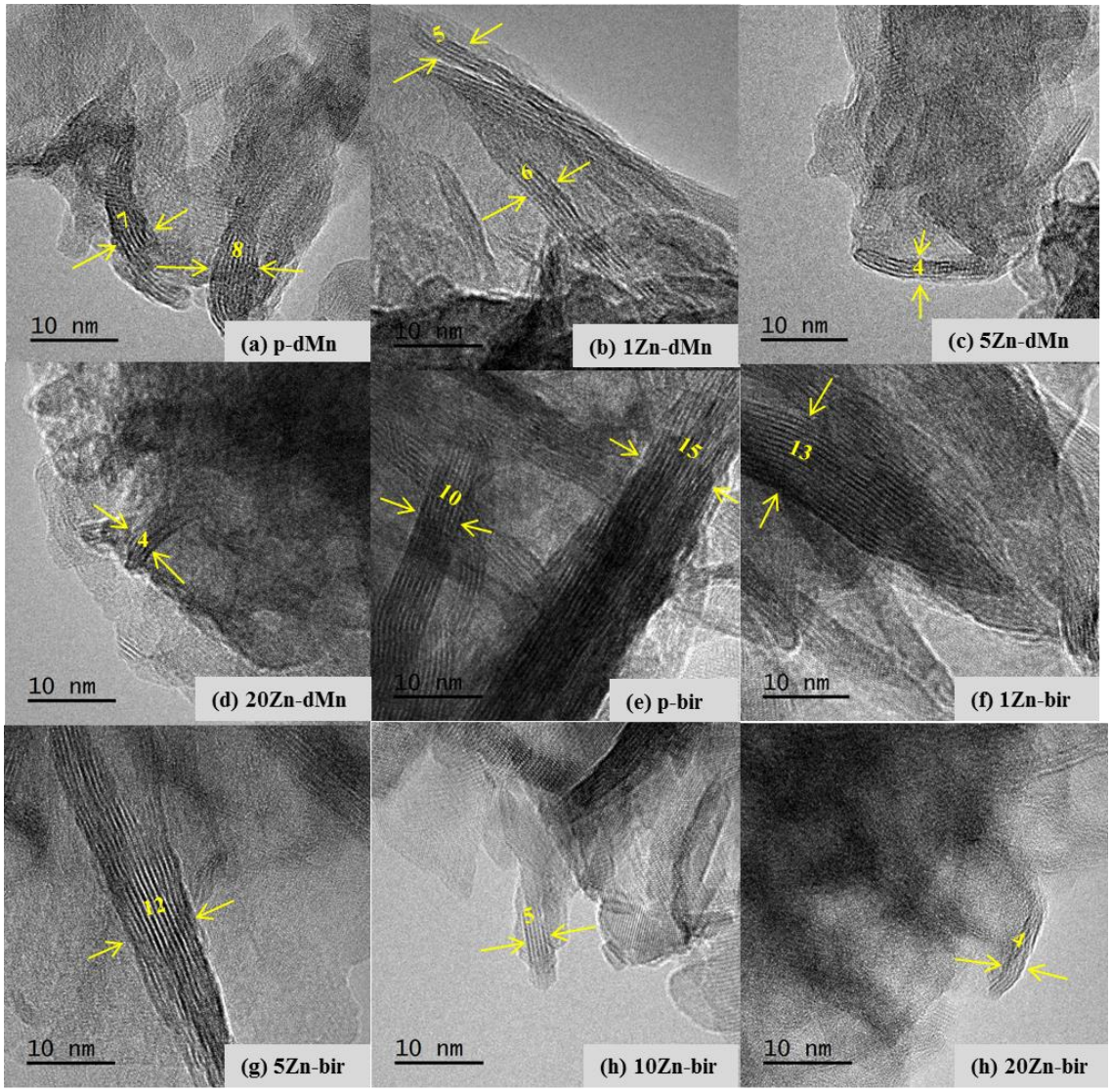

Figure 2.1 HRTEM images of pure and Zn coprecipitated δ-MnO_2 and birnessite samples. (a) p-dMn (b) 1Zn-dMn, (c) 5Zn-dMn and (d) 20Zn-dMn for δ-MnO_2; (e) p-bir (f) 1Zn-bir, (g) 5Zn-bir, (h) 10Zn-bir and (i) 20Zn-bir for acid birnessite.

2.4.3 Surface properties

BET specific surface area (SSA) is a commonly used parameter for evaluating Mn oxide adsorption and oxidation capabilities. In this study, the SSAs of pure acid birnessite and δ-MnO_2 were 27.4 and 221.9 m^2/g, respectively (Table 2.1), consistent with previously reported values of 19–40.5 m^2/g for acid birnessite and 114–274 m^2/g for δ-MnO_2 [62, 63, 80, 138]. For acid birnessite, with increasing Zn/Mn ratio, SSA first increased from 27.4 (p-bir) to 32.5 (5Zn-bir), then decreased to 19.5 m^2/g (20Zn-bir). SSA can be affected by many factors including crystallite size and aggregation. Reduction in both layer stacking and lateral layer size decreases crystallite size and increases surface area. However, surface area also decreases with increasing aggregation [14, 80, 138, 147]. As previously observed [12, 14] and discussed above, Zn presence caused greater aggregation and decreased crystallinity. The net effect of these two competing factors likely accounted for the overall trend of SSA in acid birnessite. For δ-MnO_2, increasing Zn/Mn ratio caused a continuous decrease of the SSA from 221.9 (p-dMn) to 131.6 m^2/g (20Zn-dMn), suggesting aggregation to be the dominant factor affecting SSA in the δ-MnO_2 system.

The presence of Zn also affected the surface charges of Mn oxides (Figure A.1), a critical factor controlling the sorption and redox reactions of metals, metalloids, and organics with Mn oxides [62, 63, 148]. Mn oxides synthesized in this study had negative zeta potentials even at pH as low as 2–3. The presence of Zn caused these values to become less negative, likely at least partially due to the formation of Zn inner-sphere complexes on the oxide surfaces because Zn has strong tendency to sorb on Mn oxides and low compatibility for structural incorporation into Mn oxides. Similar effects on surface charge were also previously observed during Zn adsorption onto birnessite [62].

2.4.4 X-ray diffraction

XRD analysis was conducted to characterize the long-range order of all acid birnessite and δ-MnO_2 samples (Figure 2.2). The patterns for pure acid birnessite and δ-MnO_2 both agreed well with previous studies [83, 141] and showed no presence of any additional phases. For all acid birnessite and δ-MnO_2 phases (pure and Zn-coprecipitated), the d-spacing ratio of the peaks at 2.41 Å (11, 20) and 1.41 Å (31, 02) was 1.71, close to $\sqrt{3}$, indicating a hexagonal layer symmetry [64]. All δ-MnO_2 phases showed no obvious peak at ~7.23 Å (001) and only a broad peak at ~3.68 Å (002), due to the weaker layer stacking of δ-MnO_2 along *c* axis compared to the acid birnessite phases. This is consistent with previous studies [24, 109] and our HRTEM observations. Full width at half maximum (FWHM) of the (001) peaks for all acid birnessite samples was measured and the crystallite size along *c* axis was calculated using the Scherrer equation (Table 2.1). The presence of Zn had more effects on vertical layer stacking for birnessite phases, while δ-MnO_2 phases are more affected in lateral layer size.

For birnessite phases, the presence of Zn caused significant reduction in layer stacking. With increasing Zn content, XRD showed decreased peak height and increased peak width at 7.23 Å (00l) and/or 3.62 (002) reflections, suggesting decreased crystallinity and less layer stacking along the *c* axis, consistent with HRTEM observations. The vertical crystallite size calculated using Scherrer's equation also showed decreasing values with increasing Zn contents (Table 2.1). Reduced layer stacking was also observed before in Ni, Co, Fe and P doping birnessite samples [14, 61, 80, 138]. As shown in the zoomed view (Figure 2.2 C), the hump at 1.6–1.9 Å on the long tailing on the right side of the peaks at 2.41 Å (11, 20) were previously suggested to reflect heavy metal adsorption on vacancy sites [108,

[149]. With increasing Zn content, this hump became more significant due to vacancy site occupation by Zn [108, 149].

For δ-MnO_2 phases, the presence of Zn did not cause significant changes in layer stacking, likely due to the already low numbers of layer stacking as shown in HRTEM and the weak intensity of XRD peaks at 7.23 and 3.62 Å (Figure 2.2 B). At lower d-spacing range (Figure 2.2 D), significantly decrease in peak intensities and increase in peak width were observed with increasing Zn content, suggesting decreased lateral coherent scattering domain (CSD) size [138] caused by the presence of Zn, which was also observed in Fe[80] and P doped Mn oxides[138] This phenomenon is not obvious in our Zn coprecipitated acid birnessite samples.

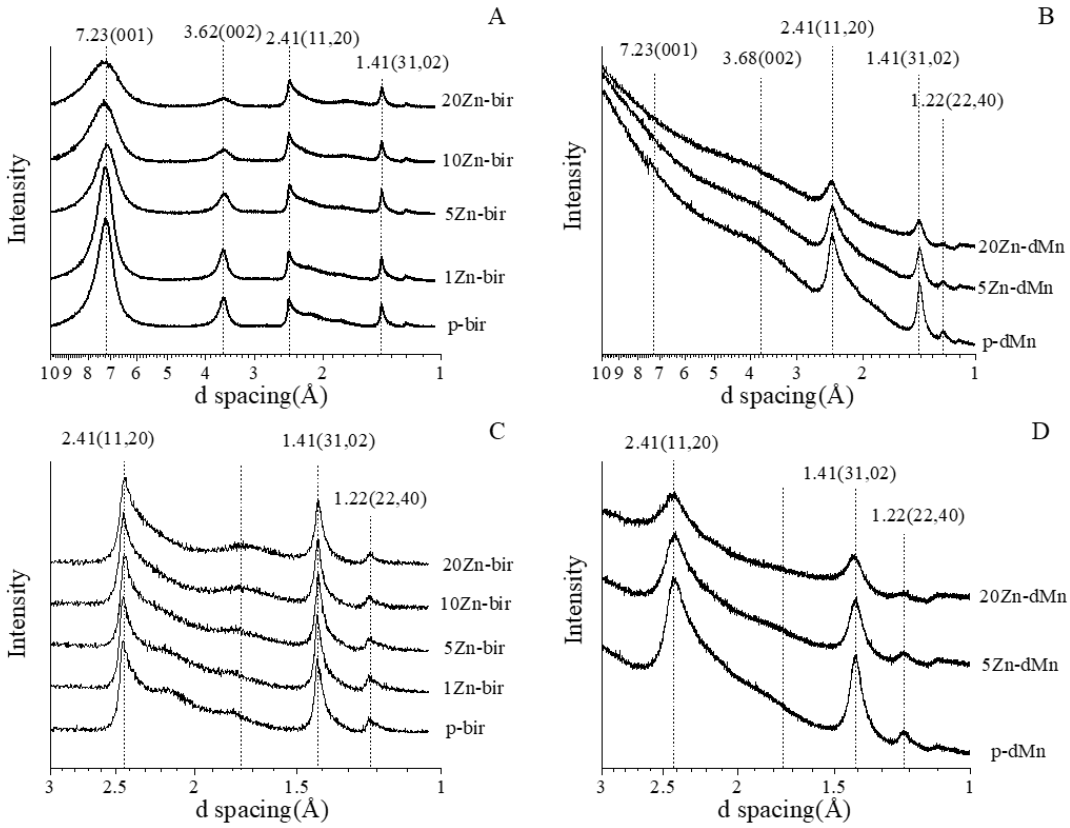

Figure 2.2 XRD patterns of pure and Zn coprecipitated birnessite (A) and δ-MnO_2 (B), as well as their zoomed view at 1–3 Å (C and D, respectively).

2.4.5 X-ray absorption spectroscopy

2.4.5.1 Mn K-edge XANES spectroscopy

Linear combination fitting (LCF) of Mn K-edge XANES spectra was applied to determine the average oxidation state (AOS) and relative contribution of Mn(II), Mn(III), and Mn(IV) species in each sample (Figure 2.3). In several studies, δ-MnO_2 is common standard with an AOS close to 4.0 [24, 34, 150]. Lower values were also reported (3.84 in Webb et al [57], 3.76 in Grangeon et al [109], 3.74 in Grangeon et al [108]) indicating the presence of mixed valence of Mn, i.e., adsorbed Mn(II,III) at vacancy sites and Mn(III) within layers. In this study, pure δ-MnO_2 has an AOS of 3.77 and ~15% Mn(III) contents,

both are similar to the values in Grangeon et al [109]. Compared to δ-MnO_2, pure acid birnessite has a higher AOS (3.92), which is very close to previously reported values, 3.9–4.0 [24, 34, 139, 151]. Less Mn(II,III) contents was observed in acid birnessite compared to δ-MnO_2. For δ-MnO_2 samples, increasing Zn content resulted in the significant decrease of Mn(II) and Mn(III), increase of Mn(IV), thus an overall increase of AOS. The replacement of interlayer Mn(II, III) by exotic cations was also observed during Zn, Pb and Cd adsorption on synthetic phyllomanganates [78, 109]. The AOS of acid birnessite stays relatively stable with increasing Zn, probably due to the already little Mn(II, III) contents in pure acid birnessite and the replacement effects are not significant. Manceau et al compared the LCF results of Mn K-edge XANES with different reference sets and pointed out that reference sets with different structures might result in errors when determining AOS. Fitting with new reference set $MnSO_4$(s), Mn_2O_3 and pyrolusite (MnO_2). The AOS of pure acid birnessite (3.79) and δ-MnO_2 (3.71) are lower than last fitting, confirming that LCF fitting method to achieve Mn AOS largely depends on the reference compounds. In this new fitting, Mn AOS of acid birnessite stays relatively stable and AOS of δ-MnO_2 increased with more Zn added, resembling the trend found in last fitting.

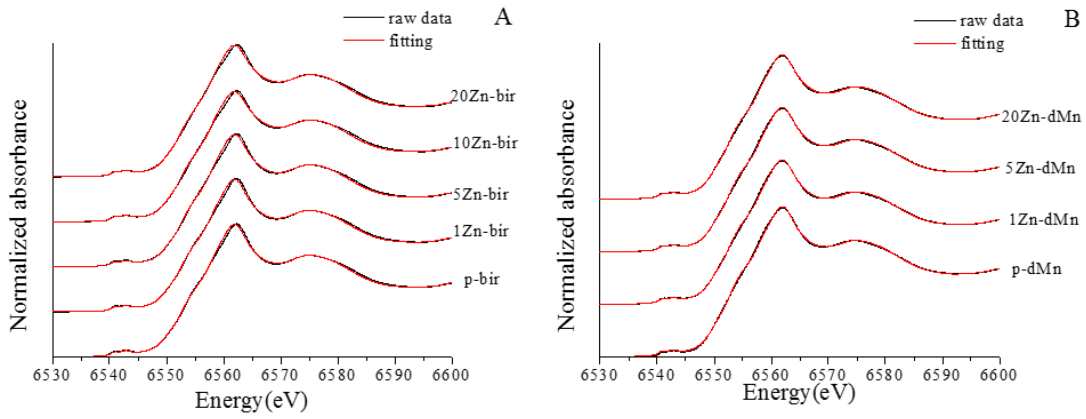

Figure 2.3 Mn XANES spectra (black lines) and linear combination fitting results (red lines) of pure and Zn-coprecipitated acid birnessite (A) and δ-MnO_2 samples (B).

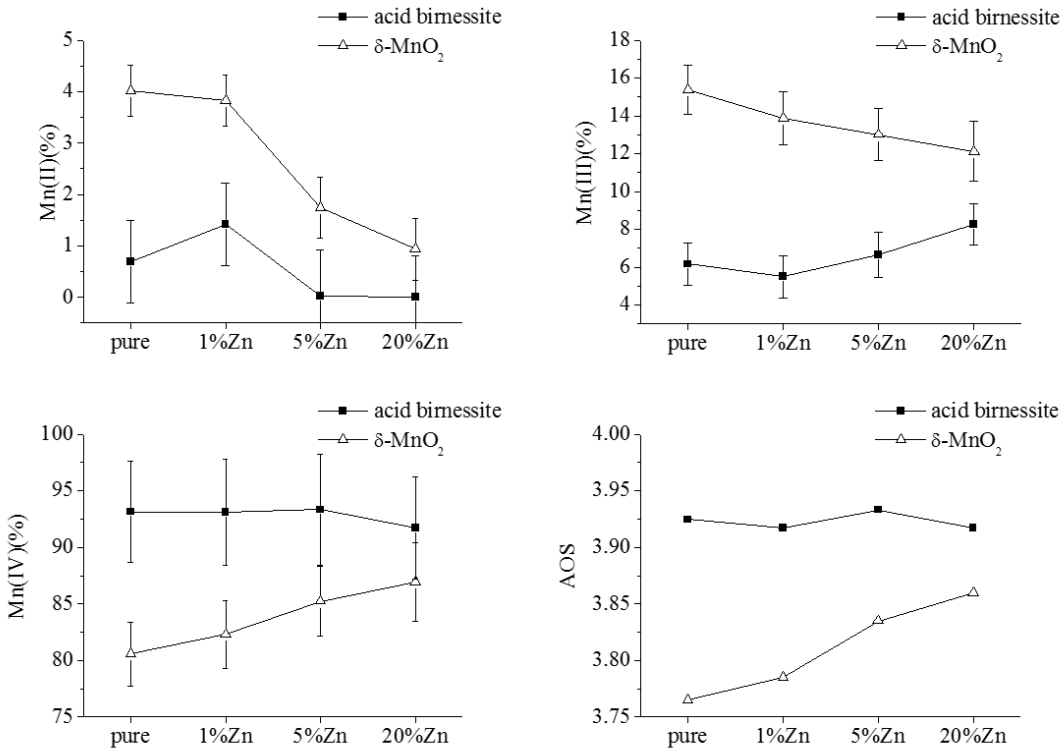

Figure 2.4 Relative percentage of Mn(II), (III), and (IV), as well as average oxidation states (AOS) of pure and Zn coprecipitated birnessite and δ-MnO_2 phases as determined by linear combination fitting of Mn K-edge XANES.

2.4.5.2 Mn K-edge EXAFS spectroscopy

Mn EXAFS spectroscopy was used to elucidate the local coordination environments (e.g. layer structure) of the oxide samples. K^3-weighted EXAFS spectra of pure and Zn-coprecipitated oxides and corresponding Fourier transforms (FT) are shown in Figure 2.5. For Mn EXAFS spectra, the region at ~8–9.2 $Å^{-1}$ (vertical dashed lines in Figure 2.5 A and C) is sensitive to the layer symmetry of Mn oxides. The amplitude of these two peaks decreased while Mn oxides aged from hexagonal to triclinic [26, 37, 55]. Peak broadening (and even splitting) is due to Mn(III) enrichment in triclinic birnessite [130, 152]. Zhu et al also used the sharpness of the two peaks to estimate the layer Mn(III) contents in biogenic Mn oxides [58]. Pure δ-MnO_2 has hexagonal symmetry and little Mn(III) content, and showed sharp peaks in this region (Figure 2.5C) [58]. Pure acid birnessite (Figure 2.5A) showed even sharper peaks compared to pure δ-MnO_2, suggesting the least amount of layer Mn(III) among all samples, which is consistent with the highest AOS measured by Mn XANES analysis (Figure 2.4). With increasing Zn content, the peak at 9.2 $Å^{-1}$ of δ-MnO_2 samples became sharper, suggesting a decrease of layer Mn(III) contents. For Zn-birnessite samples, no obvious changes were observed in this region, and all samples showed sharp peaks indicating low Mn(III) contents.

FT spectra of all samples showed two dominant peaks at ~1.5 and 2.5 Å, corresponding to the Mn-O and Mn-Mn edge-sharing (Mn-Mn_{edge}) shells, respectively. Previous studies suggested the peak height ratio $H_{Mn\text{-}Mn(edge)}/H_{Mn\text{-}o}$ corresponds to several factors such as layer vacancy site occupation fraction(f_{occ}) and particle size [58, 153]. Saratovsky et al found the ratios in layered Mn oxides increase with a larger layer cation occupation fraction[153]. However, several studies found different results from the trend

above when it comes to vacancy occupation by Mn(III) incorporation into layer structure. For example, triclinic birnessite has large amounts of layer Mn(III) occupying vacancy sites and a low ratio of 0.73 (Figure 2.5D). This ratio was 0.82 in pure δ-MnO_2 and 1.01 in pure acid birnessite, both of which have less layer Mn(III) and more unoccupied vacancies compared to triclinic birnessite [18, 26]. The aging process of abiotic [26] and biogenic [37, 55] Mn oxides with Mn(II) results in more vacancy occupation by Mn(III) and decreased $H_{Mn\text{-}Mn}/H_{Mn\text{-}o}$ ratio. Zhu et al found the inverse proportionality between f_{occ} and $H_{Mn\text{-}Mn}/H_{Mn\text{-}o}$ ratio and used this relationship to estimate layer Mn(III) contents in biogenic Mn oxides [58]. The decreased ratio probably attributes to Jahn-Teller distortions caused by layer Mn(III) which splits the Mn-Mn peak and decreased the amplitude [54].

For δ-MnO_2 with Zn addition, decreased particle size could reduce the relative amplitude of Mn-Mn_{edge} peak [4, 57, 138] while less layer Mn(III) in Zn δ-MnO_2 samples could increase the amplitude [57, 58, 154]. In this study, $H_{Mn\text{-}Mn(edge)}/H_{Mn\text{-}o}$ increased slightly from 0.82 (pure) to 0.91 (20Zn-dMn). This indicates the dominating factor is layer Mn(III) decreased by Zn addition as shown both in the k space (Figure 2.5C) and EXAFS fitting results below. The ratio remained relatively stable with increasing Zn content for the acid birnessite system showing relatively stable layer Mn(III) contents. This is also consistent with the unchanged peak sharpness at ~8–9.2 $Å^{-1}$ region in k space and our EXAFS fitting results of acid birnessite below.

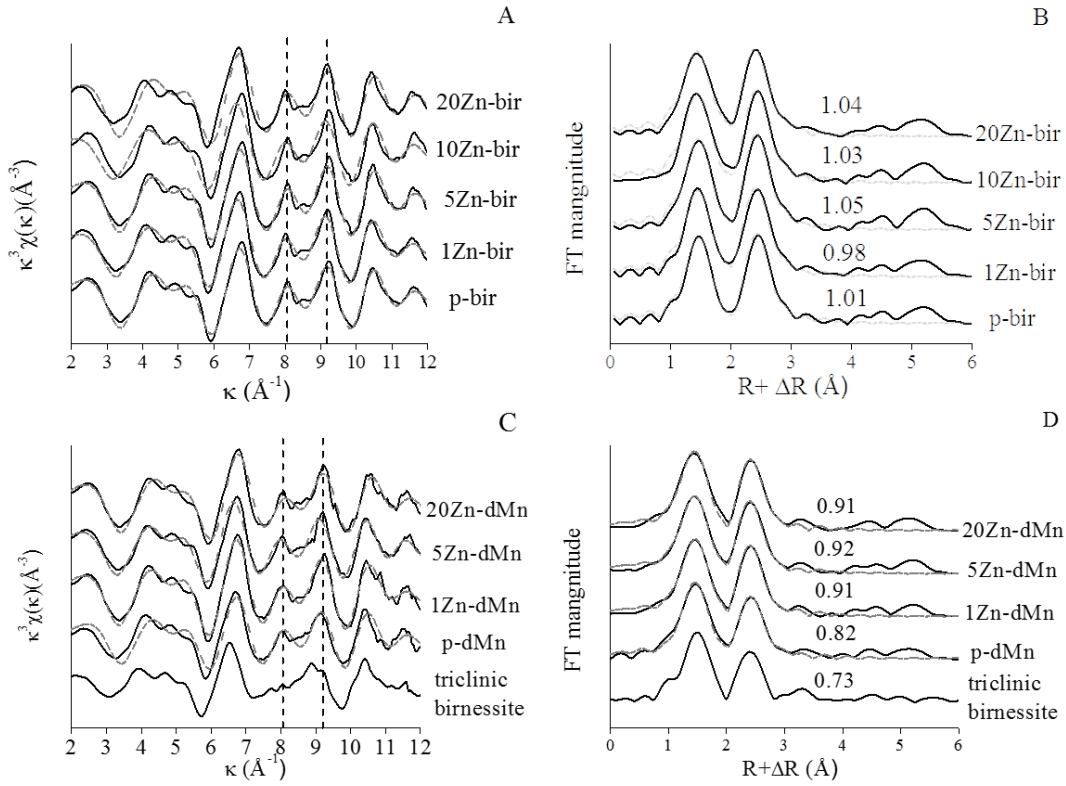

Figure 2.5 k^3-weighted Mn K-edge EXAFS and Fourier transformed (FT) spectra (not corrected for phase shift) of pure and Zn coprecipitated acid birnessite (A, B) and δ-MnO_2 (C, D). Raw and fitted data are in solid and dotted lines, respectively. Triclinic birnessite was also plotted to compare with δ-MnO_2 samples. Vertical dashed lines in (A) and (C) highlight the indicator region. The ratios of second shell (Mn-Mn edge sharing) and first shell (Mn-O) in FT spectra are shown in (B) and (D).

Mn EXAFS fitting of all the oxide samples used a single scattering model considering the Mn-O, Mn-Mn edge sharing (Mn-Mn_{edge}), and Mn-Mn corner sharing (Mn-Mn_{corner}) paths (results in Table 2.2 and Figure 2.5). For pure and Zn-birnessite samples, best fits were obtained with ~6 O atoms at ~1.91–1.92 Å (consistent with Mn in octahedral coordination), ~5–6 Mn atoms at 2.87–2.88 Å, and ~1 Mn atom at 3.47–3.49 Å. The distances for the two Mn-Mn paths were consistent with previously reported values [24, 37, 57]. The Mn-Mn_{edge} path is attributed to layer MnO_6 octahedra, and the coordination number (CN) can be affected by both particle size and layer vacancy site density (i.e. a fully filled

MnO_6 layer has CN of 6; both decreasing particle size and increasing amount of vacancy sites will lead to smaller CN values). When Mn(III) incorporates in vacancy sites, increasing amount of layer Mn(III) would increase CN and result in a slightly longer Mn-Mn_{edge} distance [24, 58]. The Mn-Mn_{corner} path is attributed to adsorbed interlayer Mn(II,III) ions [58]. Increasing amount of interlayer Mn(II) would result in a longer Mn-Mn_{corner} distance, whereas increasing amount of interlayer Mn(III) would result in an increase in the CN [57]. For Zn-birnessite samples, increasing Zn content did not result in significant changes in the CNs and distances of these two Mn-Mn shells (except for the slight decrease of the Mn-Mn_{corner} distance at 10 and 20% Zn contents), suggesting little changes to the vacancy site density and layer/interlayer Mn(III) contents. This is consistent with no changes in the 8–9.2 $Å^{-1}$ indicator region in the EXAFS spectra (Figure 2.5C), as well as the small changes in Mn(III) content and AOS as determined by the Mn XANES spectra. For δ-MnO_2, with increasing Zn content, the Mn-Mn_{edge} path showed a decrease in distance from 2.884 (pure δ-MnO_2) to 2.871–2.872 Å (all the Zn-coprecipitated δ-MnO_2), suggesting less layer Mn(III) content. This was also observed in Ni impacted biogenic Mn oxides [58]. The CN for the Mn-Mn_{edge} path also decreased from 6.2 (pure δ-MnO_2) to 4.6–4.8 (Zn-coprecipitated δ-MnO_2). The decreased CN could result both from decrease in Mn(III) within layers and deduction of particle size. The Mn-Mn_{corner} path showed decreased CN from 1.0 (pure δ-MnO_2) to 0.5 (20Zn-dMn), suggesting decreasing amount of adsorbed Mn(II,III) at interlayer region. A continuous decrease in distance was also observed for the Mn-Mn_{corner} path, from 3.515 (pure δ-MnO_2) to 3.451 Å (20Zn-dMn), suggesting relatively less interlayer Mn(II) in the presence of Zn.

Table 2.2 Shell-by-shell fitting results of Mn EXAFS for pure and Zn coprecipitated acid birnessite and δ-MnO_2 samples.

Sample label	R	Shell	CN	Distance(Å)	σ^2
Acid birnessite					
p-bir	0.0049	Mn-O	6.0 (0.8)	1.919 (0.006)	0.007 (0.001)
		$Mn\text{-}Mn_{edge}$	5.5 (0.8)	2.877 (0.007)	0.007 (0.001)
		$Mn\text{-}Mn_{corner}$	0.9 (0.7)	3.487 (0.047)	0.007 (0.001)
1Zn-bir	0.0094	Mn-O	6.0 (1.1)	1.916 (0.009)	0.006 (0.002)
		$Mn\text{-}Mn_{edge}$	5.8 (1.2)	2.877 (0.009)	0.007 (0.001)
		$Mn\text{-}Mn_{corner}$	1.0 (1.0)	3.491 (0.058)	0.007 (0.001)
5Zn-bir	0.0032	Mn-O	6.3 (0.7)	1.914 (0.005)	0.007 (0.001)
		$Mn\text{-}Mn_{edge}$	5.5 (0.7)	2.871 (0.005)	0.007 (0.001)
		$Mn\text{-}Mn_{corner}$	0.9 (0.6)	3.490 (0.033)	0.007 (0.001)
10Zn-bir	0.0183	Mn-O	7.0 (1.5)	1.913 (0.013)	0.008 (0.002)
		$Mn\text{-}Mn_{edge}$	5.2 (1.3)	2.869 (0.013)	0.006 (0.002)
		$Mn\text{-}Mn_{corner}$	0.9 (1.1)	3.476 (0.083)	0.006 (0.002)
20Zn-bir	0.0081	Mn-O	6.7 (1.1)	1.914 (0.008)	0.007 (0.001)
		$Mn\text{-}Mn_{edge}$	5.2 (1.0)	2.868 (0.009)	0.006 (0.001)
		$Mn\text{-}Mn_{corner}$	1.0 (0.8)	3.469 (0.045)	0.006 (0.001)
δ-MnO_2					
p-dMn	0.0077	Mn-O	5.6 (0.9)	1.921 (0.008)	0.005 (0.001)
		$Mn\text{-}Mn_{edge}$	6.2 (0.9)	2.884 (0.008)	0.008 (0.001)
		$Mn\text{-}Mn_{corner}$	1.0 (0.8)	3.515 (0.061)	0.008 (0.001)
1Zn-dMn	0.0049	Mn-O	6.0 (0.8)	1.914 (0.006)	0.005 (0.001)
		$Mn\text{-}Mn_{edge}$	4.9 (1.0)	2.872 (0.007)	0.008 (0.001)
		$Mn\text{-}Mn_{corner}$	0.8 (0.9)	3.453 (0.054)	0.008 (0.001)
5Zn-dMn	0.0034	Mn-O	6.8 (0.6)	1.913 (0.005)	0.006 (0.001)
		$Mn\text{-}Mn_{edge}$	4.8 (0.6)	2.871 (0.005)	0.006 (0.001)
		$Mn\text{-}Mn_{corner}$	0.6 (0.5)	3.471 (0.040)	0.006 (0.001)
20Zn-dMn	0.0075	Mn-O	6.9 (1.0)	1.910 (0.007)	0.006 (0.001)
		$Mn\text{-}Mn_{edge}$	4.7 (1.1)	2.871 (0.009)	0.007 (0.001)
		$Mn\text{-}Mn_{corner}$	0.5 (0.8)	3.451 (0.049)	0.007 (0.001)

2.5 Discussion

2.5.1 Layer stacking

Based on HRTEM observations, pure δ-MnO_2 had 5±1 layers and pure acid birnessite had 11±1 layers. Both numbers are higher than previously reported values obtained by XRD (3–4 layers for δ-MnO_2 and ~6 layers for acid birnessite) [24, 109]. Other studies have also observed higher layer numbers from TEM than XRD [109], likely because XRD is sensitive to coherent scattering domains (i.e., bending and fault-stacked particles are less accounted for). In this study, all the oxide samples showed significant bending and stacking faults of the MnO_6 layers (and more significant with Zn impact); therefore, we used HRTEM to estimate the numbers of stacked layers.

Both birnessite and δ-MnO_2 showed decreases in layer stacking with increasing Zn content. Disturbed layer stacking has also been previously observed during Ni, Co, Fe, and V coprecipitation with acid birnessite and Zn coprecipitation with biogenic Mn oxides [14, 61, 80, 81, 115, 136], and were attributed to the replacement of interlayer alkaline cations (Na^+, K^+) by foreign metals [84]. In this study, pure acid birnessite had higher alkaline cation contents than δ-MnO_2, likely due to its larger lateral particle size and more layer stacking that allowed more cations at the interlayer region. With increasing Zn content, significant decrease of K^+ content was observed for acid birnessite (Table 2.1), while no obvious changes were observed for the overall alkaline cation content (K^+ and Na^+) for δ-MnO_2. This is consistent with HRTEM and XRD results showing significant disruption of layer stacking for birnessite as compared to the small changes in layer stacking for δ-MnO_2.

2.5.2 Interlayer structure

Zn EXAFS spectra (Figure A.3) and fitting results (Table A.2) revealed that Zn formed inner-sphere complexes (Zn^{IV} or Zn^{VI}) above/below the vacancy sites, consistent with the coordination environments during its adsorption onto biogenic and synthetic birnessite phases as well as coprecipitation with biogenic Mn oxides [84, 139, 142]. No previous studies have observed Zn substitution at vacancy sites, likely due to the large size difference between octahedrally coordinated Zn (0.60 Å) and Mn(III) (more likely to exist as low-spin state [61], 0.58Å) or Mn(IV) (0.53 Å) [155], as well as the large crystal field stabilization energy (CFSE) required for Zn to enter vacancy sites [74]. As discussed above, the interlayer alkali cation content was much higher for acid birnessite (10.5% in pure birnessite) than δ-MnO_2 (3% in pure δ-MnO_2), and showed more obvious decrease with increasing Zn contents (Table 2.1), suggesting more Zn replacement. Compared to alkali cations, the release of Mn(II)/Mn(III) by surface adsorbed Zn was more significant in the δ-MnO_2 system. This was confirmed by the consistent decrease in Mn(II)/Mn(III) contents and increase in AOS from XANES fitting (Figure 2.4), as well as the decrease of Mn-Mn_{corner} CN in Mn EXAFS fitting (Table 2.2). The slight decrease in the Mn-Mn_{corner} path distance suggests that the ratio of Mn(II)/Mn(III) is lower in Zn-coprecipitated δ-MnO_2 samples. This indicates that Mn(II) is less strongly bound to layers and the expelling effects of Mn(II) is more significant compared to Mn(III).

The interlayer distance of Mn oxides can be affected by many factors. Interlayer hydrated K^+ can stabilize adjacent layers through H-bonding [65, 156], and the introduction of foreign cations can expel water molecules and K^+ and cause layer collapse [61, 80, 84, 109]. These factors can potentially account for the decrease in interlayer spacing in our Zn-birnessite system as observed by HRTEM (Figure 2.1). Removal of water by freeze drying

and the high vacuum environment used for HRTEM experiments can also cause dehydration and layer collapse [18, 65], which can be the main reasons for the generally smaller interlayer distances (5–7 Å) observed by HTREM in our system than previously reported ~7 Å for both acid birnessite and δ-MnO_2 [18].

2.5.3 Layer structure

Based on previous studies and the results above, Zn repelling of layer Mn(III) is more likely to happen in phyllomanganate phases with low AOS and high Mn(III). Grangeon et al found that Zn expelled Mn(III) during its adsorption on δ-MnO_2 with an AOS of 3.76 with ~13% layer Mn(III) [109]. Similar effects were also observed in our Zn-coprecipitated δ-MnO_2 systems with an AOS of 3.77 and ~15% Mn(III) contents. However, our EXAFS fitting results showed no change of the Mn-Mn_{edge} CN and distance for the acid birnessite system, suggesting that Zn addition did not significantly affect layer Mn(III) contents in acid birnessite phases. This is possibly due to the already low content of layer Mn(III) in acid birnessite (AOS 3.92, ~6% Mn(III)), causing the Mn(III) expelling effect by Zn to be not as obvious as the δ-MnO_2 system. XRD also showed less layer structure modification in acid birnessite samples than δ-MnO_2 samples (Figure 2.2), also likely attributed to the higher structure order in the acid birnessite phases. Natural biogenic Mn oxides are typically amorphous phases with lower AOS and more Mn(III) contents than synthetic phyllomanganate analogs (i.e., acid birnessite and δ-MnO_2) [24, 34, 57, 58], therefore, one might expect that Zn can cause significant modifications of biogenic Mn oxide layer structure. Boonfueng et al on Zn presence during biogenic Mn oxide formation showed modifications to the 8–9.2 $Å^{-1}$ EXAFS indicator region, although the authors concluded no structural changes [73]. The reduction of layer Mn(III) was observed in δ-MnO_2 and

biogenic Mn oxides (discussed in CHAPTER 5) instead of acid birnessite. The synthesis of δ-MnO_2 and biogenic Mn oxides are through oxidation of Mn^{2+} while acid birnessite was synthesized through reduction of potassium permanganate by HCl, details in methods. Unreacted Mn^{2+} could react with structural Mn(IV) producing Mn(III) in δ-MnO_2 and biogenic Mn oxide layers [26]. All pure and Zn coprecipitated acid birnessite have no layer Mn(III) without the presence of Mn^{2+} in the solutions.

The reduction of layer size can be attributed to pH change and/or crystal growth inhibition caused by Zn addition. First, metal doping during phyllomanganate synthesis is a common method for producing Mn oxide materials with desired properties, though the pH change caused by metal hydrolysis were rarely measured or discussed in previous studies [61, 79, 81, 106, 137]. In this study, the addition of Zn slightly decreased the pH in the synthesis solutions. Yu et al also found that Zn addition decreased the pH of fungi growing media during the formation of biogenic Mn oxides [84]. Grangeon et al found that acidic condition caused the dissolution and smaller layer size when pre-formed δ-MnO_2 was equilibrated at low pH [157]. Secondly, previous studies have indicated that addition of foreign oxyanions (phosphate, silicate and sulfate) can inhibit the layer growth of acid birnessite. These oxyanions should not significantly change the pH of the synthesis environment but still reduced the layer size by inhibiting crystal growth [81, 138]. The effects of Zn co-precipitation with biogenic Mn oxides in a well-buffered media is ongoing to investigate the significance of these two factors.

2.5.4 Particle size

Particle size can significantly change the electrochemical [138, 158, 159], catalytic [138], adsorptive, and redox properties of phyllomanganates [63, 160]. BET Surface area [24, 57, 63],

TEM [34, 109], XRD [109, 161] and PDF [81, 141, 162] have been used to estimate the size dimensions of Mn oxides. Size estimation of phyllomanganates using BET surface area is difficult due to the complex morphology, and can be simplified using a spherical model [63]. Smaller particle size in Zn-coprecipitated samples, as revealed by other techniques, was supposed to expose more external surfaces, yet less surface area was observed by BET due to aggregation [14]. Therefore, much caution should be taken when BET specific surface area is utilized to estimate the size of heavily aggregated particles.

Estimation of acid birnessite and δ-MnO_2 particle size by TEM images is difficult due to strong aggregation. Lateral particle sizes (along the *a*-*b* plane) of ~50–200 nm for acid birnessite and ~20–100 nm for δ-MnO_2, can be concluded based on a previous study [34] and our HRTEM observation. With increasing Zn content, our HRTEM analysis observed a general decrease of layer stacking and lateral particle size. Curling and faults of the MnO_6 nanosheets can lead to less periodicity in the *a*-*b* plane and less layer stacking consistency along *c* axis [65, 109, 141]. This is likely the reason why the CSD size calculated by XRD and PDF are much smaller than the particle size observed by HRTEM. Indeed, the CSD size revealed by PDF is around 5 nm for acid birnessite and 2–3 nm for δ-MnO_2 (Figure 2.6). The XRD calculated birnessite CSD size along *c* axis is 4–7 nm, agreed quite well with the PDF results, but both smaller than HRTEM measured size.

Interestingly, with increasing Zn content, the PDF CSD size barely changed for both acid birnessite and δ-MnO_2 (Figure 2.6), while broaden peaks in XRD (Figure 2.2) indicated decreasing CSD size along *c* axis (especially acid birnessite) and in *a*-*b* plane (especially δ-MnO_2) [138]. Foreign Zn caused more incoherence in both phyllomanganates, e.g. layer collapse, curling, stacking faults and large amorphous aggregated area, which

significantly broadened XRD Bragg peaks and decreased crystallite sizes. However, for PDF which detects both Bragg and diffuse scatterings, decreased crystallinity and formation of sub-domains, although decreasing the peak sharpness, would not affect the longest atomic pair distances which determined the signal fall-offs and CSD size.

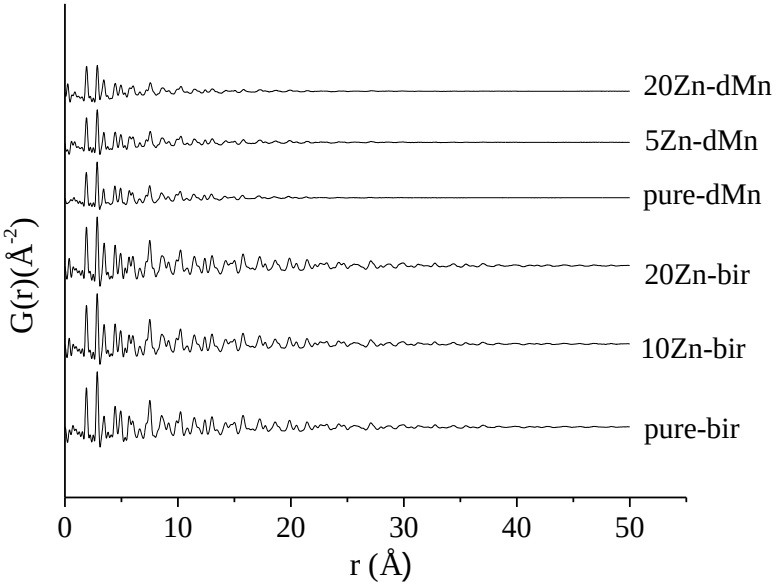

Figure 2.6 PDFs of pure and Zn coprecipitated birnessite and δ-MnO_2.

2.6 Conclusions

This systematic study demonstrated that the impact of Zn during phyllomanganate (acid birnessite and δ-MnO_2) formation are much more significant than by Zn adsorption alone [109]. Zn neutralized the negative surface charge of phyllomanganates and caused great particle aggregation. The introduced Zn during acid birnessite formation expelled interlayer alkaline cations and water molecules and interrupted the layer stacking along *c* axis. The AOS of δ-MnO_2 increased due to Mn(II)/Mn(III) expelling by Zn, while such

effect was not obvious in the acid birnessite system due to the already high AOS and little Mn(II, III) in acid birnessite. Zn existed as inner-sphere surface complexes (Zn^{IV} or Zn^{VI}) above/below vacancy sites as adsorbed species instead of substitution at vacancy sites. Zn decreased Mn(III) contents within Mn oxide layers, leaving more vacancy sites available for future reactions (e.g. sorption of other cations). For acid birnessite, layer stacking and interlayer cations/water molecules are significantly affected with minimal modulation of the layer structure. The modification of layer structure (e.g. crystallinity and layer Mn(III) contents) is much more significant in the δ-MnO_2 system.

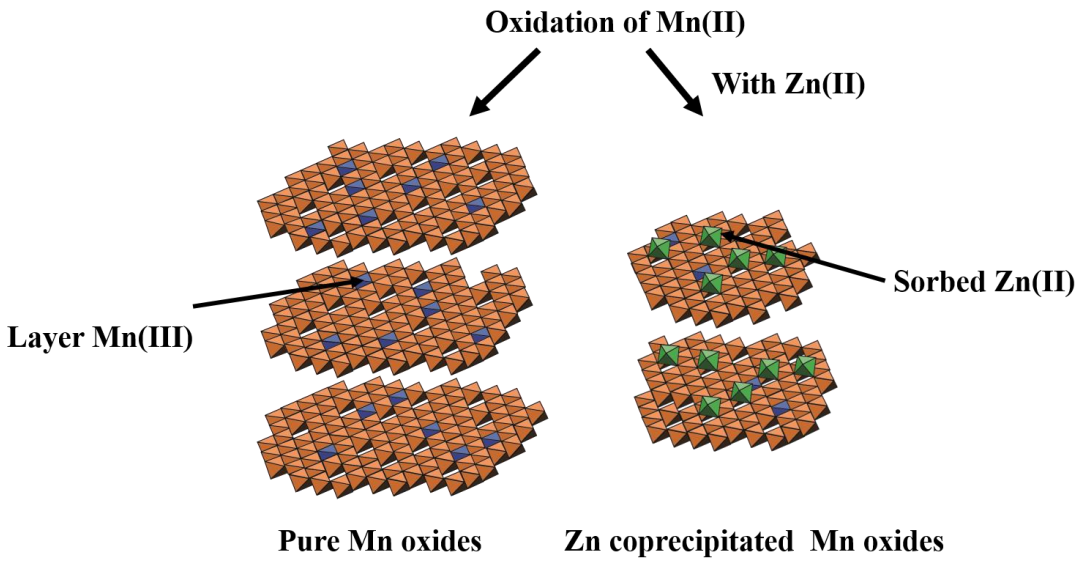

Figure 2.7 Schematic summary of coprecipitated Zn effects on the structure of Mn oxides.

Previous studies have shown that birnessite structure interruption caused by foreign metals is in the reverse relationship with the compatibility (Co > Ni >Fe) of metals in birnessite layers [80]. This study provides insights on the possible prediction of structural changes caused by Zn and other similar incompatible cations on natural and synthetic

phyllomanganates with different crystallinity. The sorptive ability of these metals impacted oxides are expected to change significantly due to the less negative surface charge, decreased particle size, and increased vacancy site density [14, 61, 63, 160, 163, 164]. Zn also decreased Mn(II, III) contents and increased AOS in the oxides with high Mn(II, III) contents, which, together with the modified sorptive reactivity, can potentially have great influences on the oxidative reactivity, transformation, and microbial anaerobic respiration of Mn oxides [6, 18, 63, 160]. These factors can also potentially change the band gap and other catalytic properties of Mn oxides [12, 165, 166].

2.7 Acknowledgements

S. Zhao and Y. Tang acknowledge funding support from U.S. National Science Foundation (NSF) under grant No. 1710285 and the National Aeronautics and Space Administration (NASA) under grant No. NNA15BB03A. We thank Dr. Hailong Chen (Georgia Tech) for help with XRD analysis. We also appreciate the support from beamline scientists Drs. Benjamin Reinhart and Sungsik Lee (APS Beamline 12BM), Qing Ma (APS Beamline 5-BM-D), and Ryan Davis (SSRL Beamline 4-1) on experiment setup. Portions of this research were conducted at the Advanced Photon Source (APS) and Stanford Synchrotron Radiation Lightsource (SSRL). APS is a U.S. Department of Energy (DOE) Office of Science User Facility operated for the DOE Office of Science by Argonne National Laboratory under Contract No. DE-AC02-06CH11357. Use of SSRL, SLAC National Accelerator Laboratory, is supported by DOE Office of Science, Office of Basic Energy Sciences under Contract No. DE-AC02-76SF00515.

CHAPTER 3. ZN PRESENCE DURING MINERAL FORMATION AFFECTS THE SORPTIVE REACTIVITY OF MANGANESE OXIDES [2]

3.1 Abstract

The sorptive reactivity of layered Mn oxides is controlled by their layer and interlayer structure, which can be affected by processes such as metal coprecipitation. This study investigated the effect of Zn coprecipitation on the sorptive reactivity of δ-MnO_2, a common layered Mn oxide mineral. Selected cation (Cd^{2+}) and anion (phosphate and arsenate) species were used to probe the changes in δ-MnO_2 sorptive reactivity. Cd uptake by δ-MnO_2 was suppressed by Zn coprecipitation but total metal uptake (Cd and Zn) was enhanced, indicating more available vacancy sites (e.g. smaller particle and higher vacancy site density) in Zn coprecipitated δ-MnO_2. Phosphate and arsenate sorption onto δ-MnO_2 were significantly enhanced by Zn coprecipitation, and the enhancement was more effective compared to Zn sorption on pure δ-MnO_2. X-ray diffraction and X-ray adsorption spectroscopy analysis was not able to detect the formation of bulk and/or surface precipitations or ternary complexes. The enhanced anion adsorption on Zn coprecipitated δ-MnO_2 was likely due to compensation of negative surface charge by adsorbed Zn, as well as the structural modifications introduced by Zn coprecipitation. Results from this study can help better understand the interactions between metal-coprecipitated Mn oxides and other species in natural environments.

3.2 Introduction

[2] Shiliang Zhao, Chenning Li, Pan Liu, Rixiang Huang, Emily M. Saad, Yuanzhi Tang. Zn(II) presence during mineral formation affects the sorptive reactivity of manganese oxide δ-MnO_2. *Soil Systems* (invited article for Special Issue *Soil Processes Controlling Contaminant Dynamics*), 2018. 2(2): p. 19..

Mn oxides, especially layered phyllomanganates, are important metal oxides in terrestrial and marine environments [1-3]. Because of the high surface area, negative surface charge, vacancy sites, and high oxidative potential, phyllomanganates have strong tendency to interact with and strongly influence the fate and transport of heavy metals, such as Ni [61, 75, 140, 167], Co [14, 79, 80, 167-169], Pb [49, 61, 77, 81, 164, 170], Cu [76, 154, 167], Zn [61, 73, 85, 109, 140, 164], and Cd [68, 171]. Phyllomanganates can interact with metals in different ways (e.g. sorption, coprecipitation, incorporation), which in turn can affect the property and reactivity of the host mineral phases. During adsorption to δ-MnO_2, metal cations can either directly incorporate into vacancy sites, or form surface adsorption complexes above or below vacancies sites and/or edge sites [2, 151]. The ratio between incorporation and surface complexation (referred to as compatibility) is metal specific, and was suggested to be dependent on the differences in atomic size and charge between foreign metal cations and Mn(III, IV) [2, 80], as well as the metal cation crystal field stability energy (CFSE) [74]. Adsorption of metal cations on pre-formed Mn oxides (i.e. sorption) can replace interlayer Mn(II) and alkaline cations [108, 172], compensate for the negative surface charge, thus affecting the reactivity of Mn oxides towards other species [62, 63, 108]. In comparison, the presence of metal cations during Mn oxide mineral formation (i.e. coprecipitation) can cause more significant changes in Mn oxide structure, such as layer stacking, average oxidation state [14, 61, 80, 173], vacancy site density, and layer symmetry [79], which also leads to modified mineral reactivity. For example, the presence of Ni, Co, Fe, and Cu during birnessite formation was found to significantly modify birnessite thermal stability, adsorptive reactivity towards Pb, and oxidative reactivity towards arsenite [14, 61, 80, 173].

The effects of metal coprecipitation on layered Mn oxides are also metal-specific.

The compatibility of foreign metal ions in birnessite layers is Fe(III) < Ni(II) < Co(III), due to the atomic radii, charges and crystal field stylization energy, and the interruption on birnessite structure is in the reverse order Fe(III) > Ni(II) > Co(III) [14, 61, 80]. Zn shows the least compatibility compared to other transition metals such as Ni or Co. As a result, upon adsorption onto Mn oxides, Zn never incorporates into vacancy sites, but always exists as adsorbed species above/below vacancy sites [74] and sometimes edge sites [135]. The local coordination environment of surface adsorbed Zn is preferably tetrahedral (^{IV}Zn) at low Zn loadings and octahedral (^{VI}Zn) at high Zn loadings [2, 84, 117], though it is also dependent on the crystallinity of the host Mn oxide phase [109]. A recent study by Grangeon et al [109] found that Zn adsorption on δ-MnO_2 caused crystal dissolution, decrease of coherent scattering domain size, decrease of layer Mn(III) content, and increase of vacancy site density. Similar effects have not been observed for the adsorption of other metal cations on Mn oxides. When Zn was added during the formation of biogenic Mn oxides, it was found to interrupt the mineral layer stacking [84]. Our recent study showed that the presence of Zn during abiotic δ-MnO_2 formation has more significant impacts on δ-MnO_2 structure as compared to Zn adsorption on pure δ-MnO_2[174]. These studies demonstrate the significant effects of Zn treatment, (either sorption or coprecipitation) on δ-MnO_2 structure, which can potentially affect the sorptive reactivity of δ-MnO_2. However, systematic investigations are still missing on the effects of Zn-coprecipitation on Mn oxide reactivity, such as sorption or redox reactivity.

This study systematically investigated the impact of Zn coprecipitation on the sorptive reactivity of δ-MnO_2 toward both cations and anions. Zn/Mn molar ratio used in this study is 0-0.2, which is with the range observed in natural environment (0~0.005 in

marine nodules and basin soils [118-120], as high as 0.03 in coal mine drainage treatment system [121] and 0.46 in contaminated sediments [122]). We used Cd^{2+} as a representative cation and phosphate and arsenate as representative anions to probe the change in sorptive reactivity. Cd is a toxic heavy metal and its fate in the environment is strongly influenced by sorption onto metal oxyhydroxides, especially Mn oxides [68, 123, 124]. Both phosphate and arsenate are important environmental anions, and their fate and transport are strongly influenced by interactions with geomedia [61, 99, 125-130]. Cd, phosphate, and arsenate sorption kinetics, isotherms, and pH edges on Zn-coprecipitated δ-MnO_2 was compared with the sorption on Zn sorption on pre-formed pure δ-MnO_2 (hereafter referred to as Zn-sorbed δ-MnO_2).

3.3 Methods

3.3.1 Synthesis of pure and Zn-coprecipitated δ-MnO_2

All reagents used in this study are ACS grade or higher. δ-MnO_2 was synthesized [28] in the presence of varied concentrations of Zn. Calculated amount of $ZnSO_4$ was dissolved in 160 mL of 0.2964 mol L^{-1} $MnSO_4$ solution to achieve desired Zn/Mn_{total} ratio. This solution was pumped at a rate of 25 mL min^{-1} with a syringe pump into a beaker containing 160 mL of $KMnO_4$ (5.0 g) and 180 mL of NaOH (3.5 g) under vigorous stirring. The molar ratio of Zn/Mn_{total} was 0, 0.01, 0.05, and 0.20. After overnight settlement, the solids were separated by vacuum filtration (0.22 μm), rinsed and dialyzed in deionized (DI) water, and freeze dried. Samples were labeled as pure, coppt0.01, coppt0.05, and coppt0.20 δ-MnO_2 for the samples synthesized with initial Zn/Mn molar ratios of 0, 0.01, 0.05, and 0.20, respectively. A portion of the freezer-dried powders were digested using hydroxylamine hydrochloride and measured for elemental compositions (Zn, Mn) using

inductively coupled plasma – mass spectrometry (ICP-MS) (Table 3.1).

3.3.2 Cation and anion adsorption on pure and Zn-coprecipitated δ-MnO_2

$CdCl_2$, $ZnSO_4$, Na_2HPO_4 and Na_2HAsO_4 were used to make 1 M Cd, 1 M Zn, 2.5 mM phosphate, and 2.5 mM arsenate stock solutions, respectively. 10 mg pure or Zn-coprecipitated δ-MnO_2 was suspended in 20 mL DI water and sonicated for 1 min to disperse the particles. For each sorption experiment, calculated amount of stock solutions were added to achieve desired sorbate concentration. Sorption isotherm and kinetic experiments were conducted at pH 6. pH edge experiments were conducted at pH 4–8. The reaction vials were agitated end-to-end on an orbital shaker at 150 rpm. At certain time points, aliquots of the reaction suspension were taken and syringe filtered (0.22 μm). Phosphate [175] and arsenate [176] concentrations in the filtrates were measured using colorimetric methods on a UV-vis spectrometer (Cary 60, Agilent). Dissolved Zn and Cd concentrations were determined using ICP-MS.

For Cd sorption, ionic strength was at 0.1 M NaCl. Due to the relatively large pH fluctuation during sorption, 20 mM MES buffer was used to maintain the pH at 6. For phosphate and arsenate sorption, ionic strength was at 10 mM NaCl. No buffers were used as the pH fluctuation throughout experiments was relatively small. At 0, 3, 12, and 22 h, HCl and NaOH solutions were used to adjust the small pH changes.

To examine the possible surface precipitation or ternary complexation between anions and pre-loaded Zn, X-ray diffraction (XRD) and X-ray adsorption spectroscopy (XAS) analysis were conducted on the reaction products (details in Supporting Information, SI, **Text S1**). Both Langmuir and Freundlich models was used to fit the isotherm data. For

kinetic data, pseudo first order, pseudo second order, and particle diffusion models were used to fit the data.

For Cd adsorption on Zn-coprecipitated δ-MnO_2, total metal uptake (both Cd and Zn) was calculated using the following equation in order to investigate the overall metal cation uptake ability:

Total metal uptake = initially loaded Zn + adsorbed Cd – desorbed Zn (Eq.1)

3.3.3 Cation and anion sorption on Zn-sorbed δ-MnO_2

Based on previous studies [84] and our recent study [174], when Zn is added during δ-MnO_2 formation, it exists as surface adsorbed species, but can introduce significant structural modification. In order to compare the effects of Zn-coprecipitation induced structural modification on δ-MnO_2 sorptive reactivity, we also conducted parallel experiments where pure δ-MnO_2 with Zn sorption (i.e. Zn-sorbed δ-MnO_2, with Zn concentrations comparable to the coprecipitation system) was used as the sorbent, with subsequent addition of Cd, phosphate, and arsenate as sorbate.

Zn-sorbed δ-MnO_2 samples were produced by reacting 0.5 g L^{-1} pure δ-MnO_2 with varied concentrations of $ZnSO_4$ (0.25–2 mM) at pH 6 and 0.1 M NaCl background electrolyte. After shaken at 150 rpm for 24 h, reaction reached steady state and the suspension was centrifuged at 13000 rpm. Zn concentration in the supernatant was measured by ICP-MS. Zn uptake was calculated by the difference of Zn concentration in the initial suspension and supernatant. After centrifugation, the remaining wet paste (Zn-sorbed δ-MnO_2) was briefly rinsed by DI water, and resuspended in DI water to achieve a solid/liquid ratio of 0.5 g/L. Cd, phosphate, and arsenate was added to the suspension

following the procedures in section 3.3.2 for sorption experiments. Sample labels are shown in Table 3.1.

Table 3.1 Initial Zn/Mn_{total} molar ratio in the synthesis suspension and final Zn/Mn molar ratio in the solid products.

Sample category	Sample label	Initial Zn/Mn molar ratio	Zn/Mn molar ratio in final solids	Zn uptake (mmol/g)
pure δ-MnO_2	pure	0	0	0
Zn-coprecipitated δ-MnO_2	coppt0.05	0.05	0.04	0.36
	coppt0.20	0.20	0.21	1.50
Zn-sorbed δ-MnO_2	sorb0.07	0.07	0.06	0.42
	sorb0.20	0.20	0.15	0.99
	sorb0.30	0.30	0.19	1.30
	sorb0.60	0.60	0.31	1.69

3.4 Results and Discussion

3.4.1 Cation adsorption on pure and Zn coprecipitated δ-MnO_2

Cd adsorption isotherms on Zn coprecipitated δ-MnO_2 are shown in Figure 3.1. Increasing initial Cd concentration resulted in gradual increase in Cd uptake. The Langmuir model was used to fit the data (Figure 3.1A, Table 3.3). Maximum Cd uptake (C_{max}, mmol g^{-1}) decreased slightly from 1.49 (pure δ-MnO_2) to 1.38 (coppt0.05) and 1.20 (coppt0.20), indicating the competitive adsorption between Cd and pre-loaded Zn. This decrease is not significant considering that the fitting errors of C_{max} is in the range of 0.03–0.07. In order to compare Zn-coprecipitated and Zn-sorbed δ-MnO_2, sample sorb0.20 was also prepared by mixing 0.5 g L^{-1} pure δ-MnO_2 and calculated amount of $ZnSO_4$ (Zn/Mn= 0.2). The Zn loading on sample sorb0.20 (Q = 0.99 mmol g^{-1}) was much lower than the Zn coverage in coppt0.20 sample (Q = 1.5 mmol g^{-1}), regardless of the same initial Zn/Mn concentration. Similar phenomenon was also observed for biogenic Mn oxides, i.e. Zn uptake by fungal

Mn oxides was higher when Zn was present during Mn oxide formation compared to Zn uptake by pre-formed Mn oxides [84]. With less surface-loaded Zn, Cd adsorption on sample sorb0.20 was, however, more suppressed (1.1 mmol g^{-1}) compared to sample coppt0.20 (1.2 mmol g^{-1}). This is likely caused by the structural modifications δ-MnO_2 by Zn coprecipitation.

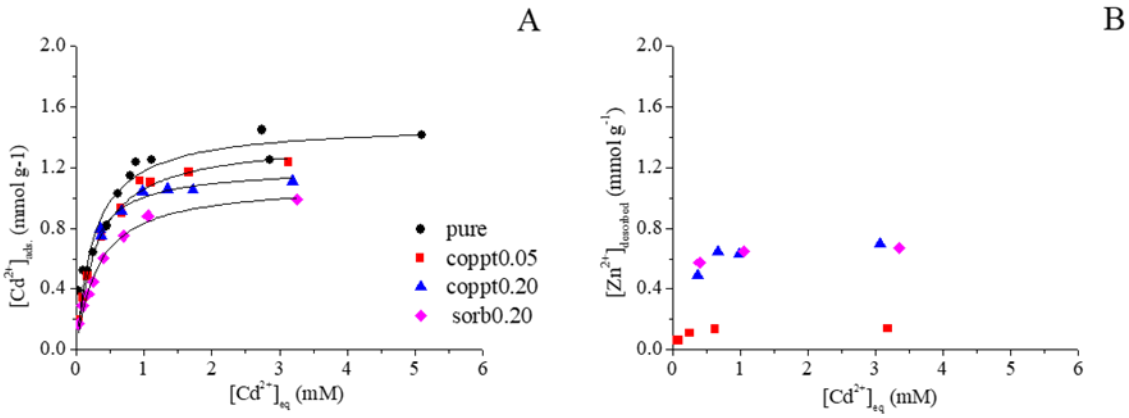

Figure 3.1 (A) Cd adsorption isotherms on pure, Zn-coprecipitated (coppt0.05, coppt0.20) and Zn-sorbed (sorb0.20) δ-MnO_2 samples. (B) Amount of Zn release (desorption) during Cd adsorption. Solid lines are Langmuir model fitting results.

Figure 3.1(B) shows the concentration of solution Zn during Cd adsorption on samples coppt0.05, coppt0.20, and sorb0.20 δ-MnO_2. With increasing initial Cd concentration, more Zn was released to the solutions. However, the concentration of adsorbed Cd was always higher than released Zn. This suggests that a fraction of Cd was adsorbed via exchange with Zn, and the rest of Cd was adsorbed on unoccupied surface sites. Because the surface sites of both coppt0.20 and sorb0.20 samples were pre-occupied with a large amount of Zn, they showed a similar amount of desorbed Zn, both higher than that of coppt0.05. Total metal uptake (Eq. 1) was also calculated to compare the adsorption

capacity of different minerals (Figure 3.2). At low Cd concentrations, total metal uptake increased with increasing Cd concentration. Total metal uptake reached a plateau after ~1 mM $[Cd]_{eq}$ (i.e. steady state Cd concentration in the reaction suspension), suggesting the saturation of available surface sites for cation adsorption. Although Zn coprecipitation with δ-MnO_2 decreased Cd adsorption (due to the pre-occupation of surface sites by Zn), the overall metal uptake by coppt0.20 was much higher than pure δ-MnO_2, suggesting significant structural modifications by Zn coprecipitation, e.g. increased availability of surface sites for cation sorption.

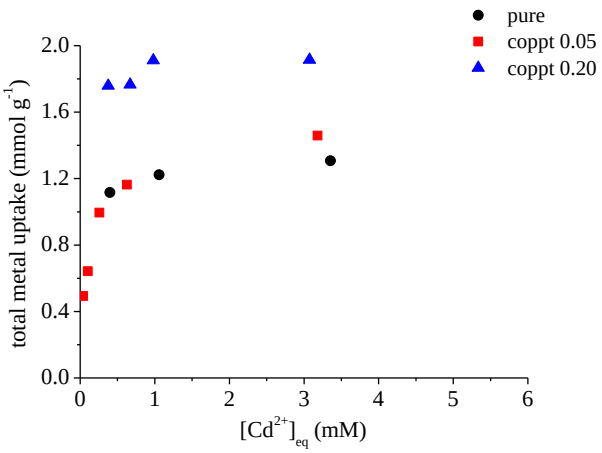

Figure 3.2 Total metal uptake (calculated by Eq. 1) on pure and Zn-coprecipitated δ-MnO_2 samples.

3.4.2 Anion adsorption on pure and Zn coprecipitated δ-MnO_2

3.4.2.1 Phosphate and arsenate adsorption on pure δ-MnO_2

Phosphate and arsenate sorption kinetics (both with 100 μM initial concentration) are shown in Figure 3.3A and B. Both pseudo first and second order kinetic models were used to fit the kinetics data (Figure B.4), and the first order model yielded a better fit (Table

3.2). Arsenate adsorption had a faster adsorption rate constant (k) and reached a higher uptake capacity at steady state. Phosphate pH edge experiments (Figure 3.4) showed a gradual increase in phosphate uptake by pure δ-MnO_2 with decreasing pH, reaching a maximum at pH < 5, consistent with previous studies [125, 177, 178].

Both phosphate and arsenate sorption reactions were fast and completed within a few hours (Figure 3.3). Therefore, a 24-h reaction time was chosen for phosphate and arsenate isotherm experiments, and the results are shown in Figure 3.3C and D. Both Langmuir and Freundlich models were used to fit the data (Figure B.3) and Langmuir model showed a better fit (Table 3.3). The maximum adsorption capacity for phosphate and arsenate are 81.33 and 109.45 μmol g^{-1}, respectively. Both are a magnitude lower than those of cations, consistent with previous studies [63, 172, 178-180]. The zero point charge (ZPC) of δ-MnO_2 is around 2.8 [181], resulting in a negatively charged surface under a wide range of pH. At the studied pH range, phosphate exists mainly as $H_2PO_4^-$ and HPO_4^{2-} (pKa = 7.21), while arsenate as $H_2AsO_4^-$ and $HAsO_4^{2-}$ (pKa = 6.97) [63, 125]. The electrostatic repulsion between oxyanions and δ-MnO_2 surface is the main cause for limited anion adsorption. Manning et al found that arsenate adsorbed both on edges and at interlayer region of birnessite by forming a bidentate binuclear corner sharing complex [182]. Several other studies proposed that arsenate only adsorbs on edge sites, and attributed the relatively low arsenate adsorption to the limited amount of reactive edge sites for arsenate bonding [63, 183]. Triple layer modeling results showed that the sorption of phosphate is unlikely to be inner-sphere but rather through the formation of out-sphere complexes with Mn oxide surface sites [125]. Wang et al proposed that phosphate, silicate, and sulfate sorb on the edge sites of acid birnessite [138], but direct experimental confirmations (e.g. spectroscopic

analysis) are still needed to confirm the actual binding mechanism(s) of phosphate on Mn oxides [125].

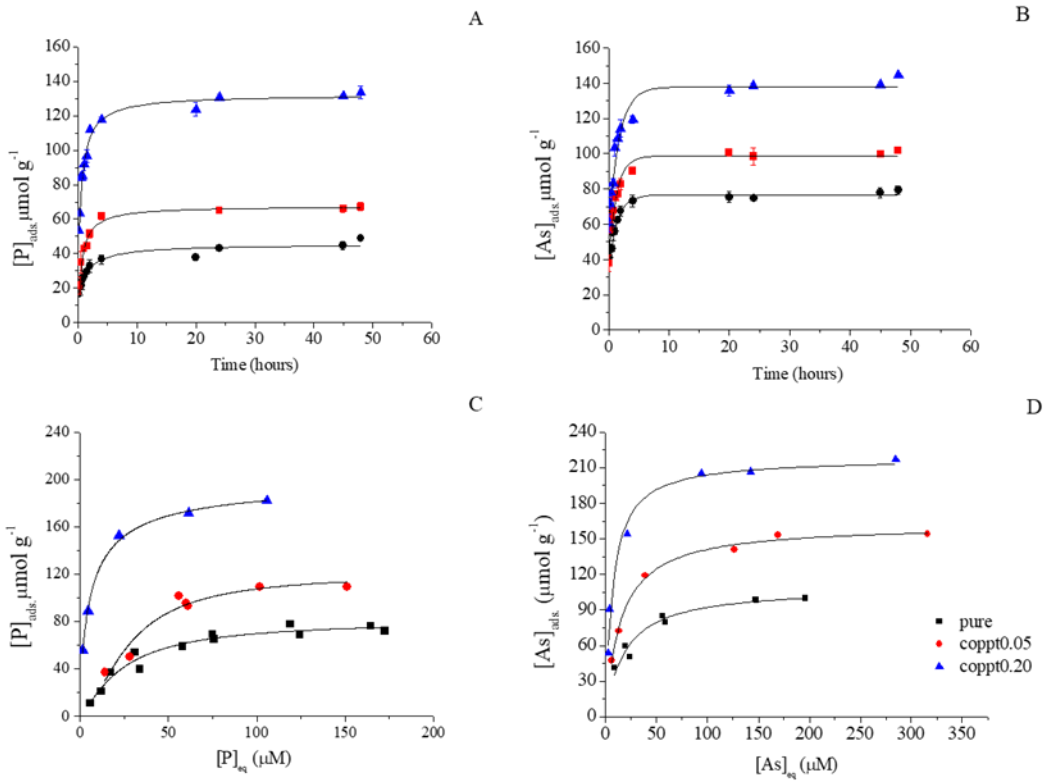

Figure 3.3 (A) Phosphate and (B) arsenate sorption kinetics on pure, coppt0.05, and coppt0.20 δ-MnO_2 samples. Solid lines are pseudo first order model fitting results. (C) Phosphate and (D) arsenate sorption isotherms on pure, coppt0.05, and coppt0.20 δ-MnO_2 samples. Initial phosphate and arsenate concentrations are 100 µM. Solid lines show the Langmuir fitting results. Error bars represent results from duplicates.

3.4.2.2 Phosphate and arsenate sorption on Zn coprecipitated δ-MnO_2

With increasing Zn concentration in Zn-coprecipitated δ-MnO_2, both phosphate and arsenate sorption were greatly enhanced (Figure 3.3 and Figure 3.4**)**. Based on the Langmuir model fitting results of sorption isotherms, phosphate sorption capacity increased from 81.3 (pure δ-MnO_2) to 120.4 (coppt0.05) and 186.2 µmol g^{-1} (coppt0.20). Arsenate

sorption capacity increased from 109.4 (pure δ-MnO_2) to 162.2 (coppt0.05) and 218.0 μmol g^{-1} (coppt0.20). Slopes of the sorption isotherms also became steeper with higher Zn treatment, suggesting that Zn-coprecipitation enhanced the affinity of anion sorbates. Such increased affinity was also manifested in the larger K values from Langmuir model fitting (Table 3.3). Enhanced phosphate and arsenate uptake by Zn-coprecipitated δ-MnO_2 was also observed for the kinetics and pH edge experiments. Adsorption rate constants (k, Table 3.2) are higher for the coppt0.05 and coppt0.20 δ-MnO_2 samples, compared to that of pure δ-MnO_2. In Figure 3.4, the sorption edges of phosphate and arsenate shifted to higher pH values with increasing Zn content for Zn-coprecipitated δ-MnO_2. Previous studies showed that phosphate sorption edges on hydrous Mn oxides shifted to higher pH in Na^+ and Ca^{2+} solutions or seawater, compared to that in water [125]. Co-existing metal cations [172] can also exert similar effects on phosphate adsorption. Therefore, metal cations on Mn oxides generally shift anion sorption edges to higher pH, regardless of cation species or whether the cation was added before or during anion adsorption. This is possibly because cation sorption compensated the negative surface charge of Mn oxides thus increasing anion affinity for the surface, or the potential formation of ternary complex (es) and/or precipitate(s).

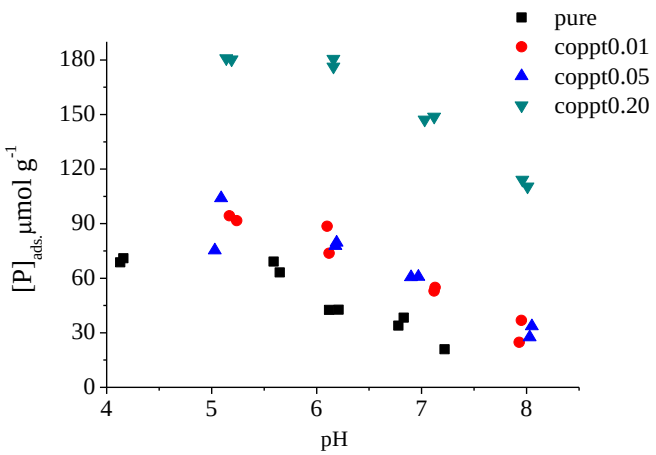

Figure 3.4 Phosphate adsorption on pure, coppt0.05, and coppt0.20 δ-MnO_2 samples as a function of pH. Initial phosphate concentration is 100 µM.

Table 3.2 Pseudo first order model fitting results for phosphate and arsenate sorption kinetics on pure and Zn co-precipitated δ-MnO_2.

Mn oxide type	P kinetics			As kinetics		
	k	Q_e	R^2	k	Q_e	R^2
pure	0.4217	43.4857	0.9176	0.6534	76.7312	0.9824
coppt0.05	0.6221	65.9621	0.9697	0.7433	98.7929	0.9495
coppt0.20	0.6936	128.688	0.9643	0.6985	137.8668	0.9615

Table 3.3 Langmuir model fitting results of Cd, phosphate, and arsenate sorption isotherms on pure, Zn-coprecipitated, and Zn-sorbed δ-MnO_2.

Mn oxide type	Cd isotherm			P isotherm			As isotherm		
	C_{max}	K	R^2	C_{max}	K	R^2	C_{max}	K	R^2
pure	1.49	3.77	0.91	81.3	0.02	0.95	109.4	0.05	0.94
coppt0.05	1.38	3.19	0.99	120.4	0.04	0.96	162.2	0.07	0.99
coppt0.20	1.20	4.11	0.93	186.2	0.25	0.98	218.0	0.14	0.98
sorb0.20	1.10	3.08	0.99	-	-	-	-	-	-

In order to compare the influences of Zn-coprecipitation with Zn-sorption, Zn-sorbed δ-MnO_2 was prepared by mixing pure δ-MnO_2 with 0.25, 0.75, 1, and 2 mM Zn before anion adsorption experiments. ICP-MS analysis of the supernatant suggested that 0.42, 0.99, 1.30, and 1.69 mmol g^{-1} Zn was adsorbed on δ-MnO_2, respectively (Table 3.1). δ-MnO_2 with increasing Zn loading showed enhanced phosphate and arsenate sorption capacities (Figure 3.5). Comparatively, the sorption capacity of Zn-coprecipitated coppt0.20 sample (with 1.5 mmol g^{-1} Zn loading) for phosphate and arsenate is higher than that of all Zn-sorbed δ-MnO_2 samples, even though the Zn loading on sorb0.60 sample is higher than that of the coppt0.20 sample (Figure 3.5). This confirms the significant influences of structural modifications by Zn-coprecipitation with δ-MnO_2.

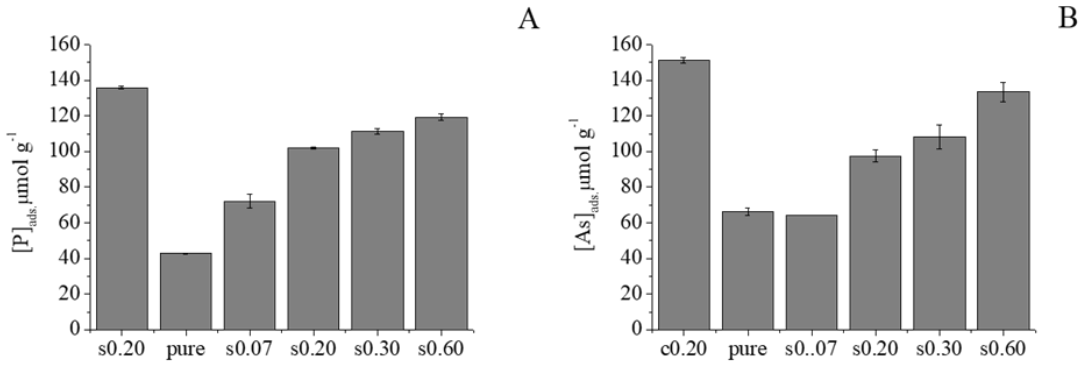

Figure 3.5 Comparison of phosphate and arsenate adsorption on Zn-sorbed and 0.2Zn co-precipitated δ-MnO_2 (error bars represent results from duplicate experiments). "c" stands for "Zn-coprecipitation" samples and "s" for "Zn-sorption" samples. Initial phosphate and arsenate concentrations are 100 µM.

3.4.3 Effect of Zn coprecipitation on the sorptive reactivity of δ-MnO_2

3.4.3.1 Mechanisms for cation adsorption on Zn-coprecipitated δ-MnO_2

Previous studies have shown that adsorbed Cd on Mn oxides existed as triple corner-sharing surface complexes below and/or above vacancy sites without incorporation into Mn oxide layers [2, 63, 78]. Zn coprecipitation with δ-MnO_2 can affect Cd uptake by modifying surface charges, particle size, and vacancy site density. In previous studies, the effects of metal coprecipitation with birnessite on mineral sorptive reactivity are metal-specific, possibly depending on the ratio of metal incorporation/(surface complexion + incorporation), with Co 90–100%, Ni 10–45%, Cu 0–20%, and Zn 0% [2, 74, 78]. Co coprecipitation with Mn oxides was shown to enhance Pb^{2+} adsorption on birnessite [14] and cryptomelane [7], and the authors proposed that Co substitution of Mn(IV) led to a more negatively-charged surface and more sorption sites (hydroxyl groups in CoOOH). Compared to Co, Ni coprecipitation with acid birnessite led to less Mn(IV) substitution (10–45% of Ni) vs surface sorbed species [74]. Surface-complexed Ni occupied surface

vacancy sites and decreased adsorption capacity towards Zn^{2+} and Pb^{2+} [61]. Similar to the effects of coprecipitation, pre-adsorbed metal cations can decrease Mn oxide sorption capacity toward Pb^{2+} [106, 163], Cu^{2+}, Zn^{2+}, and Cd^{2+} [163]. Zn was not observed to substitute or incorporate (0% of Zn) in δ-MnO_2 or phyllomanganate layers, due to the large atomic difference between Zn and Mn(III,IV) and crystal field stabilization energy [2, 74]. Therefore, Zn-coprecipitation could block surface vacancy sites, preventing further cation (e.g. Cd) adsorption. Zn also compensated δ-MnO_2 negative surface charges (Figure A.1), which also reduces the affinity between cations (e.g. Cd) and δ-MnO_2 surface.

This study shows that Zn coprecipitated δ-MnO_2 possesses larger sorptive capacity towards Cd than Zn-adsorbed δ-MnO_2 at similar or even higher Zn loadings, suggesting that Zn coprecipitation not only blocked surface vacancy sites, but also affected the structural properties of δ-MnO_2. Grangeon et al found that Zn sorption can expel Mn(III) within δ-MnO_2 layers [109], leading to more vacancy sites and potentially increased sorption capacity towards metal cations [151]. Our recent study found that Zn coprecipitation had significant effects on δ-MnO_2 structure, causing significantly reduced layer size and layer stacking and less Mn(III) occupation on vacancy sites[174]. These structural modifications might account for the higher total metal uptake by Zn-coprecipitated δ-MnO_2 than pure δ-MnO_2. Yu et al [84] also found more Zn uptake during biogenic Mn oxide formation compared to Zn sorption on pre-formed biogenic Mn oxides. It is likely that Zn inhibited the growth of fungal Mn oxides and resulted in lower crystallinity Mn oxides with higher metal uptake capacity. Previous study showed that metals such as Zn and Ni moved from interlayer vacancy sites to edge sites when interlayer sites were already occupied by pre-loaded metal cations [82]. In our study, Cd was likely to adsorb onto edge sites as well and Zn

coprecipitated δ-MnO_2 have more edge sites exposed to Cd with smaller particle size caused by Zn coprecipitation.

3.4.3.2 Solid phase analysis for anion adsorption on Zn-coprecipitated δ-MnO_2

XRD and As K-edge EXAFS were conducted to characterize the solid products from adsorption experiments, in order to explore the possible mechanisms underlying the effects of Zn coprecipitation on sorptive reactivity. Pure δ-MnO_2 were mixed with 2 mM Zn (higher than coppt0.20 Zn loading) and 200 μM phosphate (highest phosphate concentration used in this study), and no bulk precipitation was identified by XRD (Figure 3.6). The rising peak at 1.6–1.9 Å in the XRD spectra can be attributed to heavy metal occupation on vacancy sites [108].

Figure 3.7 shows the As EXAFS data of 100 μM arsenate sorption on 0.5 g L^{-1} pure and coppt0.20 δ-MnO_2. No significant differences were observed for the spectra of the two samples. Fourier transformed (FT) spectra showed two major peaks corresponding to As-O and As-Mn shells. Shell-by-shell fitting (Table 3.4) revealed ~4 oxygen atoms at ~1.69 Å, consistent with the tetrahedral coordination of arsenate [63, 182]. The second shell fitting indicated an As-Mn distance of 3.17–3.18 Å, suggesting the formation of bidentate binuclear complex of As on δ-MnO_2 surfaces, consistent with the previously reported 3.17–3.22 Å range [63, 182]. No additional δ-MnO_2-Zn-As ternary binding or other pathways were found. Thus the formation of ternary surface complexation and/or precipitation can be excluded during arsenate adsorption on Zn-coprecipitated δ-MnO_2. Previous EXAFS studies also found that no ternary complexes were formed between arsenate, Mn oxides, and adsorbed Zn/Pb [63] , or from the Mn(II) and arsenate produced during arsenite oxidation by Mn oxides [184], consistent with our studies.

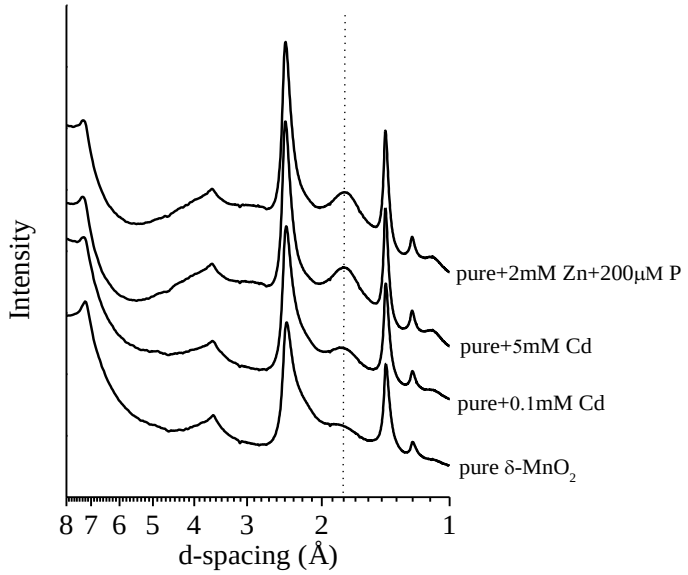

Figure 3.6 XRD of pure δ-MnO_2 and δ-MnO_2 with different treatments. Sample "pure + 2 mM Zn + 200 μM P" is pure δ-MnO_2 sample reacted with 2 mM Zn, filtered after 24 hours, briefly rinsed with DI, resuspended and reacted with 200 μM phosphate for another 24 hours. Solid loadings are all 0.5 g L^{-1}. pH was controlled at 6 using NaOH and HCl solutions, details described in text.

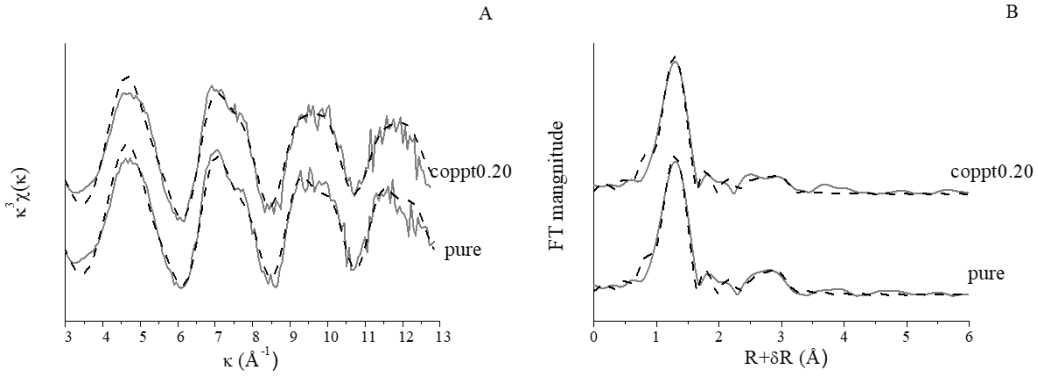

Figure 3.7 k^3-weighted As EXAFS (A) and Fourier transformed spectra (B, not corrected for phase shift) of arsenate sorption on pure and coppt0.20 δ-MnO_2 samples. Raw and fitted data are in solid and dotted lines, respectively.

Table 3.4 Shell-by-shell fitting results of As EXAFS for pure and coppt0.20 δ-MnO_2 samples.

Sample label	Shell	CN	Distance (Å)	σ^2
pure+As	As-O	4.1 (0.1)	1.699 (0.002)	0.003 (0.001)
	As-Mn	1.1 (0.1)	3.167 (0.001)	0.003 (0.001)
coppt0.20+As	As-O	4.1 (0.1)	1.694 (0.001)	0.003 (0.000)
	As-Mn	1.4 (0.1)	3.189 (0.001)	0.006 (0.001)

3.4.3.3 Mechanisms for anion adsorption on Zn-coprecipitated δ-MnO_2

Metal cations can influence phosphate and arsenate adsorption in several ways. First, pre-existing cations on δ-MnO_2 surface might compete with anions for adsorption sites. Yao et al proposed that Ca^{2+} and Mg^{2+} can suppress phosphate adsorption on hydrous Mn oxides by occupying surface sites and forming phosphate complexes in the solution [125]. Power et al found that adsorbed Zn slowed down arsenite oxidation by blocking δ-MnO_2 surface sites for arsenite complexation and electron transfer [62]. To verify the presence of competitive adsorption, we monitored the release of metals (Zn and total Mn) from the coppt0.20 sample equilibrated with 10 mM NaCl solution with or without 100 μM phosphate (Figure 3.8). Mn was not detected in the solution. Desorbed Zn was ~9 μM when 0.2coppt birnessite was equilibrated with 100μM phosphate and ~8 μM without P after 24 hours (Figure 3.8). Phosphate did not induce substantial Zn desorption, suggesting little competition between Zn and phosphate, likely due to the different sorption sites that they prefer. Zn adsorbs mostly at interlayer vacancy sites [109, 142], while anions such as phosphate, silicate, and sulfate are generally considered to complex at edge sites of

birnessite layers [138].

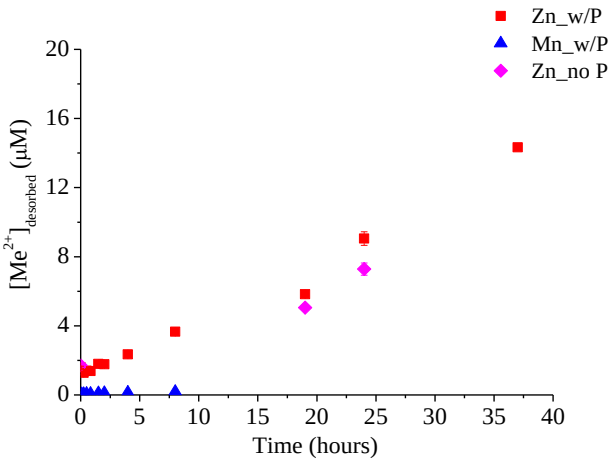

Figure 3.8 Release (desorption) of Zn and/or Mn from 0.5 g L^{-1} coppt0.20 δ-MnO_2 sample in the presence of 10 mM NaCl solution with or without 100 µM dissolved phosphate. pH was controlled at 6 using NaOH and HCl(no HEPES buffer).

Secondly, the presence of metal cations may compensate for the negative surface charge of δ-MnO_2, thus reduce the electrostatic repulsion between δ-MnO_2 surface and anions and enhance anion sorption. In general, anion uptake by negatively charged Mn oxides is limited, and anions are more likely to be associated with more positively charged Fe and Al (oxhydr)oxides [185-187]. However, charge compensation through cation adsorption/coprecipitation can significantly enhance anion adsorption on Mn oxides. Vilallobos et al found that Zn^{2+} and Pb^{2+} adsorption on δ-MnO_2 and birnessite enhanced the adsorption of arsenate [63]. Kawashima et al [172] found that co-existing Ca^{2+}, Mg^{2+}, Ba^{2+}, Sr^{2+}, Mn^{2+}, Co^{2+}, and Ni^{2+} greatly enhanced phosphate adsorption on hydrous Mn oxides over a wide range of pH. The order of enhancement by alkaline earth elements is Ba^{2+} > Sr^{2+} > Ca^{2+} > Mg^{2+}, suggesting that cations with smaller hydrated radii (i.e., higher charge

density) are more likely to promote anion adsorption. A previous study showed that in seawater (containing concentrated Ca^{2+}, Na^{+}, K^{+}, Mg^{2+}, and other metal cations), phosphate uptake by hydrous Mn oxides was comparable to that by goethite, and even higher than goethite at pH < 4 [125]. Mn(II)-rich hydrous Mn oxides were also shown to play important roles in As accumulation in Biwa lake sediments in Japan [188]. The study suggested that, since Mn oxides are important oxidants for arsenite, the resulting arsenate can accumulate on Mn oxide surfaces that are charge compensated by cations (Mn, Ni, and earth alkaline cations).

Thirdly, the common presence of metals during Mn oxide formation in the natural environment is likely to modify Mn oxide structure and enhance anion uptake ability, especially metals with limited incorporation into Mn oxide vacancy sites such as Zn and Ni [80]. As discussed above, adsorbed Zn was not as effective as coprecipitated Zn for the enhancement of phosphate and arsenate sorption on δ-MnO_2, due to the structural modifications by Zn-coprecipitation. Adsorbed Zn was shown to cause δ-MnO_2 dissolution and caused 15–20% reduction in lateral coherent domain size after ~12 hours at pH 5–7 [109]. Coprecipitated Zn caused even greater effects on δ-MnO_2 layer structure[174]. Reduced layer size can expose more available edges for anions, which mostly adsorb onto edge sites[63].

3.5 Conclusions

In this study, Cd was chosen as a cation probe while phosphate and arseante as anion probes to investigate the effects of Zn-coprecipitation on the sorptive reactivity of δ-MnO_2. Compared to pure δ-MnO_2, Zn-coprecipitated δ-MnO_2 phases are less negatively charged, and has a smaller layer size and less layer Mn(III) occupation on vacancy sites.

Pre-loaded Zn, either coprecipitated or adsorbed, inhibited Cd adsorption on δ-MnO_2, due to the competition between Zn and Cd. Total metal uptake (Zn+Cd) was enhanced as a result from the above-mentioned structural changes. Zn-sorbed δ-MnO_2 has a smaller Cd adsorption capacity than Zn-coprecipitated δ-MnO_2, even if the latter has less pre-loaded Zn. The charge-compensated Zn-δ-MnO_2 surface showed significantly enhanced sorptive capacity toward anions phosphate and arsenate. Higher sorption capacity, higher affinity, faster kinetics, and a right-shifted adsorption edge were observed for phosphate and arsenate sorption on Zn-coprecipitated δ-MnO_2, compared to pure δ-MnO_2. Compared to Zn-sorbed δ-MnO_2 samples, Zn-coprecipitation was more effective in enhancing anion sorption. No formation of ternary surface complex and/or precipitates were observed for phosphate and arsenate sorption on Zn treated δ-MnO_2. This study quantified the sorptive reactivities of Mn oxides under complex conditions that close to realistic environments and revealed the underlying mechanisms. Our study suggests that the roles of Mn oxides in regulating anion fate and transport should be re-visited by considering the impacts (e.g. structural modification, surface charge compensation) of metal presence during (i.e. coprecipitation) and after Mn oxide formation (i.e. sorption). Because the presence of metal cations during Mn oxide mineral formation can be a common environmental condition, our findings can help better understand the roles of Mn oxides in the biogeochemical cycles of nutrients, metals, and organic contaminants.

3.6 Acknowledgements

We acknowledge funding support from NASA grant #NNA15BB03A and NSF grant #1710285. We appreciate the support from beamline scientist Qing Ma at APS Beamline 5-BM-D. Portions of this research were conducted at the Advanced Photon

Source (APS). Use of the Advanced Photon Source was supported by the U.S. Department of Energy, Office of Science and Office of Basic Energy Sciences.

CHAPTER 4. EFFECT OF ZN COPRECIPITATION ON MN^{2+}-INDUCED REDUCTIVE TRANSFORMATION OF BIRNESSITE [3]

4.1 Abstract

Mn oxides are ubiquitous metal oxide minerals in nearly all environmental settings. They play important roles on the transport and fate of many environmental components such as metals, organics, and nutrients. In the presence of dissolved Mn^{2+}, Mn oxide phases can undergo ripening and transformation processes, resulting in the formation of phases with higher structural order, thus strongly affect the reactivity of Mn oxides over extended time scale. In natural environments, metal cations can strongly interact with Mn oxides, yet much still remain unknown about the effect of metal coprecipitation on the transformation process of Mn oxides. This study investigates the effects of Zn coprecipitation on Mn^{2+}-induced reductive transformation of birnessite, a common Mn oxide mineral phase. Pure and Zn-coprecipitated acid birnessite phases were synthesized and their transformation kinetics and pathways in the presence of Mn^{2+} was investigated under oxic or anoxic conditions. During the transformation process, Zn-coprecipitated birnessite showed higher capability toward Mn^{2+} uptake, likely due to smaller particle size and the fast consumption of Mn^{2+} and precipitation of a new phase hetaerolite. The formation of an intermediate phase, feitknechtite, was faster for Zn-coprecipitated birnessite than pure birnessite, which is the opposite of Zn-sorbed birnessite system. Transformation from the intermediate phase feitknechtite to the final stable phase manganite was slower for Zn-coprecipitated birnessite, due to the lower Mn^{2+}

[3] Shiliang Zhao, Yaneira A. Gonzáez-Valle, Evert J. Elzinga, Emily M. Saad, Yuanzhi Tang. Effect of Zn(II) coprecipitation on Mn(II)-induced reductive transformation of birnessite. *Chemical Geology*. Under review.

concentration which catalyzed the transformation. This study revealed the importance of understanding the influence of metal cation impurities on the structural stability and long-term reactivity of Mn oxide minerals.

4.2 Introduction

Mn oxides are ubiquitous metal oxide minerals in nearly all environmental settings, such as fresh waters, marine nodules, soils, and sediments [122, 131, 132]. Mn oxides are generally produced through the oxidation of Mn^{2+}, and this process is much faster when catalyzed by mineral surfaces, microorganisms [18], or reactive oxygen species (ROS) [30, 56]. The predominant type of initial Mn oxide phase formed at circumneutral pH is a highly disordered nanocrystalline phyllomanganate phase that is structurally similar to hexagonal birnessite [30, 36, 42, 48]. This phase is highly reactive due to the high surface area, negative surface charge, and large amount of vacancy sites [18]. Dissolved Mn^{2+} ions can be adsorbed onto the vacant sites and react with structural Mn(IV) to produce Mn(III) [25, 26, 55, 58], resulting in the ripening and transformation of the hexagonal birnessite phases and the formation of phases with higher structural order [27, 57]. Such reductive transformation can strongly affect the sorptive and redox reactivity of the Mn oxides. For example, newly produced Mn(III) can incorporate at the vacancy sites of Mn oxides and decrease the sorption capacity toward metal cations (e.g. Pb^{2+}, Cu^{2+}, Zn^{2+}, and Cd^{2+}) [151]. Mn(III)-bearing minerals are less reactive compared to Mn(IV)-bearing minerals toward the adsorption of As(III, V) [189]. The availability of Mn(III) in Mn oxide structure are also important during the oxidation of Cr(III) by Mn oxides [6, 105].

The reductive transformation process is controlled by factors such as Mn^{2+} concentration, pH, and the presence of oxygen (O_2). Biotic and abiotic hexagonal birnessite

was found to react with low concentration of Mn^{2+}, and the newly formed Mn(III) can order within the layer structure and change the layer symmetry from hexagonal to triclinic [25, 26, 58]. With higher Mn^{2+} concentrations, hexagonal birnessite can transform to manganite (γ-MnOOH) at pH 7.0–8.0 and hausmannite ($Mn^{II}Mn^{III}_2O_4$) at pH 8.0–8.5, both with the presence of an intermediate phase feitknechtite (β-MnOOH) under anoxic conditions [110, 112]. Under oxic conditions, birnessite can react with concentrated Mn^{2+} and precipitate nsutite (γ-$Mn^{III,IV}(O,OH)_2$) and ramsdellite (MnO_2) at pH 2.4, cryptomelane ($K_{1.3-1.5}Mn^{III,IV}_8O_{16}$) at pH 4.0, groutite (α-MnOOH) at pH 6.0, and feitknechtite and manganite at pH 7–7.5 [47, 91]. The presence of oxygen generally increases the uptake of Mn^{2+} by birnessite, due to surface catalyzed oxidation of Mn^{2+} by O_2 in addition to the electron transfer reaction between Mn^{2+} and birnessite [110, 112].

Birnessite minerals have high affinities for metal cations due to their low point of zero charge (PZC) [18, 29] and negatively charged surface across a wide range of pH conditions. Adsorbed and/or incorporated metal impurities in birnessite are likely to affect the above-mentioned transformation processes. A few studies have examined the effect of metal sorption and/or presence on the reductive transformation process. Ni adsorption on biotic birnessite [58] were shown to inhibit the formation of Mn(III) and favor the hexagonal symmetry; whereas Na and Ca presence during the transformation of biotic Mn oxides can stabilize layer Mn(III) and favor the triclinic symmetry [58]. Zn adsorption on birnessite was found to slow down the transformation from birnessite to feitknechitite under anoxic condition [111].

Coprecipitation of metals (Ni, Zn, Fe, and Co) are known to modify birnessite structural properties (e.g. average oxidation state, surface area, vacancy site density) [14, 61,

[79, 80, 136]. For example, Zn coprecipitation with fungal Mn oxides was shown to interrupt the layer stacking along **c*** direction and result in thinner flake-shaped particles [84]. Our recent study also showed that Zn coprecipitation with abiotic phyllomanganates (δ-MnO_2 and birnessite) resulted in generally smaller particle size (e.g. reduced layer stacking and/or lateral layer size) [174]. Such effects were previously observed for Zn adsorption on Mn oxides [109], but were not as significant as the Zn coprecipitation systems [174]. However, despite the commonly observed structural modifications induced by metal coprecipitation with Mn oxides and the obvious environmental relevance, no studies have investigated how the structural modifications caused by metal coprecipitation would influence the long-term reductive transformation processes of Mn oxides.

In this study, we systematically compared the Mn^{2+}-induced transformation kinetics and pathways of pure birnessite and Zn-coprecipitated birnessite, and compared the effects to a previous study on the transformation of Zn-adsorbed birnessite [111]. To our knowledge, this is also the first study on the effects of Zn-birnessite interaction on birnessite reductive transformation under oxic conditions. Results of this study help understand how metal impurities could affect the long term Mn oxide transformation and thus Mn geochemical cycling in natural environment.

4.3 Methods

4.3.1 Synthesis of pure and Zn-coprecipitated acid birnessite

Acid birnessite was synthesized following a previous study [34] by adding 45 mL of 6 mol L^{-1} HCl to a boiling 300 mL of 0.667 mol L^{-1} $KMnO_4$ solution under vigorous stirring. For Zn coprecipitated birnessite samples, calculated amount of $ZnSO_4$ was mixed with the HCl solution before the addition of $KMnO_4$, to achieve a $Zn:Mn_{total}$ molar ratio of 0.01, 0.1,

and 0.2. These samples are labeled as 0.01cppt, 0.1cppt, and 0.2cppt birnessite, respectively. At the end of reaction, the suspension was allowed to cool down and settle. The brown precipitates were collected by vacuum filtration (0.2 μm), washed and dialyzed with deionized (DI) water, and freeze dried. A portion of the solids were digested by aqua regia and measured for Zn and Mn concentrations using inductively coupled plasma–mass spectrometry (ICP-MS).

4.3.2 Mn^{2+}-induced transformation of birnessite phases

Parallel experiments were conducted to investigate the kinetics and pathways of Mn^{2+}-induced reductive transformation of pure and Zn-coprecipitated birnessite under oxic or anoxic conditions. For oxic experiments, 20 mg of pure or Zn-coprecipitated birnessite was suspended in a 200-mL solution containing 20 mM HEPES and 10 mM NaCl, with a solids/liquid ratio of 0.1 g/L. pH of the suspension was adjusted to 7.5 using NaOH and HCl solutions. The suspension was ultrasonicated for 3 min and equilibrated for 3 h by shaking at 150 rpm. To initiate the reaction, 200 μL of 1 M $MnSO_4$ stock solution was added to the suspension to achieve 1 mM Mn^{2+} concentration. Reaction bottles were consistently agitated on an orbital shaker at 150 rpm for 18 d. At certain reaction time, aliquots of the reaction suspension were collected and vacuum filtered (0.22 μm). Mn^{2+} concentration in the filtrate was determined using a colorimetric method [190] on a UV-vis spectrometer (Cary 60, Agilent). Zn^{2+} concentration was analyzed using ICP-MS. Filtered solids were repeated rinsed with DI water and freeze dried for later structural characterization. For anoxic experiments, all reactions were conducted inside a glove box (Coy) filled with 95% N_2 and 5% H_2. All solutions used for the experiments were boiled and cooled down under N_2 bubbling before transferring into the glove box. The

transformation experiments above were conducted under dark conditions (bottles warped with aluminum foil). The effect of light was also investigated using transparent plastic bottles under ambient lab lighting with other conditions same as above.

4.3.3 Solid phase characterization

A suite of complementary techniques were conducted to analyze the morphology and structure of the pure and Zn coprecipitated birnessite, as well as their transformation products. X-ray diffraction (XRD) analysis was conducted using a Panalytical Empyrean multipurpose diffractometer with Cu Kα radiation. Fourier transformed infrared (FT-IR) spectroscopy analysis was conducted on a Bruker Vertex 80 V spectrometer using KBr pellets at 800–1250 cm^{-1}. FTIR spectra were normalized by the highest peak intensity in each spectrum, according to previous studies [110-112]. High resolution transmission electron microscopy (HRTEM) experiments were conducted on a JEOL 2010F TEM. Solid samples were suspended in ethanol and ultrasonicated for 1 min then a single drop of the suspension was added on a 200-mesh Cu grid with a holey-carbon support film and air dried. Image focus was obtained on the carbon film adjacent to the particles of interest to avoid beam damage, then the beam was moved to the sample for image collection.

For Mn and Zn K-edge XAS analysis, wet pastes of the synthesized birnessite samples were vacuum filtered using a 0.22 μm membrane, rinsed with DI water, and mounted in an acrylic sample holder covered with Kapton tape. Samples were stored at -20 °C before analysis. XAS experiments were conducted at Beamline 4-1 at Stanford Synchrotron Radiation Lightsource (SSRL, Menlo Park, CA) and beamlines 5-BM-D and 12-BM-B at Advanced Photon Source (APS; Argonne National Laboratory, Lemont, IL). Energy calibration used the corresponding Mn or Zn metal foil. Spectra of reference foils

were collected simultaneously with sample scans. XAS data were collected in both fluorescence and transmission mode at room temperature using a Vortex detector (APS 5-BM-D) or a 13 element Ge solid-state detector (APS 12-BM-B and SSRL 4-1). Both X-ray absorption near edge structure (XANES) and extended X-ray absorption fine structure (EXAFS) data were collected. Reference compounds (feitknechtite, manganite, pure and Zn substituted hausmannite and hetaerolite) were from Lefkowitz et al [111].

XAS data processing and analysis used the programs SIXpack [57] and Ifeffit [191]. Multiple scans (2–6) were energy calibrated and averaged for further analysis. Principal component analysis (PCA) was conducted on the normalized sample spectra to determine the number of components needed for obtaining reasonable fits. Using the corresponding reference compound spectra library, target transformation (TT) was conducted to determine appropriate candidate compounds. Linear combination fitting (LCF) was conducted on the EXAFS region. Combinations of TT-determined candidate compounds were used, and the goodness of fit was determined by R-factor. Fits with smallest R-factors were used.

4.4 Results and Discussion

4.4.1 Effects of Zn-coprecipitation on birnessite properties

HRTEM images of pure and 0.2cppt birnessite samples are presented in Figure 4.1. Both samples showed amorphous to low crystallinity particles with great aggregation, but in general smaller particle size was observed in Zn birnessite. XRD patterns of the unreacted pure and Zn birnessite was shown in Figure 4.3 (t = 0). The peaks (001) and (002) at ~13° (labeled as “B”) and 24°can provide an overall estimation of the thickness of birnessite particles. With Zn coprecipitation, both peaks became lower and broader,

indicating less layer stacking. A previous study also reported that Zn inhibited fungal Mn oxide growth and resulted in thinner flake particles [84]. Grangeon et al found that Zn sorption onto δ-MnO_2 caused oxide dissolution and smaller coherent domain size [109]. Coprecipitation of other heavy metals (e.g. Ni, Co, Cu, and Fe) was also previously shown to influence the crystallization of abiotic [14, 61, 80, 109] and biotic [84] birnessite, producing birnessite particles with less stacking layers and/or smaller layer dimension, i.e., overall smaller particle size.

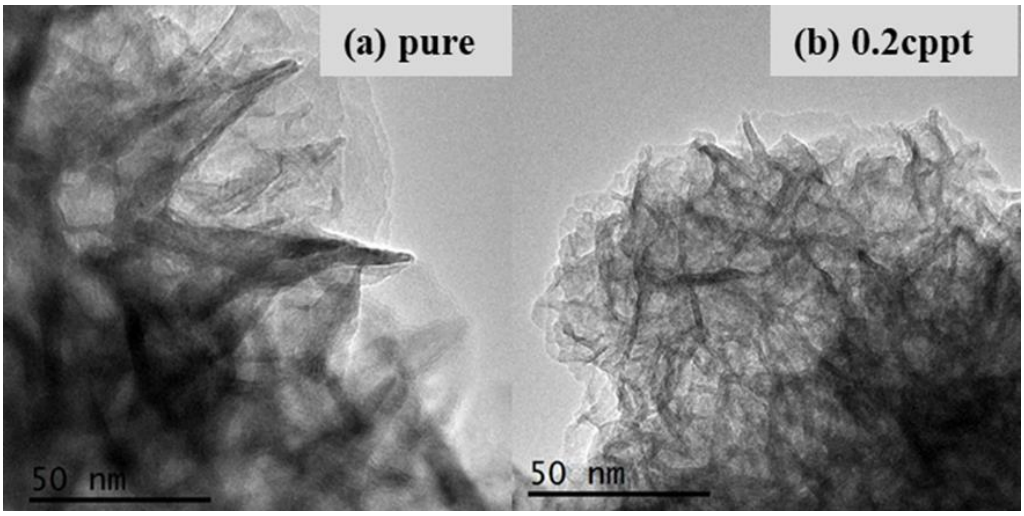

Figure 4.1 HRTEM images of pure and Zn coprecipitated acid birnessite.

Both pure and Zn birnessite solids were analyzed by digestion and ICP-MS to obtain the Zn and total Mn contents. According to the results in Table 4.1, Mn contents were barely changed by Zn addition while K^+ contents were significantly reduced. Previous studies showed that adsorbed [2, 74, 78] or coprecipitated [84] Zn did not substitute Mn atoms in the layer, but was adsorbed above or below the layer vacancy sites, replacing interlayer K^+ [78], and have minimum effects on Mn contents. Therefore, when the solid

concentrations were controlled as described above, Mn concentrations were also controlled in both pure and Zn coprecipitated systems.

Table 4.1 Concentrations of dissolved Mn^{2+} in the reaction solution, as well as total Mn, Zn, and K contents (from ICP-MS) in pure or Zn-birnessite samples before and after 18 d reaction under anoxic or oxic conditions. To better compare with dissolved Mn^{2+} concentration, concentrations of total Mn, Zn, and K in birnessite were converted to mM by normalizing the contents by total liquid volume.

Reaction condition	Birnessite phase	$[Mn^{2+}]_{aq}$ (mM)		[Mn(IV)] (mM)		[Zn] (mM)	[K] (mM)
		t = 0	t = 18 d	t = 0	t = 18 d		
Anoxic	Pure	1.0	0.44	0.76	0.20	0	0.27
	0.2cppt	1.0	0.26	0.72	0	0.12	0.04
Oxic	Pure	1.0	0.09	0.76	-	0	0.27
	0.2cppt	1.0	0.11	0.72	-	0.12	0.04

4.4.2 Transformation of pure birnessite under anoxic condition

When Mn^{2+} reacted with pure birnessite under anoxic condition, Mn^{2+} was instantly adsorbed onto birnessite vacancy sites at interlayer and edge regions before further reactions occur [63, 111, 112]. This is consistent with the fast decrease of Mn^{2+} concentration in our system after adding Mn^{2+} to both pure birnessite and Zn-birnessite systems (Figure 4.2A). Figure 4.3 shows the XRD data of solid products during the 18-day transformation process. After Mn^{2+} addition, peak B decreased along with the growth of other peaks, indicating that adsorbed Mn^{2+} reacted with birnessite and produced new mineral phases. Previous study also found that HEPES buffer can react with birnessite, causing partial dissolution of birnessite and production of Mn^{2+} [192]. After comparison with XRD spectra of reference compounds (details in Text S1 and Figure C.1), the growing peaks belong to feitknechtite (β-MnOOH), which indicates electron transfer from Mn^{2+} to structural Mn(IV), producing Mn(III)-containing mineral phase (Eq. 2), consistent with the results of

previous studies [110-112]. Two bands at 1067 and 946 cm^{-1} in FT-IR spectra (Figure 4.4) resulting from OH bending [110-112] confirm the existence of feitknechtite. Feitknechtite production likely continuously decreased Mn^{2+} concentration in the following 5 days in under anoxic condition. The growth of feitknechtite peaks, as presented by the signature sharp peak "F" at ~19°, also lasted until ~day 5 of reaction, consistent with the decreasing Mn^{2+} concentration in Figure 4.2A.

$$Mn^{2+}{}_{(aq)} + MnO_{2\,(s)} + 2\,H_2O \rightarrow 2\,\beta\text{-}MnOOH_{\,(s)} + 2\,H^{+}{}_{(aq)} \qquad \text{(Eq. 2)}$$

Mn^{2+} concentration reached a steady state after 5 days and remained unchanged (~0.44 mM) in the next 13 days. At this stage (day 5-18), peak "F" gradually disappeared with the growth of new peaks such as the peak "M" at ~29°. These new peaks belong to a more stable Mn(III)-containing phase manganite (γ-MnOOH, Eq. 3). Three appearing bands at 1150, 1116, and 1087 cm^{-1} in FT-IR data [110-112] confirms the transformation from feitknechtite to manganite [110-112]. This process does not consume Mn^{2+}, resulting in a steady state Mn^{2+} concentration from day 5 to 18. The ratio between initial Mn^{2+} (1 mM) and Mn(IV) concentrations (0.76 mM) is larger than the 1:1 Mn^{2+}/Mn(IV) stoichiometry in Eq. 1, but ~0.20 mM Mn(IV) remained in the solids after 18-day reaction (Table 4.1). This is probably due to the newly formed Mn-bearing phases preventing the further reaction between birnessite and Mn^{2+}.

$$\beta\text{-}MnOOH_{\,(s)} \rightarrow \gamma\text{-}MnOOH_{\,(s)} \qquad \text{(Eq. 3)}$$

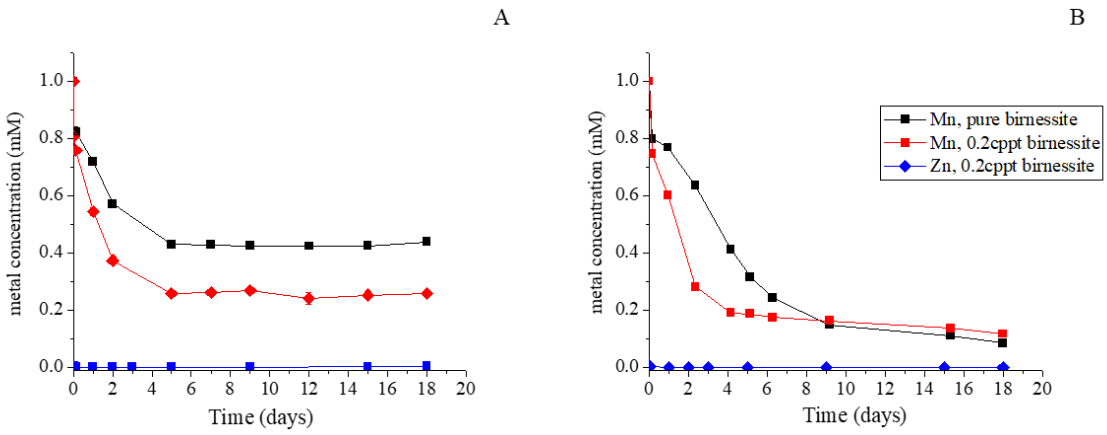

Figure 4.2 Concentrations of dissolved Mn^{2+} and Zn^{2+} in the reaction suspension during the reductive transformation of pure or 0.2cppt-birnessite under (A) anoxic and (B) oxic conditions at pH 7.5.

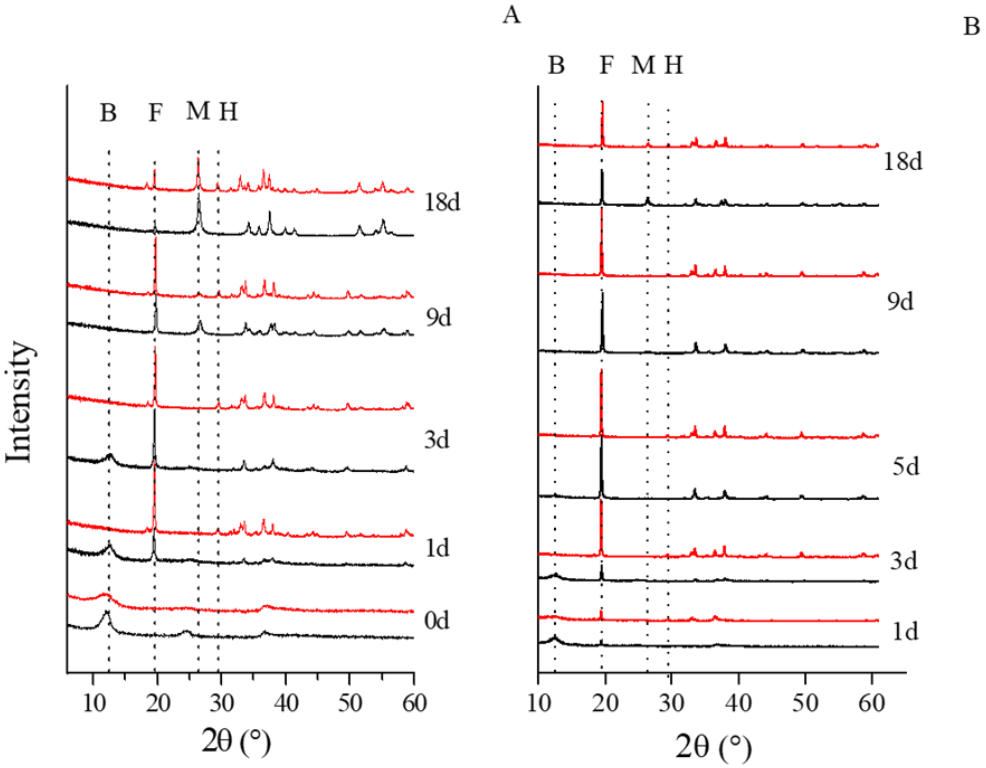

Figure 4.3 XRD spectra of pure (black) and Zn coprecipitated birnessite (red, 0.2cppt) samples after reaction under (a) anoxic and (b) oxic conditions at pH 7.5 for 18 days. "B", "F", "M" and "H" indicate the peak positions for birnessite, feitknechitite, manganite, and hetaerolite, respectively.

4.4.3 Transformation of pure birnessite under oxic condition

Under oxic conditions, Mn^{2+} concentration decreased fast during the first few days, similar to the observed trend in the anoxic condition (Figure 4.2B). This fast decrease was mostly attributed to Mn^{2+} adsorption and reaction with birnessite. Mn^{2+} concentration was continuously reduced, compared to reaching a steady state concentration under anoxic condition. The continuous removal of Mn^{2+} from the solution is likely due to surface-catalyzed oxidation of Mn^{2+} by oxygen under oxic conditions according to Eq. 4 [110-112]. Mn^{2+} oxidation by oxygen is kinetically slow at neutral pH [18], but faster when catalyzed by Mn-oxide mineral surfaces (i.e., birnessite and feitknechtite in this study) [110]. At day 9, both the XRD patterns (Figure 4.3) and the normalized FT-IR spectra (Figure 4.4) showed a higher content of feitknechtite but little manganite in the oxic system compared to the anoxic system. At day 18, there was still a significant amount of feitknechtite remaining in the oxic system, whereas nearly all feitknechtite transformed to manganite at day 9 under anoxic conditions. This is because feitknechtite was produced through Mn^{2+} oxidation by both birnessite (i.e. direct oxidation) and oxygen (i.e. mineral catalyzed oxidation) in the oxic system, whereas Mn^{2+} oxidation was only through birnessite (direct oxidation) in the anoxic system. [110-112] Feitknechtite was continuously produced in the presence of oxygen and mineral surfaces throughout 18 days, whereas under anoxic condition the production stopped at ~day 5. In addition, the transformation from feitknechtite to manganite was also catalyzed by Mn^{2+}. Low Mn^{2+} concentration (after day 5) might have accounted for the slow transformation rate of feitknechtite to manganite under oxic condition.

$$4\ Mn^{2+}{}_{(aq)} + O_{2\ (aq)} + 6\ H_2O \rightarrow 4\ \beta\text{-}MnOOH_{\ (s)} + 8\ H^{+}{}_{(aq)} \qquad \text{(Eq. 4)}$$

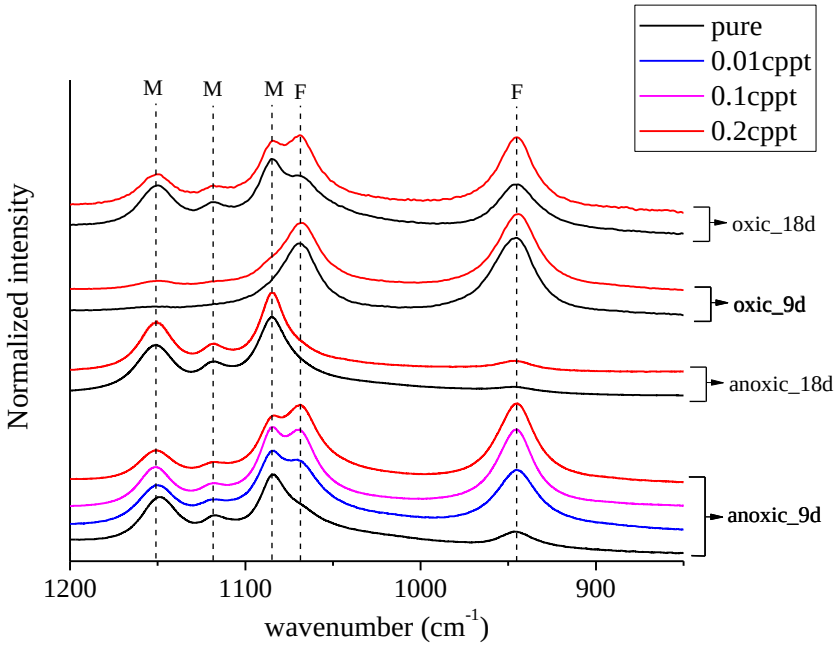

Figure 4.4 FTIR spectra of pure and Zn coprecipitated birnessite samples after reaction under anoxic and oxic conditions at pH 7.5. "F" and "M" stand for feitknechitite and manganite.

4.4.4 Transformation of Zn-coprecipitated birnessite under oxic and anoxic conditions

Parallel experiments were conducted on pure and Zn coprecipitated birnessite under oxic vs. anoxic and light vs. dark conditions. Under light vs dark conditions, no significant difference was observed in Mn^{2+} concentrations (Figure C.3) and solid phase structure (Figure C.4). Under oxic vs anoxic conditions, the effects of Zn-coprecipitation on the transformation process showed similar trends, and are discussed below.

4.4.4.1 Hetaerolite precipitation

Based on XRD data in Figure 4.3 (t = 0), Zn coprecipitation did not cause the formation of additional phases other than birnessite. k^3-weighted Zn EXAFS data and Fourier transformed spectra of 0.2cppt birnessite are shown in Figure 4.5. Shell-by-shell

fitting results in our recent study [174] showed that Zn mostly existed in octahedral configuration and as surface adsorbed species. In previous studies [111, 135], it was shown that Zn^{2+} and Mn^{2+} strongly compete during adsorption. Pre-adsorbed Zn^{2+} can decrease birnessite sorption capacity towards Mn^{2+} at pH 6 [111]. At low Mn^{2+} loading, Mn^{2+} can replace pre-adsorbed Zn^{2+} on birnessite and δ-MnO_2 vacancy sites at pH 4 [135]. However, in this study with high Mn^{2+} concentration (1 mM) and higher reaction pH (7.5), no desorbed Zn^{2+} (i.e. aqueous Zn) was observed in both anoxic and oxic systems throughout the 18-day reaction, even within the first few minutes (Figure 4.2). On the other hand, compared to pure birnessite system, Zn coprecipitated birnessite showed a much faster Mn^{2+} sequestration rate under both anoxic and oxic conditions. Under anoxic condition, a lower steady state Mn^{2+} concentration was reached after 5 days. Because Zn-coprecipitation produced birnessite phases with smaller particle size, the subsequent increase in surface area might have contributed (at least partially) to the faster Mn^{2+} uptake as compared to the pure birnessite system.

Besides feitknechtite and manganite, XRD data of Zn coprecipitated system showed additional peaks at ~18°, 29°, and 33 °(Figure C.1). These peaks correspond to a new phase hetaerolite ($ZnMn^{III}_2O_4$), formed by Zn coprecipitation with newly produced Mn(III), as shown in Equation 4. Hetaerolite production was previously observed in systems involving Zn and Mn redox reactions [85, 111]. The precipitation of hetaerolite also consumed Mn^{2+} and Mn(IV) at a 1:1 ratio, same as feitknechtite production in Equation 1. Based on mass balance calculation (Table 4.1), the reaction in the pure systems was not complete. Both Mn(IV) and Mn^{2+} remained at stable stage. In comparison, nearly all Mn(IV) in Zn coprecipitated birnessite was consumed after 18 days. Mn(III) in solutions readily

undergoes disproportionation into Mn^{2+} and Mn(IV) [18, 39, 58]. The precipitation of feitknechtite and hetaerolite in this study removed Mn(III) from solutions and preserved it. Previous study showed that hetaerolite acted as a stronger sink of Mn(III) compared to feitknechtite [111], consistent with the complete consumption of Mn^{2+} and Mn(IV) in the anoxic Zn systems. The rapid precipitation of hetaerolite relative to feitknechtite may be another cause of the faster Mn^{2+} uptake by Zn coprecipitated birnessite.

$$Mn^{2+}{}_{(aq)} + MnO_{2\,(s)} + Zn^{2+}{}_{(aq)} + 2\,H_2O \rightarrow ZnMn^{III}{}_2O_{4\,(s)} + 4\,H^+{}_{(aq)} \quad \text{(Eq. 5)}$$

Figure 4.5 shows the k^3-weighted Zn EXAFS data and Fourier transformed spectra of initial Zn birnessite and the transformation products under anoxic condition. Pure hetaerolite was also plotted as a reference compound. Zn-birnessite and hetaerolite have distinct features at 6~12 Å in k space, especially the peaks at ~6.5 and 8.5 Å. The evolution of both peaks suggests the gradual transformation from surface adsorbed Zn to hetaerolite. Linear combination fitting of Zn EXAFS was conducted using hetaerolite and Zn-coprecipitated birnessite as the end members, and the results are shown in Figure 4.6 and Table C.1. The fitting results suggested a very fast transformation, with more than 60% of the adsorbed Zn precipitated in hetaerolite within the first 3 hours. This is consistent with the strong Mn(III)-removal ability of hetaerolite as discussed above. In k space EXAFS spectra, the 3-hour sample already resembled the spectra of hetaerolite. This fast transformation also explains why no desorbed Zn^{2+} was detected in the solution.

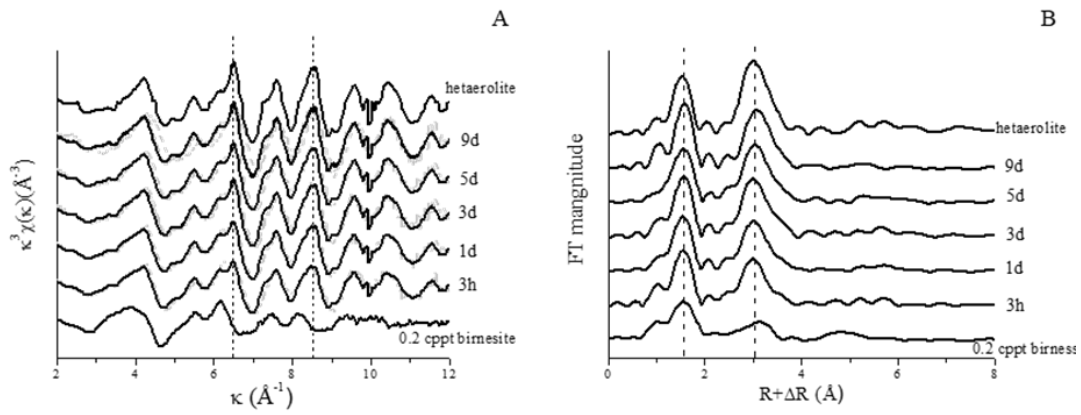

Figure 4.5 k^3-weighted Zn EXAFS (A) and Fourier transformed (B) spectra (not corrected for phase shift) of 0.2cppt birnessite anoxic transformation products. Raw and fitted data are in solid and dotted lines, respectively.

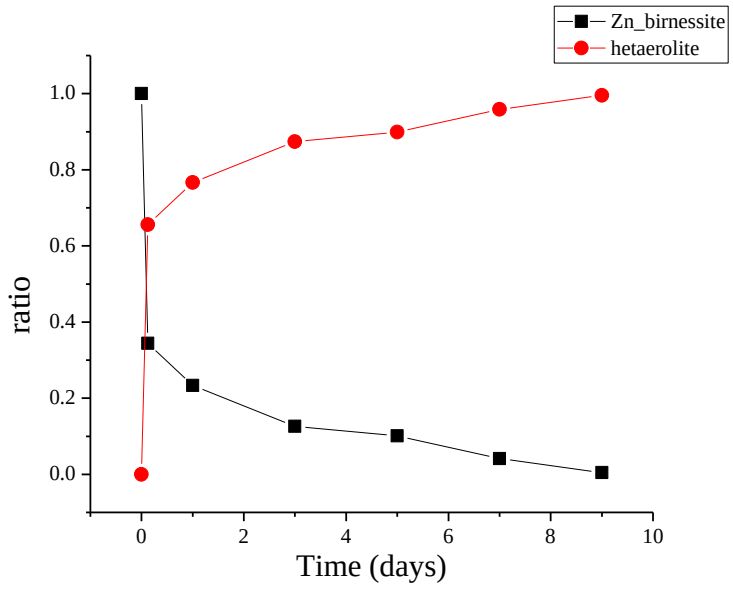

Figure 4.6 Fractional composition of 0.2cppt birnessite transformation products from linear combination fitting results of k^3-weighted Zn EXAFS.

Table 4.2 Linear combination fitting results of Zn EXAFS data on the 0.2cppt birnessite transformation products.

Reaction time (days)	Zn_birnessite (%)	Hetaerolite (%)	R factor	χ^2
0	100	0	0.09	6
0.125	34	66	0.09	5
1	23	77	0.08	6
3	13	87	0.10	11
5	10	90	0.07	6
7	4	96	0.15	39
9	0	100	0.09	6

4.4.4.2 Effect of Zn coprecipitation on the formation of feitknechtite

"F" peaks in XRD (Figure 4.3) and FT-IR (Figure 4.4) spectra present the gradual production then consumption of feitknechtite along the 18-day reaction time. The initial F peaks in XRD are stronger in Zn-coprecipitation system under both anoxic and oxic conditions, indicating that feitknechtite production is faster from Zn-coprecipitated birnessite than from pure birnessite. Zn coprecipitation could affect feitknechtite production under anoxic conditions in several ways. Firstly, Zn sorption on birnessite surfaces could lower the affinity of Mn^{2+} towards birnessite. In previous studies, pre-sorbed metal cation on Mn oxides surface modified surface charge and blocked surface sites, preventing further reaction between birnessite and other species. Ni coprecipitation with birnessite was found to decrease Pb and Zn adsorption [61]. Adsorbed Zn on birnessite surface slows down the oxidation of As(III) by birnessite [62]. Secondly, hetaerolite precipitation was fast (within minutes) and consumed the newly-produced Mn(III), acting as a stronger Mn(III) sink than feitknechtite. None of the two factors discussed above favored feitknechtite precipitation in systems with birnessite pre-loaded with Zn. In fact, Lefkowitz et al [111] conducted similar transformation study using Zn adsorbed birnessite and found slowed-down feitknechtite precipitation by adsorbed Zn, in contrast to the results.

The accelerated transformation to feitknechtite within the first 5 days in Zn-coprecipitation systems is like due to the birnessite structural modification by Zn coprecipitation (as discussed in section 4.4.1). Higher surface area possibly resulted in fast Mn(III) production from the reaction between Zn-coprecipitated birnessite and Mn^{2+}. The accumulation of feitknechtite was thus more significant in the Zn-coprecipitation system, despite the competition with hetaerolite precipitation. Previous studies showed that Co-coprecipitation with birnessite enhanced the oxidative capacity of birnessite towards As(III) [14], and Co coprecipitation with cryptomelane also enhanced has Cr^{3+} oxidation (due to larger surface area and higher average oxidation states) [7]. In this study, Zn coprecipitated birnessite exhibited enhanced uptake and oxidative ability toward Mn^{2+}, suggesting the potential enhancement of oxidative capacity of the solid, which warrants further investigation.

Under oxic conditions, the faster feitknechtite formation in Zn-coprecipitation system could also result from a faster mineral surface-catalyzed Mn^{2+} oxidation by oxygen. Mn oxides have been widely used as an effective catalyst and the catalytic reactivity is influenced by chemical composition and structure [193-195]. Metal impurities in Mn oxides (e.g. alkali [193, 195], alkaline earth [193], and heavy metals [137, 196, 197]) generally enhance the catalytic capacity of Mn oxides. The mechanisms vary and are metal specific, such as expanded interlayer distance by alkali cations [195], increased surface area and average oxidations state by Fe [137], and enhanced surface hydroxyl group by Co [14, 193]. In this study, the smaller particle size of the Zn-coprecipitated birnessite possibly enhanced the efficiency of the oxide for catalyzing Mn^{2+} oxidation by oxygen, contributing to the faster Mn^{2+} removal from solution and feitknechitite production under oxic condition.

4.4.4.3 Effect of Zn coprecipitation on the formation of manganite

"M" peaks in XRD (Figure 4.3) showed continuous transformation from feitknechtite to more stable manganite. This process did not changed Mn^{2+} concentration under anoxic condition [112]. Despite modified kinetics of feitknechtite production and hetaerolite precipitation in Zn-coprecipitation systems, Mn^{2+} concentration reached steady state at similar times (~5 days) as the pure birnessite systems (Figure 4.2A). This suggests that the precipitation of both feitknechtite and hetaerolite was almost finished after ~5 days. Linear combination fitting of Zn EXAFS that showed ~90% Zn precipitated as hetaerolite after 5 days, with continuous slow precipitation until almost 100% Zn precipitation at ~day 9. The normalized FT-IR spectra of solids after 9-day and 18-day transformation are shown in Figure 4.4. Almost all feitknechtite was replaced by manganite in the pure birnessite system after 9 days. With increasing Zn/Mn_{total} ratio from 0 to 0.2, the fraction of residual feitknechtite increased. After 18 days, manganite became the dominant phase in both pure and Zn-coprecipitation systems. However, there are still some remaining feitknechtite in the 0.2cppt birnessite system, suggesting that increasing Zn loading slowed down the transformation to manganite. This lower rate is likely due to the lower concentration of solution Mn^{2+} in the Zn-coprecipitation systems (Figure 4.2), which was previously shown to be proportional to manganite production rate [112].

Similar phenomena were also observed under oxic conditions where more feitknechtite remained in the 0.2cppt birnessite system than in the pure birnessite system after 18 days. However, the dissolved Mn^{2+} concentration was almost the same in pure and Zn-coprecipitation systems from day 9 to 18, and this period was the primary time for feitknechtite transformation to tunnel structured manganite. Three factors might have contributed to the slow formation of manganite in Zn-coprecipitation system. Firstly, the

availability of interlayer K^+ was important during Mn oxide transformation from layered to tunneled structure by significantly reducing the energy barrier and speeding up the transition [198]. In this study, K^+ content in birnessite was significantly reduced by Zn coprecipitation (Table 4.1). Therefore, it is possible that the formation of manganite in the Zn-coprecipitation systems was less favored with less K^+ buckling the sheets and stabilizing the tunneled structure [198]. Secondly, feitknechtite transformation was prohibited by adsorbed Ni [199]. Metal cations such as Ni and Zn were also found to slow down the transformation of ferrihydrite to more stable phases (e.g. goethite and hematite) [200-202]. These studies suggested that Fe/Mn (oxyhydr)oxide transformation were prohibited by the bonds between Fe/Mn and adsorbed metals [199, 202, 203]. Similar Zn-Mn bonds might also preserved feitknechtite in our study. Thirdly, Zn might block feitknechtite surface and compete with Mn^{2+} and interfere with the catalytic function of Mn^{2+} in feitknechtite transformation to manganite [199].

4.5 Conclusion and Environmental Implications

In this study, the effects of Zn coprecipitation on Mn^{2+}-induced birnessite transformation was explored. Zn coprecipitated birnessite has smaller particle size compared to pure birnessite. During the interaction with Mn^{2+}, compared to the pure birnessite system, a new Zn-containing mineral phase (hetaerolite) was formed in the Zn-coprecipitation system, modifying the transformation pathway and increasing Mn^{2+} removal and Mn(IV) consumption. Compared to Zn sorption on birnessite, the Zn coprecipitation system showed different transformation kinetics. Accelerated feitknechitite precipitation suggested enhanced redox and catalytic reactivity of Zn- coprecipitated birnessite.

Considering the common association of metal cations (e.g. Zn) with MnOx in natural environments, further investigations are warranted to explore the effect of metal-coprecipitation on Mn oxide structure modification, subsequent influence on Mn oxide transformation pathways and kinetics, as well as the influence of environmental factors (e.g. oxygen level, pH, Mn^{2+} concentration). Such information can help better understand the roles of Mn oxides in the fate and transport of a range of elements, as well as the Mn cycle itself. Since Mn oxides are also widely used as oxidants and catalysts, the modified redox and catalytic property of metal-coprecipitated Mn oxides can provide information on the design and selection of targeting phases for environmental remediation and catalytic applications.

4.6 Acknowledgement

This research is supported by NASA under Grant #NNA15BB03A and NSF under Grant #1710285. We appreciate the support from beamline scientists Qing Ma (APS 5BM), Benjamin Reinhart and Sungsik Lee (APS 12BM), and Ryan Davis (SSRL 4-1). Portions of this research were conducted at the Advanced Photon Source (APS) and Stanford Synchrotron Radiation Lightsource (SSRL). APS is a U.S. Department of Energy (DOE) Office of Science User Facility operated for the DOE Office of Science by Argonne National Laboratory under Contract No. DE-AC02-06CH11357. Use of SSRL, SLAC National Accelerator Laboratory, is supported by DOE Office of Science, Office of Basic Energy Sciences under Contract No. DE-AC02-76SF00515.

CHAPTER 5. COMPARISON OF ZN COORDINATION ENVIRONMENTS DURING ZN ADSORPTION OR COPRECIPITATION WITH MN OXIDES

5.1 Introduction

Phyllomanganates (e.g. birnessite and vernadite) are layered Mn oxide minerals and are among the most abundant Mn minerals in soils and marine nodules [1, 67, 204]. Most phyllomanganate minerals exist as rock / mineral coatings or discrete particles in soils [1, 67]. Surface charge of phyllomanganates are generally negative under circumneutral pH conditions due to the absence of Mn(IV) atoms or substitution of Mn(IV) by Mn(III) or other cations with lower oxidation states [14, 60, 61]. The void Mn(IV) sites (i.e. vacancy sites) are highly reactive for a wide varity of sorption or redox reactions [28, 65, 205]. Metal sequestration by phyllomanganate are significant due to the large surface area, negative surface charges, and large amount of vacant sites [67].

Zn is among the common transition metals that are found to associate with Mn oxides in natural environments, such as in ocean marine nodules, soils, and contaminated systems [8, 118-120]. Zn concentrations in natural Mn oxides are typically low. Zn/Mn molar ratio was found to be 0–0.5% in Sicilian [118] and New Zealand marine nodules [119] and Mississippi Basin soils [120]. This ratio was 3% in coal mine drainage treatment systems and can be as high as 46% in contaminated sediments [122]. Zn mostly existed as adsorbed species when associated with natural [8, 120, 130, 206, 207] or synthetic abiotic [62, 78, 82, 111, 140, 142] and biotic [73, 84, 139] phyllomanganate Mn oxides. No Zn incorporation into layer structure was previously observed due to the large atomic difference between Zn and Mn(III,IV), as well as the crystal field stabilization energy Zn required to incorporate into layer structure

[2, 74]. Earlier studies found that Zn formed tri-corner-sharing (TCS) complexes above or below the vacancy sites at interlayer region when Zn was adsorbed on abiotic and biotic phyllomanganate surfaces [78, 82, 84, 139, 140, 142]. More recent studies found that Zn also bonds to phyllomanganate edges by forming double-corner-sharing (DC) complexes [82, 109], especially when interlayer vacancy sites were occupied by Mn(II, III) [82]. Adsorbed Zn can exist in two coordination environments [2, 142]: 1) tetrahedrally coordinated (^{IV}Zn) with three oxygen atoms from Mn oxides and one oxygen atom from water molecules; 2) octahedrally coordinated (^{VI}Zn) with three oxygen atoms from Mn oxides and three oxygen atoms from water molecules, see Figure 5.1. ^{VI}Zn-TCS species have longer Zn-O (~2.10 Å) and Zn-Mn distances (~3.50 Å) as compared to ^{IV}Zn-TCS (~1.97 and 3.35 Å, respectively) [2, 82, 142]. These characteristics are commonly used to differentiate ^{IV}Zn and ^{VI}Zn.

The factors that influence the ^{IV}Zn/^{VI}Zn ratio during Zn sorption on Mn oxides have been extensively studied. Firstly, ^{IV}Zn predominantly forms at low Zn loadings on phyllomanganate surface while ^{VI}Zn is favored at high Zn loadings [2, 73, 78, 82, 139]. Kwon et al revealed that ^{IV}Zn is more efficient compared to ^{VI}Zn when compensating for the negative surface charges of Mn oxides [142], which probably explains why ^{IV}Zn is favored at low Zn loadings. As discussed above, Zn/Mn ratio is low in most natural environments and correspondingly most Zn associated with natural Mn oxides are ^{IV}Zn, e.g. >90% in Baltic sea nodules [130] and ~100% in Mn oxide sand coatings at a Zn/Mn ratio of 0.0138 [8]. The amount of ^{IV}Zn is considerably lower at Zn contaminated sites, e.g. ~75% in contaminated phyllomanganate nanoparticles in grass roots [122]. Secondly, a density function theory (DFT) study revealed that interlayer ^{VI}Zn was stabilized by the water molecules at the interlayer mid-plane and oxygen atoms at the vacancy sites of Mn oxide

surface [142]. Well-crystallized phyllomanganate with larger layer size and well-stacked layers should be able to hold more ^{VI}Zn at interlayer region. In fact, Grangeon et al found that ^{VI}Zn in acid birnessite was twice more than that in δ-MnO_2 [109], which has smaller and incoherently stacked layers than the former [28]. Thirdly, theoretical DFT calculations showed that ^{IV}Zn is more efficient to compensate for negative surface charges thus it was believed that phyllomanagnate with more vacancy sites (i.e. more negative surface) favored the formation of ^{IV}Zn [109, 142]. In contrary, Hinkle et al found that occupation of vacancy sites by Mn(III) pushed Zn to edge site forming DC complexes and DC favors the formation of ^{IV}Zn [82]. More detailed study is required to study the relationship of vacancy site amount in phyllomanganate with Zn coordination environments.

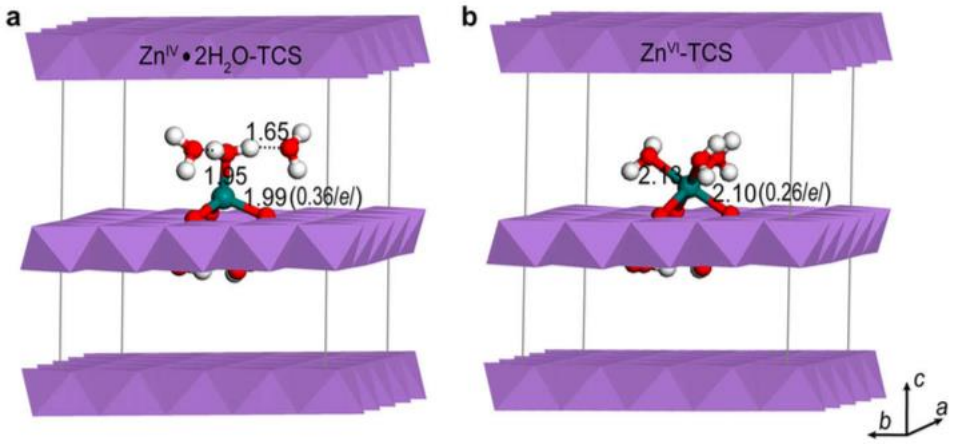

Figure 5.1 Geometry-optimized (a) isolated ^{IV}Zn–TCS (b) isolated ^{VI}Zn–TCS, taken from Kwon 2009 [142]. Zn atoms are marked as green, oxygen atoms as red and hydrogen as white balls. Three water molecules were plotted in (a) but only one is coordinated with Zn atoms and the rest two are related to the coordinated water molecule with H bonds. Bond lengths of Zn-O in this figure are calculated values for isolated species and might differ from the actual values in real cases.

Although the Zn coordination during Zn adsorption has been well explored, there are still questions about the Zn coordination with phyllomanganate in real environmental samples. Marcus et al found that in a growing ocean nodule, nearly all Zn was ^{IV}Zn regardless of various Zn/Mn ratio at different nodule bands [122, 130]. Lanson et al reported a combination of ~75% ^{IV}Zn and ~25% ^{VI}Zn in Zn contaminated ferromanganese soil samples (with Zn/Mn ratio of 0.46) [122]. At such high Zn loading, high ^{VI}Zn amount was expected according to the trend in previous studies but only ~25% ^{VI}Zn was observed. Considering that the formation of natural Mn oxide can likely occur in the presence of Zn, it is likely that coprecipitated Zn can have coordination environments that do not follow the trend for Zn sorption on pre-formed Mn oxides. On the basis of the results discussed above, it seems that ^{VI}Zn is not favored during Zn coprecipitation with Mn oxides. In fact, Yu et al found that ^{VI}Zn contents stayed unchanged with increased Zn loadings when Zn coprecipitated with fungal Mn oxides, while ^{VI}Zn increased with higher Zn loadings during sorption on pre-formed fungal Mn oxides [84]. The Zn coprecipitation system differs from the Zn sorption system in many ways, such as the existence of competing Mn^{2+}, layer stacking interruption by Zn coprecipitation, and large Zn/Mn ratios at the initial stage. All these factors might influence the formation of ^{VI}Zn species. This study systematically investigated Zn coordination environments during Zn sorption on and coprecipitation with several representative abiotic and biotic phyllomanganate phases (δ-MnO_2, acid birnessite, and bacterial Mn oxides) with different crystallinity, layer size, and formation conditions. Combined with the structural modifications by Zn sorption and coprecipitation as revealed in previous chapters, ^{VI}Zn/^{IV}Zn formation mechanisms during Zn coprecipitation were explored.

5.2 Methods

5.2.1 Preparation of biogenic Mn oxide samples

Biogenic Mn oxides (bioMnOx) were prepared through the extracellular oxidation of Mn^{2+} by *Roseobacter* sp. Azwk-3b [37, 55, 56]. Calculated amount of salts was dissolved to prepare artificial sea water (ASW) containing 0.3 mol L^{-1} NaCl, 0.05 mol L^{-1} $MgSO_4$, 0.01 mol L^{-1} $CaCl_2$, and 0.01 mol L^{-1} KCl. K growth media (pH 7.2) containing 75 % (volume percentage) ASW, 20 mM HEPES buffer, 2 g L^{-1} peptone, and 0.5 g L^{-1} yeast extract was used for *R*. Azwk-3b cultivation. *R*. Azwk-3b was grown in K growth media at 30 °C and 150 rpm to mid-exponential phase ($OD_{600} \approx 0.22$, Figure 5.2). Cell-free filtrate was obtained by centrifuging the growth suspension at 10,000 rpm and filtering the supernatant with 0.45 μm sterile membrane. 100 μM Mn^{2+} was added immediately to the cell-free filtrate and oxidized by the extracellular superoxide in the filtrate [56]. Zn coprecipitated bioMnOx was obtained by adding calculated amount of $ZnSO_4$ together with Mn^{2+} to achieve a Zn/Mn ratio of 0.01–0.50, within the Zn/Mn range in natural environments discussed above. The concentration of Mn(III, IV) oxides during bioMnOx production was measured using the leucoberbelin blue (LBB) colorimetric assay on an UV-vis spectrophotometer (Cary 60, Agilent). Mn^{2+} concentration was measured using the method described in Chapter 4 [190]. The mixing speed during Mn^{2+} oxidation varied at 150, 250, and 300 rpm to investigate the effects of oxygen diffusion on bioMnOx production. BioMnOx were harvested after 24–327 h by centrifuging the suspension at 11,000 rpm for 20 min and rinsed with DI water.

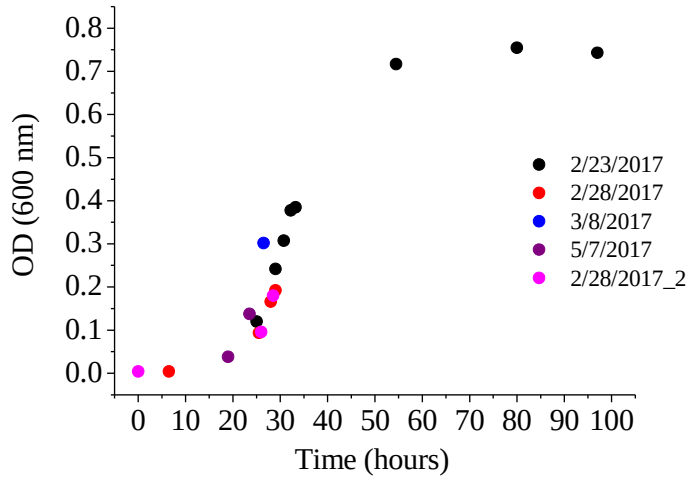

Figure 5.2 *Roseobacter* sp. Azwk-3b growth in 30 mL K growth media in 250 mL flask at 30 °C and 150 rpm. The dates labeled are starting dates of different batches.

5.2.2 Preparation of abiotic Mn oxide samples

Synthesis of Zn-coprecipitated δ-MnO_2 and acid birnessite were described in Chapter 2. Zn adsorbed Mn oxides were obtained by equilibrate 0.5 g L^{-1} Mn oxides with calculated amount of $ZnSO_4$ to achieve a Zn/(total Mn) ratio of 0.005–0.50. pH was controlled at 7.2 using NaOH and HCl solutions. After 24 h, the suspension was filtered using a 0.2 μm membrane and washed with DI water for future analysis. The reference compound chalcophanite ($ZnMn_3O_7 \cdot 3H_2O$) was synthesized through ion exchange between layered brinessite and high concentration of $ZnSO_4$ [208]. A small amount of Zn (Zn/Mn = 0.005) was adsorbed on δ-MnO_2 and served as a Zn tetrahedral reference compound. Zn EXAFS data collection and analysis procedures were described in detail in Chapter 2.

5.3 Results and Discussion

5.3.1 Biogenic Mn oxide production by Roseobacter sp. Azwk-3b

Fast increase of Mn(III, IV) oxide concentrations was observed after Mn^{2+} addition due to Mn^{2+} oxidation by superoxide species produced by *Roseobacter* sp. Azwk-3b in Figure 5.3 [36, 37]. The growth of Mn(III, IV) oxides slowed down gradually over time, indicating reduced superoxide concentrations in the solutions. Newly-formed bioMnOx by *Roseobacter* sp. Azwk-3b have been previously identified as amorphous hexagonal phyllomanganate phases that are structurally similar to δ-MnO_2 or hexagonal birnessite. This initial bioMnOx phase is highly reactive and can catalyze Mn^{2+} oxidation by oxygen, leading to continuous increase of Mn(III, IV) oxide concentration [18, 29, 36, 37, 55]. Learman et al also proposed that the organics in organic-rich K growth medium can react with oxygen under light conditions, producing reactive oxygen species (ROS) that might also continuously oxidize Mn^{2+} [37]. The involvement of oxygen might also explain the higher bioMnOx production at higher mixing rates (Figure 5.3B).

Mn K-edge EXAFS of bioMnOx after 24 and 327 h are shown in Figure 5.4. The 24-hour spectra in k space has sharp peaks at ~8.10 and 9.25 Å, indicating a hexagonal Mn oxide phase with vacancy site but little Mn(III) contents[28, 34]. These tow peaks of spectra of 327-hour sample were broadened, indicating the transition of layer symmetry from hexagonal to triclinic, consistent with previous studies [26, 37, 55, 130, 152]. Mn^{2+} reacted with structural Mn(IV) and the newly-formed Mn(III) incorporated into layer vacancy sites and changed layer symmetry [26, 58]. In Figure 5.4(B), the FT spectra showed two dominate peaks at ~1.5 and 2.5 Å, corresponding to Mn-O and Mn-Mn edge-sharing (Mn-Mn_{edge}) shells. As bioMnOx aged from 24 to 327 hours, both Mn-O and Mn-Mn_{edge} peaks broadened and the peak height ratio $H_{Mn\text{-}Mn(edge)}/H_{Mn\text{-}O}$ also decreased. Webb et al attributed

the peak broadening to Jahn-Teller distortions caused by increased layer Mn(III) which split the Mn-Mn peak and decreased the amplitude [54].

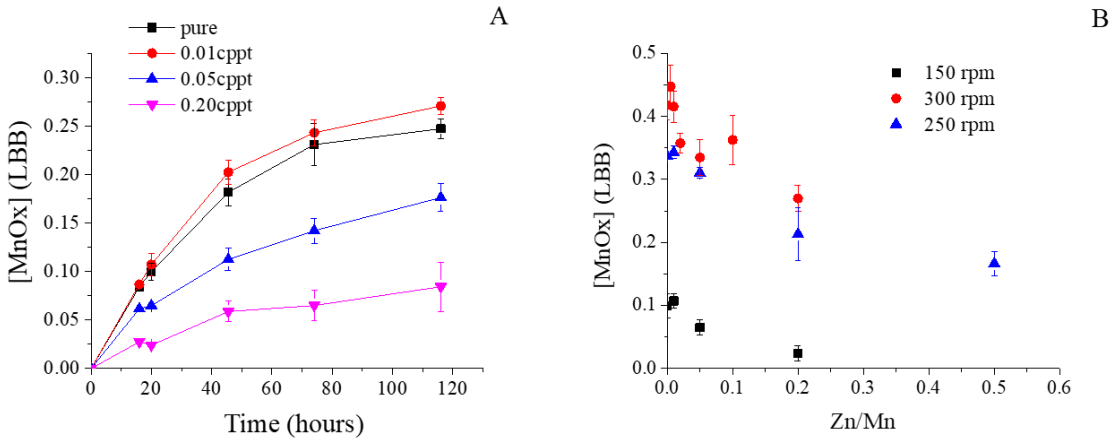

Figure 5.3 Mn(III, IV) oxide concentration in the cell free filtrate in the presence of varied Zn concentration and at 150 rpm mixing rate (A), and under different mixing rate at 24 hour reaction time (B).

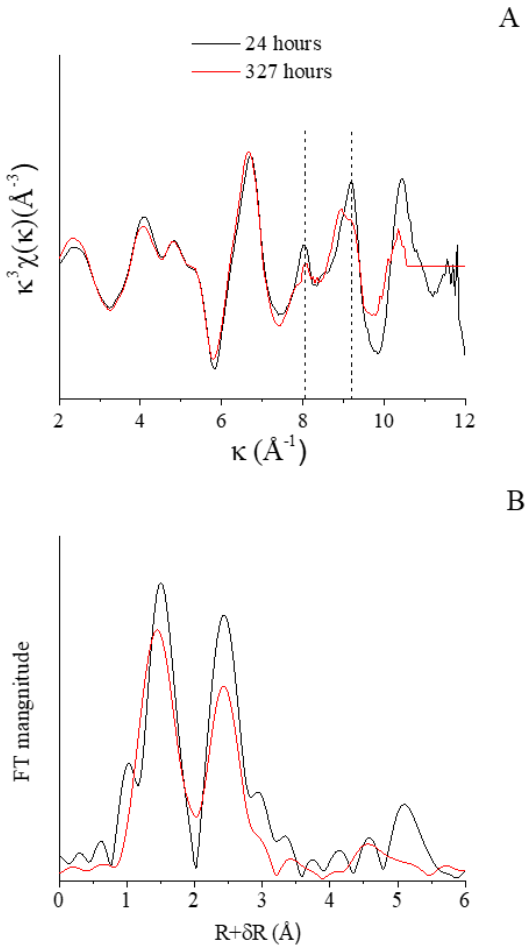

Figure 5.4 k^3-weighted Mn K-edge EXAFS (A) and Fourier transformed (FT) spectra (B, not corrected for phase shift) of pure bioMnOx harvested after 24 and 327 hours. Stirring speed was controlled at 150 rom at room temperature. Vertical dashed lines highlight the indicator region.

5.3.2 Effects of Zn presence on biogenic Mn oxide production

Low Zn (0.01 cppt) amounts did not show obvious influences on bioMnOx production (Figure 5.3). Zn contents higher than 0.05 cppt decreased the Mn^{2+} oxidation rates and the reduction was more significant with increased Zn/Mn ratio. The prohibition caused by Zn presence was also observed at higher stirring speed at 250 rpm and 300 rpm, see Figure 5.3(B). The addition of Cu stimulated biotic Mn^{2+} oxidation by *Leptothrix*

discophora SS-1 [45] through facilitating the production of multi-copper oxidase (MCO). During Mn^{2+} oxidation by *R.* sp Azwk-3b, Cu slowed down bioMnOx formation by catalysing superoxide dismutation [56, 209, 210]. Zn does not catalyze superoxide dismutation [56] and the slow bioMnOx production in Zn systems might result from the bioMnOx structural disturbance by Zn, as seen in the cases of synthetic Mn oxides discussed in Chapter 2. Zn could block surface vacancy sites and prevent Mn^{2+} adsorption on bioMnOx surface when bioMnOx catalyse Mn^{2+} oxidation by oxygen [37]. Grangeon et al also showed Zn equilibrium caused dissolution of synthetic vernadite[109] and same effects might also account for the lower bioMnOx concentration compared to pure systems. On the other hand, Figure 5.5 showed the picture of pure and 0.2 Zn/Mn coprecipitated bioMnOx produced after 24-hour cultivation. In pure system, bioMnOx exist as colloids in solutions; while much larger bioMnOx aggregates were observed in 0.2 Zn system. Mn oxides are generally negatively charged [67] and the electrostatic repulsion made pure bioMnOx colloids well dispersed in the solutions. Adsorbed [62] and coprecipitated (Figure A.1) Zn compensated the negative surface charges and caused great aggregation of bioMnOx. These heavily aggregated bioMnOx particulates might not be as reactive as colloidal bioMnOx when catalysed Mn^{2+}oxidation [37].

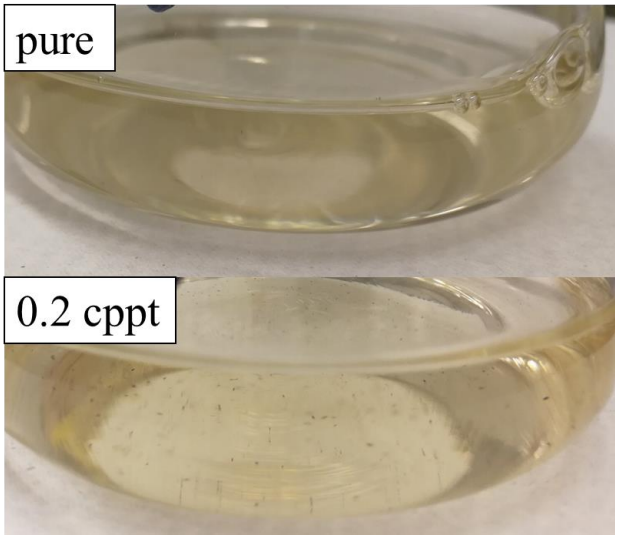

Figure 5.5 Pictures of pure and 0.2-cppt bioMnOx after 24 hours at 150 rpm and room temperature.

k^3-weighted Mn K-edge EXAFS and Fourier transformed (FT) spectra of pure and Zn-coprecipitated bioMnOx after 24 hours are shown in Figure 5.6. The general features in pure bioMnOx at both k space and R space were preserved in 0.01-0.20 cppt samples, indicating the short-range Mn coordination environment was not significantly changed by Zn coprecipitation. The indicator region from 8-10 Å in k^3-weighted Mn K-edge EXAFS spectra is sensitive to the layer Mn(III) contents. Since Mn(III) incorporates into vacancy sites, the Mn(III) contents have been used to predict the vacancy site density in phyllomanganate layers [174]. Layer Mn(III) could broaden, or even split with high Mn(III) contents, the two peaks at ~8.10 and 9.25 Å, such as triclinic birnessite with no vacancy sites and significant amount of Mn(III) [28, 58, 60]. Both peaks became sharper with increasing coprecipitated Zn amount, consistent with our findings in Zn coprecipitated δ-MnO_2. The ratio of $H_{Mn\text{-}Mn(edge)}/H_{Mn\text{-}O}$ in FT space was also increased with Zn contents showing less

layer Mn(III) contents in Zn coprecipitated bioMnOx, consistent with the k^3-weighted Mn EXAFS spectra.

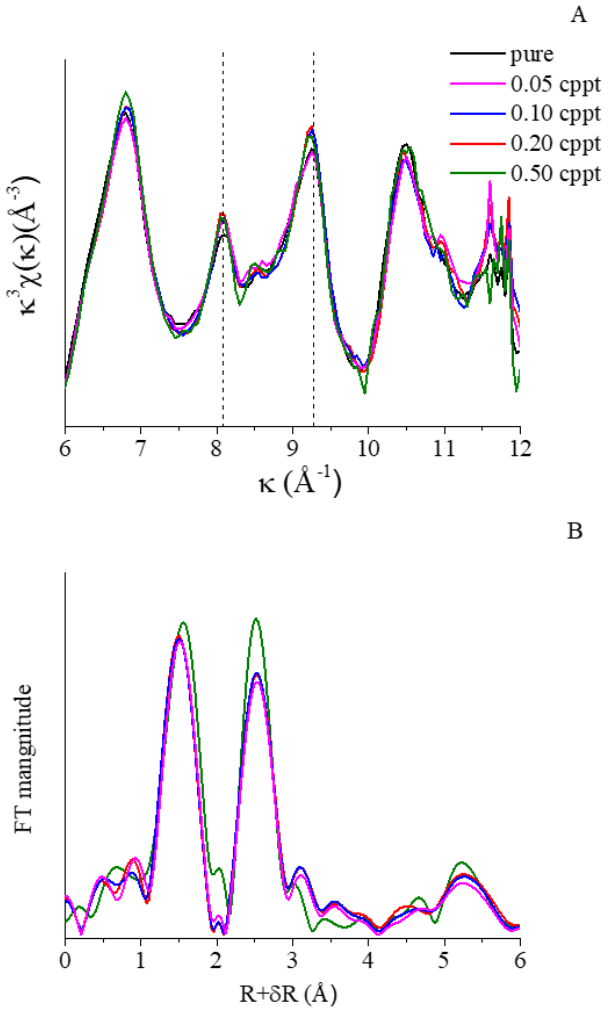

Figure 5.6 k^3-weighted Mn K-edge EXAFS (A) and Fourier transformed (FT) spectra (B, not corrected for phase shift) of pure and Zn-coprecipitated bioMnOx after 24 hours. Stirring speed was controlled at 150 rom at room temperature Vertical dashed lines highlight the indicator region.

Table 5.1 Sample abbreviations and conditions used in Zn EXAFS analysis.

Labels	Zn/Mn	Treatments	Mn oxides	Time (hours)
0.5Zns-bir	0.005	Adsorption	Acid birnessite	24
1Zns-bir	0.01	Adsorption	Acid birnessite	24
5Zns-bir	0.05	Adsorption	Acid birnessite	24
20Zns-bir	0.20	Adsorption	Acid birnessite	24
50Zns-bir	0.50	Adsorption	Acid birnessite	24
1Zn-bir	0.01	Coprecipitation	Acid birnessite	-
5Zn-bir	0.05	Coprecipitation	Acid birnessite	-
10Zn-bir	0.10	Coprecipitation	Acid birnessite	-
20Zn-bir	0.20	Coprecipitation	Acid birnessite	-
0.5Zns-dMn	0.005	Adsorption	δ-MnO_2	24
1Zns-dMn	0.01	Adsorption	δ-MnO_2	24
2Zns-dMn	0.02	Adsorption	δ-MnO_2	24
5Zns-dMn	0.05	Adsorption	δ-MnO_2	24
50Zns-dMn	0.50	Adsorption	δ-MnO_2	24
1Zn-dMn	0.01	Coprecipitation	δ-MnO_2	-
5Zn-dMn	0.02	Coprecipitation	δ-MnO_2	-
10Zn-dMn	0.10	Coprecipitation	δ-MnO_2	-
20Zn-dMn	0.20	Coprecipitation	δ-MnO_2	-
1Zn-bio-24	0.01	Coprecipitation	bioMnOx	24
2Zn-bio-24	0.02	Coprecipitation	bioMnOx	24
5Zn-bio-24	0.05	Coprecipitation	bioMnOx	24
20Zn-bio-24	0.20	Coprecipitation	bioMnOx	24
50Zn-bio-24	0.50	Coprecipitation	bioMnOx	24
1Zn-bio-327	0.01	Coprecipitation	bioMnOx	327
5Zn-bio-327	0.02	Coprecipitation	bioMnOx	327
20Zn-bio-327	0.20	Coprecipitation	bioMnOx	327

5.3.3 Characterization of Zn coordination reference compounds

Reference compounds with pure ^{IV}Zn or ^{VI}Zn coordination environment were required to compare with our sample qualitatively and analyse quantitively using linear combination fitting (LCF) methods. Chalcophanite ($ZnMn_3O_7$) has 100% ^{VI}Zn and serves as a Zn octahedral reference compound in this and previous studies [2, 73, 109, 122, 206]. The formation of ^{IV}Zn is favoured at low Zn loadings. In several previous studies, Mn oxides with low Zn loadings (^{IV}Zn birnessite with Zn/Mn=0.008 [2], ^{IV}Zn bioMnOx with Zn/Mn= 0.007 [109, 139] and natural ocean nodules [130]) were fully tetrahedral and used as ^{IV}Zn reference compounds. δ-MnO_2 with even less Zn loading (Zn/Mn=0.005, 0.5Zns-dMn) was prepared as a Zn tetrahedral reference compounds in this study. Figure 5.7 showed the k^3-weighted Zn K-edge EXAFS of these two references. The spectra of ^{VI}Zn shifted to the left compared to the spectra of ^{IV}Zn, which attributed to the longer distances between Zn and other atoms [139]. Signals at high k range were noisy in ^{IV}Zn spectra and the peaks at low k ranges (3-4 Å and 5-6 Å, indicated by the dashed lines in Figure 5.7) were generally used to differentiate two Zn coordination [2, 84, 109, 122, 130, 139]. Shell-by-shell fitting of 0.5Zns-dMn Zn EXAFS yielded a coordination number (CN) 3.8 and distance (R) 1.97 Å for Zn-O (Table 5.3), confirming fully tetrahedral Zn coordination in 0.5Zns-dMn. The results were consistent with previous ^{IV}Zn references mentioned above: CN 3.3 and R 1.97 for ^{IV}Zn birnessite [2], CN 4.4 and R 1.97 for ^{IV}Zn bioMnOx [139] and CN 4.9 and R 1.96 Å for natural ocean nodules [130]. Shell-by-shell fitting of chalcophanite Zn EXAFS yielded a CN 5.5 and R 2.07 Å for Zn-O (Table 5.3), confirming the octahedral Zn coordination in chalcophanite [2, 109, 130, 139].

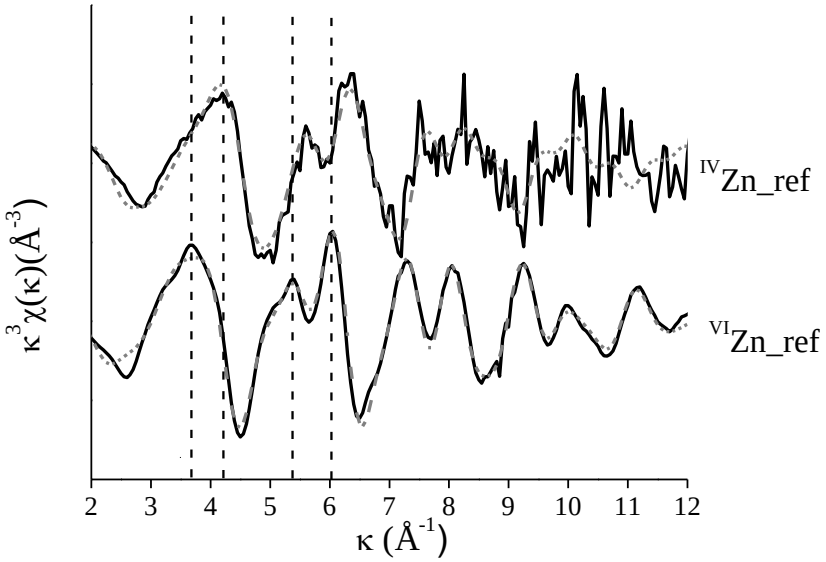

Figure 5.7 K^3-weighted Zn K-edge EXAFS of chalcophanite and 0.5Zns-dMn. Raw and shell-by-shell fitted data are in black solid and gray dotted lines, respectively. The vertical dash lines indicated the main differences of two reference compounds.

5.3.4 Zn coordination during adsorption on δ-MnO_2 and acid birnessite

Zn coordination during adsorption on synthetic Mn oxides has been extensively studied. Zn adsorbed acid birnessite andδ-MnO_2 were also prepared and analysed in order to compare with the effects of Zn coprecipitation. Figure 5.8 (A) and (b) show the k^3-weighted Zn EXAFS spectra of Zn adsorbed samples with ^{IV}Zn and ^{VI}Zn references. In Figure 5.8 (A), all spectra of Zn adsorbed δ-MnO_2 samples showed similar features to ^{IV}Zn, in spite of a wide range of Zn/Mn ratio from 0.01 to 0.50. With increased Zn loading, the peak at ~3.8-3.9 Å slightly shifted to left, indicating increased ^{VI}Zn contents. The double peaks at 5-7 Å also became less resolved with more Zn added. This is probably because the presence of ^{VI}Zn split and broadened the peaks [84]. Linear combination fitting (LCF) was conducted using chalcophanite and 0.5Zns-dMn as two end-members and the results

were listed in Table 5.2 and plotted in Figure 5.8. The contents of ^{VI}Zn in Zn adsorbed δ-MnO_2 increased from 11.9% for 1Zns-dMn to 27.1 for 50Zns-dMn, consistent with Zn EXAFS spectra discussed above. The increase of ^{VI}Zn contents with higher Zn loadings were widely observed during Zn adsorption in previous studies [2, 109, 130, 139]. ^{IV}Zn is more effective compensating the negative surface charges of Mn oxides and the formation of ^{IV}Zn is favoured at low Zn loadings [109, 142].

The spectra of Zn adsorbed acid birnessite changed more dramatically with increasing Zn contents, compared to δ-MnO_2. The spectra of 0.5Zns-bir was similar to ^{IV}Zn while 5Zns-bir was already resembling ^{VI}Zn. At 3-4 Å, the spectra of 1Zns-bir showed two splitting peaks indicating the transition from ^{IV}Zn to ^{VI}Zn at this Zn loading. LCF showed large increase of ^{VI}Zn contents from 61.7% for 0.5Zns-bir to 100% for 5Zns-bir. Shell-by-shell fitting was conducted on Zn EXAFS data of Zn adsorbed acid birnessite samples (Figure 5.9 and Table 5.3) and confirmed the octahedral coordination in 5Zns-bir and 20Zns-bir. At similar Zn loadings, the fraction of ^{VI}Zn in acid birnessite was much higher than that in δ-MnO_2 (Figure 5.10). Grangeon et al found that ^{VI}Zn contents in acid birnessite from Manceau et al [2] was twice more than the contents in their Zn adsorbed δ-MnO_2 sample with similar Zn loading [109]. Kwon et al revealed based on density function theory that ^{VI}Zn was stabilized by phyllomanganate layers and water molecules at mid-plane of interlayer region [142]. Therefore acid birnessite with larger layer size and better stacked layers (see HRTEM and XRD discussions in section 2.4.2 and 2.4.4) favoured the formation of ^{VI}Zn compared to δ-MnO_2. ^{VI}Zn fraction of δ-MnO_2 with super high Zn loadings (e.g. Zn/Mn=0.5) was still smaller than acid birnessite with low Zn loadings (e.g.

Zn/Mn=0.005), suggesting that the effects of crystallinity was more significant than Zn loadings on Zn coordination environments.

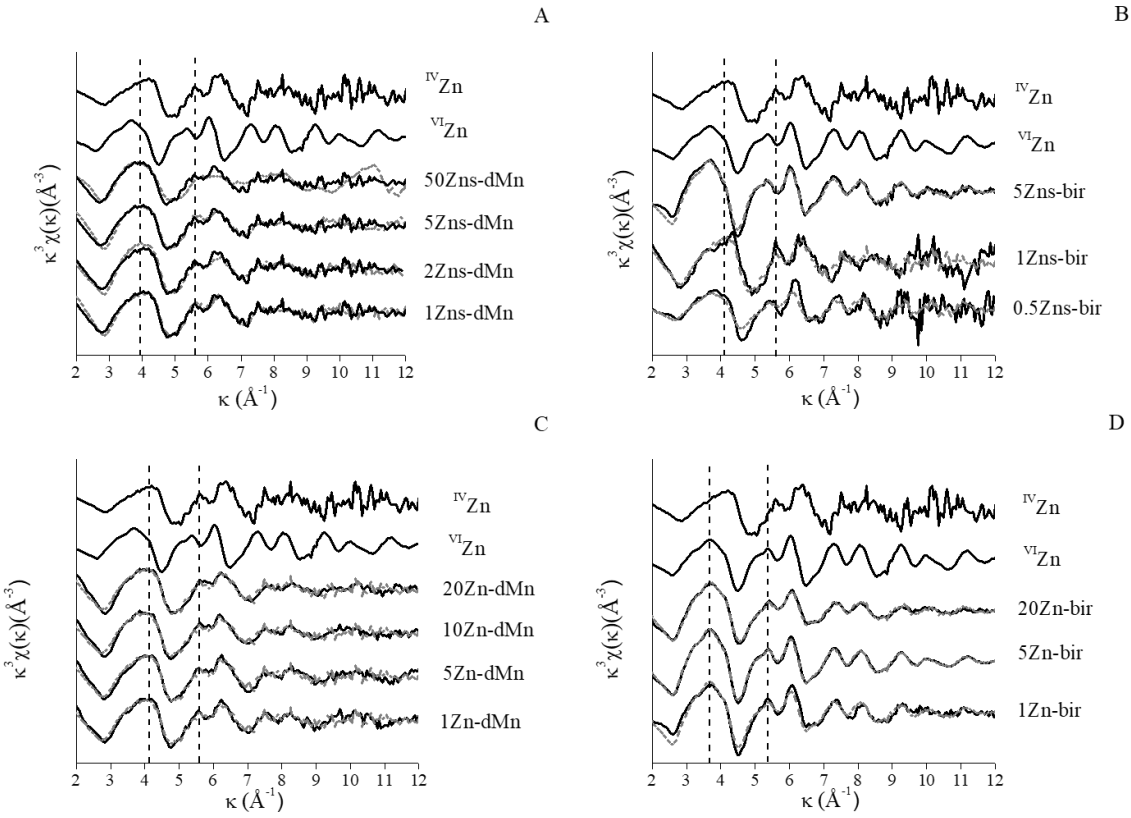

Figure 5.8 K^3-weighted Zn K-edge EXAFS of abiotic Mn oxides with different Zn treatments, including Zn adsorbed δ-MnO_2 (A) and acid birnessite (B), as well as Zn coprecipitated δ-MnO_2 (C) and acid birnessite (D). Raw and linear combination fitted data are in black solid and gray dotted lines, respectively. The vertical dash lines highlight the indicator regions.

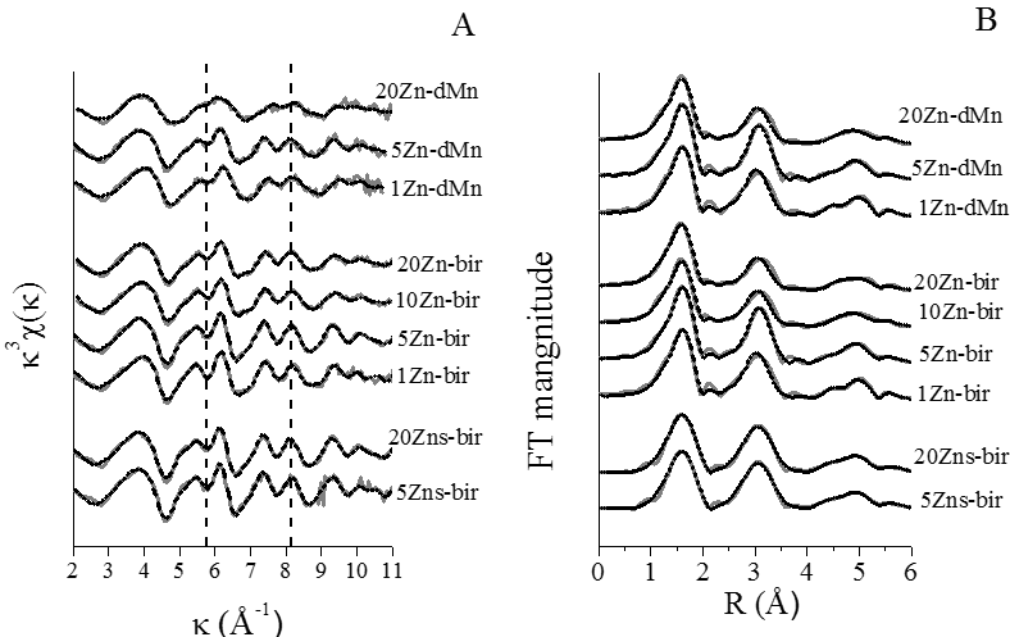

Figure 5.9 Raw and shell-by-shell fitted data of k^3-weighted Zn K-edge EXAFS and Fourier transformed spectra (not corrected for phase shift) of pure and Zn adsorbed or impacted acid birnessite and δ-MnO_2. Raw and fitted data are in gray solid and black dotted lines, respectively.

5.3.5 Zn coordination after coprecipitation with δ-MnO_2 and acid birnessite

The k^3-weighted Zn K-edge EXAFS features of Zn coprecipitated δ-MnO_2 spectra are similar to those of ^{IV}Zn reference suggesting that Zn was predominately tetrahedrally coordinated. LCF results in Table 5.2 and Figure 5.10 showed slightly increased the fraction of ^{VI}Zn with more total Zn added at low Zn/Mn ratio (0-0.1). Shell-by-shell fitting also showed increased CN (from 4.8 for 1Zn-dMn to 5.9 for 5Zn-dMn) and R (from 2.02 for 1Zn-dMn to 2.05 for 5Zn-dMn) of Zn-O bonds (Table 5.3), showing the increasing ^{VI}Zn fraction. The absolute values of ^{VI}Zn fraction in Zn coprecipitated δ-MnO_2 were similar to those in Zn adsorbed δ-MnO_2, indicating that Zn coprecipitation did not cause significant influences in Zn coordination environments in δ-MnO_2. All Zn coprecipitated acid birnessite Zn EXFAS spectra resemble the ^{VI}Zn reference showing predominant

octahedral Zn coordination in Zn coprecipitated acid birnessite. The high ^{VI}Zn contents in acid birnessite were expected considering the well crystallinity of acid birnessite samples.

Interestingly, ^{VI}Zn fraction in coprecipitated acid birnessite decreased with increasing Zn/Mn ratio, in contrary to the trends observed in other cases. 20Zn-dMn also showed a smaller CN (4.7) and R (2.01) and less ^{VI}Zn contents compared to 5Zn-dMn. The effects of Zn coprecipitation on synthetic phyllomanganate were discussed thoroughly in Chapter 2. Zn coprecipitation interrupted layer stacking of acid birnessite and δ-MnO_2. Less layers were observed in Zn coprecipitated Mn oxide HRTEM images. Zn coprecipitation also caused more layer faults/collapse and less coherence along *c** axis was revealed by XRD spectra. Disturbed layer stacking in Zn coprecipitated phyllomanganate prohibited the formation of ^{VI}Zn which required stabilization from both Mn oxide layers and mid-player interlayer water molecules [109, 142]. Layer stacking disturbance by Zn was more significant in acid birnessite than δ-MnO_2. This might explains why ^{VI}Zn decrease was observed at a wide range of Zn/Mn ratio in acid birnessite but only occurred at high Zn/Mn ratio in δ-MnO_2. Previous studies showed Zn coordination environments were not affected by pH [109, 140] although the coordination of other metals such as Ni and Cu [58] was dependent on pH. Therefore, the distinct pH conditions during synthesis (acidic for birnessite and alkaline for δ-MnO_2) should not account for the different ^{VI}Zn fraction between Zn coprecipitated acid birnessite and δ-MnO_2.

Another interesting observation was the relatively small Zn-Mn_1 CN (1.9) in 20Zn-dMn sample from shell-by-shell fitting (Table 5.3). The ideal CN for Zn-Mn_1 is 6 in theoretical cases. This value was 6 or slightly higher for all Zn coprecipitated acid birnessite. For Zn coprecipitated δ-MnO_2, this value decreased from 6.4 for 1Zn-dMn, 4.6

for 5Zn-dMn to 1.9 for 20Zn-dMn. Decreased particle size, less layer Mn(III) contents and more vacancy sites could decrease Zn-Mn_1 CN, similar to the Mn-Mn_{edge} CN discussed in section 2.4.5.2. In previous studies, Zn-Mn_1 CN also decreased with more Zn adsorbed onto edge sites (forming tetrahedral double-corner-sharing complexes, DCS) instead of interlayer sites[135]. With high Zn loading in 20Zn-dMn, the interlayer vacancy sites are probably saturated and partial Zn was adsorbed on edge sites by forming tetrahedral DCS complexes and thus ^{VI}Zn fraction was reduced.

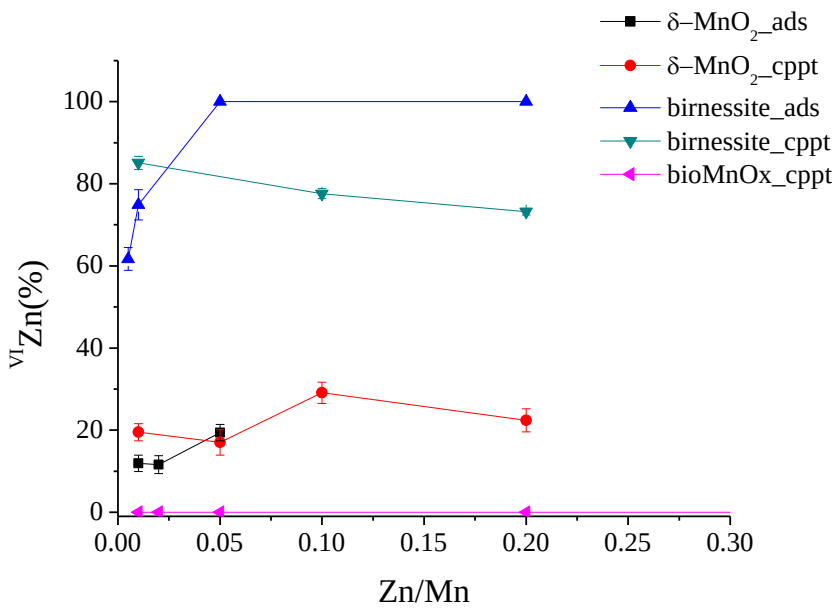

Figure 5.10 Summary of ^{VI}Zn contents when associated with Mn oxide with different treatments. "Ads" stands for adsorption while "cppt" for coprecipitation.

5.3.6 Zn coordination after coprecipitation with biogenic Mn oxides

Layers of bioMnOx gradually stacked over time [54, 84]. Therefore, bioMnOx samples with different cultivation time (24 Vs. 327 hours) were also prepared to show how Mn oxide growth would affect Zn coordination environments. Surprisingly, all Zn

coprecipitated bioMnOx EXAFS spectra are resembling ^{IV}Zn reference in spite of Zn/Mn ratio or cultivation time. LCF results showed 100% of Zn was tetrahedrally coordinated in all biogenic Mn oxide samples (Table 5.2). Based on the discussions about synthetic Mn oxides, the predominate factor that affects Zn coordination is the crystallinity of Mn oxides. The fully ^{IV}Zn observed (including the sample with Zn loading as high as 0.5) indicated that biogenic Mn oxides produced by *Roseobacter* sp. Azwk-3b in our study are very poorly crystallized and could not stabilized ^{VI}Zn species. In fact, the initial biogenic Mn oxides were mostly identified as amorphous phases with limited layer stacking [18, 25, 28, 54, 84]. With increased Zn/Mn ratio during coprecipitation with bioMnOx, layer stacking was interrupted by Zn [84] and could not stabilize ^{VI}Zn. Therefore, no sign of increased ^{VI}Zn was observed with increasing Zn/Mn ratio, even if high Zn loadings favour ^{VI}Zn formation.

Several studies showed that ^{VI}Zn fraction in lab-synthesized biogenic or natural Mn oxide samples did not agree well with the trend obtained from Zn adsorption on pre-formed Mn oxides [109, 122, 130]. Nearly ~100% ^{IV}Zn was found in a fast growing natural marine nodule (various Zn/Mn ratio at different nodule bands) [130], Zn coprecipitated bioMnOx (produced by *Paraconiothyrium sp.* WL-2, Zn/Mn=0-0.064) [84] and Zn adsorbed bioMnOx (produced by *Pseudomonas*, Zn/Mn=0.06) [139]. ^{VI}Zn existed in synthetic well crystallized Mn oxides at this Zn loading range but no ^{VI}Zn was observed in these biogenic or natural Mn oxides. The ^{VI}Zn fractions in some biogenic or natural samples with high Zn loadings were also much lower than the ^{VI}Zn fractions in well-crystallized synthetic Mn oxides with similar Zn loadings, such as Zn contaminated ferromanganese soil samples (~ 25% ^{VI}Zn, Zn/Mn ratio=0.46) [122] and Zn adsorbed bioMnOx (produced by *Pseudomonas*, ~30% ^{VI}Zn, Zn/Mn=0.37) [109, 139]. The lack of ^{VI}Zn in biogenic and natural Mn oxide samples

(which are mostly considered biogenic in origin) is probably due to the poor crystallinity of bioMnOx, as well as layer interruption by Zn coprecipitation as in the case of Zn coprecipitated acid birnessite.

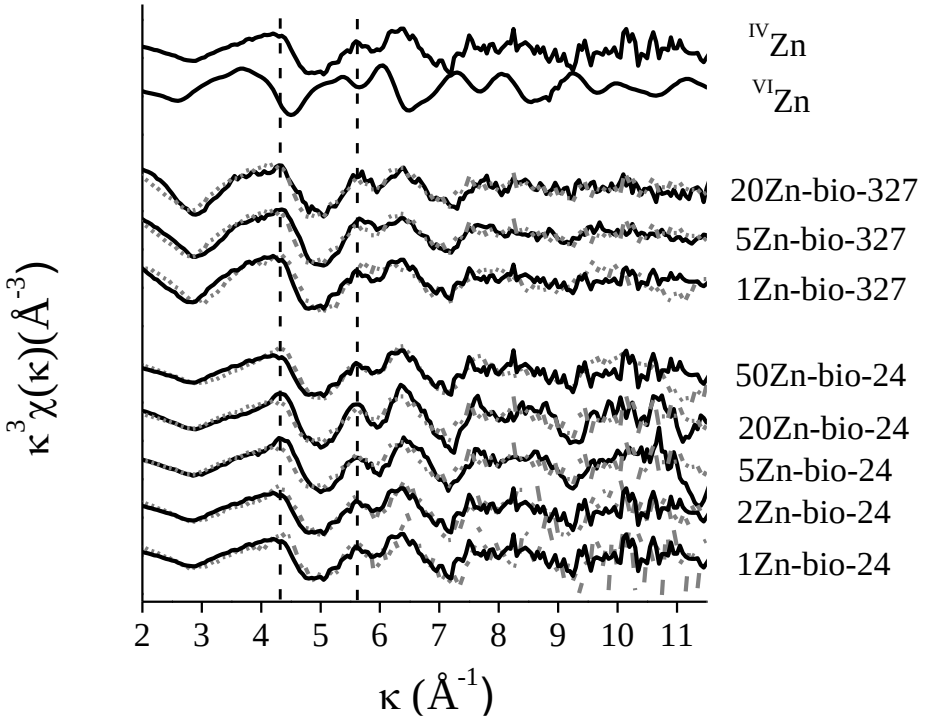

Figure 5.11 K^3-weighted Zn K-edge EXAFS of Zn coprecipitated bioMnOx. Raw and linear combination fitted data are in black solid and gray dotted lines, respectively. The vertical dash lines highlight the indicator regions.

Table 5.2 Linear combination fitting results of Zn EXAFS data using two end members chalcophanite and 0.5Zns-dMn.

Zn/Mn	^{IV}Zn (%)	^{VI}Zn (%)	Error (%)
Zn adsorbed δ-MnO₂			
0.01	88.1	11.9	2
0.02	88.4	11.6	2.2
0.05	80.6	19.4	2
0.5	72.9	27.1	3.2
Zn adsorbed acid birnessite			
0.005	38.3	61.7	2.8
0.01	25.1	74.9	3.7
0.05	0	100	0
0.20	0	100	0
Zn coprecipitated δ-MnO₂			
0.01	80.5	19.5	2.1
0.05	83.0	17.0	3.1
0.1	70.9	29.1	2.6
0.2	77.8	22.4	2.8
Zn coprecipitated acid birnessite			
0.01	14.9	85.1	1.6
0.1	22.4	77.6	1.2
0.2	26.8	73.2	0.8
Zn coprecipitated bioMnOx (24 hours)			
0.01	100	0	0
0.02	100	0	0
0.05	100	0	0
0.2	100	0	0
0.5	100	0	0
Zn coprecipitated bioMnOx (327 hours)			
0.01	100	0	0
0.05	100	0	0
0.20	98.6	1.4	4.5

Table 5.3 Zn EXAFS shell-by-shell fitting results

Samples	Residual	Shell	CN	Distance(Å)	σ^2
Reference compounds					
^{VI}Zn (chalcophanite)	11.49	Zn-O	5.5	2.07	0.009
		Zn-Mn_1	6.5	3.48	0.010
		Zn-Mn_2	12.8	5.39	0.011
^{IV}Zn (0.5Zns-dMn)	15.80	Zn-O	3.8	1.97	0.007
		Zn-Mn_1	8.8	3.35	0.013
		Zn-Mn_2	4.7	5.36	0.008
Zn-adsorbed acid birnessite samples					
5Zns-bir	8.19	Zn-O	6.0	2.081	0.011
		Zn-Mn_1	6.5	3.497	0.011
		Zn-$Mn_{1\ adj}$	1.8	4.967	0.006
		Zn-Mn_2	3.9	5.449	0.005
		Zn-$Mn_{2\ adj}$ + Zn-Mn_3	8.6	5.990	0.013*
20Zns-bir	10.76	Zn-O	5.8	2.079	0.009
		Zn-Mn_1	6.4	3.503	0.012
		Zn-$Mn_{1\ adj}$	1.4	4.982	0.010
		Zn-Mn_2	5.5	5.457	0.007
		Zn-$Mn_{2\ adj}$ + Zn-Mn_3	7.0	5.977	0.012*
Zn coprecipitated acid birnessite samples					
1Zn-bir	11.79	Zn-O	5.5	2.062	0.010
		Zn-Mn_1	10	3.483	0.014
		Zn-$Mn_{1\ adj}$	5.2	4.977	0.014
		Zn-Mn_2	5.6	5.461	0.006
		Zn-$Mn_{2\ adj}$ + Zn-Mn_3	6.1	6.028	0.013*
5Zn-bir	10.73	Zn-O	5.7	2.074	0.010
		Zn-Mn_1	6.5	3.496	0.010
		Zn-$Mn_{1\ adj}$	2.4	4.993	0.011
		Zn-Mn_2	5.9	5.453	0.008
		Zn-$Mn_{2\ adj}$ + Zn-Mn_3	7.7	5.976	0.013*
10Zn-bir	12.67	Zn-O	5.7	2.058	0.011
		Zn-Mn_1	6.8	3.486	0.014
		Zn-$Mn_{1\ adj}$	2.8	4.996	0.012
		Zn-Mn_2	7.1	5.449	0.0011
		Zn-$Mn_{2\ adj}$ + Zn-Mn_3	7.0	5.963	0.013*
20Zn-bir	13.54	Zn-O	5.9	2.021	0.009
		Zn-Mn_1	6.4	3.488	0.013
		Zn-$Mn_{1\ adj}$	1.1	4.984	0.006
		Zn-Mn_2	6.2	5.453	0.0010
		Zn-$Mn_{2\ adj}$ + Zn-Mn_3	4.9	5.965	0.013*

Zn coprecipitated δ-MnO_2 samples					
1Zn-dMn	14.78	Zn-O	4.8	2.021	0.009
		Zn-Mn_1	6.4	3.448	0.016
		Zn-Mn_2	2.0	5.405	0.004
		Zn-$Mn_{2\ adj}$ + Zn-Mn_3	6.2	5.453	0.013*
5Zn-dMn	13.22	Zn-O	5.9	2.057	0.011
		Zn-Mn_1	4.6	3.489	0.010
		Zn-Mn_2	6.6	5.452	0.010
		Zn-$Mn_{2\ adj}$ + Zn-Mn_3	5.0	5.980	0.013*
20Zn-dMn	22.44	Zn-O	4.7	2.012	0.010
		Zn-Mn_1	1.9	3.431	0.012
		Zn-Mn_2	2.8	5.378	0.014
		Zn-$Mn_{2\ adj}$ + Zn-Mn_3	6.3	6.089	0.013*

* Fixed.

5.4 Conclusions

Zn coordination was systematically studied during Zn adsorption or coprecipitation with synthetic and biogenic Mn oxides with different crystallinity. ^{VI}Zn fraction increased with higher Zn loadings during Zn adsorption on acid birnessite and δ-MnO_2. However, ^{VI}Zn fraction decreased with increased Zn loading during Zn coprecipitation with acid birnessite and high-loading Zn coprecipitation with δ-MnO_2. The decreased ^{VI}Zn fraction mainly attributes to decreased crystallinity (e.g. layer stacking interruption) caused by Zn coprecipitation. No ^{VI}Zn was observed in Zn coprecipitated bioMnOx due to the poor bioMnOx crystallinity and structural modification by Zn coprecipitation. This study helps understand Zn association with natural Mn oxides in real cases, considering the prevalent presence of Zn during natural Mn oxide growth in natural environments. These results will also deepen our understanding of the interaction mechanisms of natural Mn oxide with sequestered transition metals. The coordination environments of transition metals are related to the stability in Mn oxide structure and release rate to natural environments [211].

CHAPTER 6. CONCLUSIONS AND FUTURE STUDY

6.1 Conclusions

Mn oxides are among the most ubiquitous and reactive mineral phases in natural environments and can significantly influence the cycling of essential nutrients and a wide range of metals and organics [28, 67, 88]. The structure and reactivity of Mn oxides have been extensively studied but most of these studies used pure Mn oxide minerals, which are barely found in geological or engineering settings. More understanding is needed on the effects of metal coprecipitation on the structure and reactivity of Mn oxides, considering the prevalent interactions between metal cations and growing Mn oxide phases in the natural environments. This study systematically explored the effects of Zn coprecipitation on the structure, reactivity, and transformation of Mn oxides, as well as Zn coordination environment during its interaction with Mn oxides. Results were compared with pure Mn oxide phases and the effects of Zn adsorption on pre-formed Mn oxides, two phases commonly used in previous studies.

(1) The effects of Zn coprecipitation on the structure of synthetic Mn oxides (two biogenic Mn oxide analogs acid birnessite and δ-MnO_2), including chemical composition, surface property, layer and interlayer structure, were systematically investigated. The impacts of Zn during acid birnessite and δ-MnO_2 formation are much more significant than Zn adsorption system [109]. Zn neutralized the negative surface charge of phyllomanganates and caused great particle aggregation. The introduced Zn during acid birnessite formation expelled interlayer alkaline cations (e.g. K^+) and interrupted layer stacking along the *c* axis. The average oxidation state of δ-MnO_2 increased due to Mn(II/III) expelling by Zn, while such effects were not obvious in the acid birnessite system due

to the already high AOS and low Mn(II, III) content in acid birnessite. Zn decreased Mn(III) content within Mn oxide layers, leaving more vacancy sites (capped by Zn) for future reactions. For acid birnessite, layer stacking and interlayer cation content are significantly affected, and the modification of layer structure (e.g. crystallinity and layer Mn(III) content) is much more significant in the δ-MnO_2 system. The Zn/Mn molar ratio used in this study was 0–0.2, which is within the range observed in the natural environment (0–0.005 in marine nodules and basin soils [118-120], as high as 0.03 in coal mine drainage treatment system [121] and 0.46 in contaminated sediments [122]). The structural modifications by Zn coprecipitation was not obvious until Zn/Mn ratio reached 0.05, which indicates that the results from this study can be applied to contaminated environments. This study also provided information for the design of Mn oxides with specific composition, structure, and morphology, which is of great interest for environmental, chemical, and material science research, due to the wide application of Mn oxides as catalysts, battery materials, adsorbents, and semiconductors.

(2) The effects of Zn coprecipitation on the sorptive reactivity of Mn oxides were investigated towards both representative cation (Cd) and anions (arsenate and phosphate). Pre-loaded Zn, either coprecipitated or adsorbed, inhibited Cd adsorption on δ-MnO_2, due to the competition between Zn and Cd. Total metal uptake (Zn+Cd) was enhanced as a result from the above-mentioned structural changes. The charge-compensated Zn-δ-MnO_2 surface showed significantly enhanced sorptive capacity toward phosphate and arsenate. Higher sorption capacity, higher affinity, faster kinetics, and a right-shifted adsorption edge were observed for phosphate and arsenate sorption on Zn-coprecipitated δ-MnO_2, compared to pure δ-MnO_2. Compared to Zn-sorbed δ-MnO_2

samples, Zn-coprecipitation was more effective in enhancing anion sorption. No significant ternary surface complex and/or precipitation were detected for phosphate and arsenate sorption on Zn treated δ-MnO_2. This study quantified the sorptive reactivity of Mn oxides under complex conditions that are close to realistic environments and revealed the underlying mechanisms. Our study suggests that the roles of Mn oxides in regulating anion fate and transport should be re-visited by considering the impacts (e.g. structural modification, surface charge compensation) of the presence of different metals during (i.e. coprecipitation) or after Mn oxide formation (i.e. sorption).

(3) With the structural modifications, Zn coprecipitation can potentially affect the Mn cycling by influencing the phyllomanganate reductive aging/transformation process. The kinetics and pathways of Mn^{2+} induced reductive transformation were examined in oxic or anoxic conditions to investigate the long-term stability of Zn coprecipitated Mn oxides. During the interaction with Mn^{2+}, compared to the pure birnessite system, a new Zn-containing mineral phase (hetaerolite) was formed in the Zn-coprecipitation system, modifying the transformation pathway and increasing Mn^{2+} removal and Mn(IV) consumption. The transformation from Zn coprecipitated birnessite to Mn(III)-containing feitknechtite was faster compared to pure phases, due to the smaller particle caused by Zn coprecipitation. Further transformation to a more stable phase manganite with tunneled structure was slowed down in the presence of Zn, probably due to the decreased Mn^{2+} concentration and lack of the buckling cation K^+. Accelerated feitknechitite precipitation suggested enhanced redox and catalytic reactivity of Zn coprecipitated birnessite. Such information can help better understand the roles of Mn oxides in the fate and transport of a range of elements, as well as the Mn cycle itself. Since

Mn oxides are also widely used as oxidants and catalysts, the modified redox and catalytic property of metal-coprecipitated Mn oxides can provide information on the design and selection of targeting phases for environmental remediation and catalytic applications.

(4) Several studies showed that Zn coordination environment in lab-synthesized biogenic or natural Mn oxide samples did not agree well with the trend obtained from Zn adsorption on pre-formed synthetic Mn oxides [109, 122, 130]. Zn coordination was systematically studied during Zn adsorption or coprecipitation with synthetic and biogenic Mn oxides with different crystallinity, in order to explore the various factors that might affect Zn coordination environment, such as Zn loadings, Zn presence during/post Mn oxide formation (i.e. coprecipitation vs. adsorption), crystallinity, and involvement of microbes. The fraction of Zn octahedral complex (^{VI}Zn) increased with increasing Zn loading during Zn adsorption on acid birnessite and δ-MnO_2. However, ^{VI}Zn fraction decreased with increased Zn loading during Zn coprecipitation with acid birnessite and high-loading Zn coprecipitation with δ-MnO_2. The decreased ^{VI}Zn fraction was mainly attributed to decreased crystallinity (e.g. interruption of layer stacking) caused by Zn coprecipitation. No ^{VI}Zn was observed in Zn coprecipitated biogenic Mn oxides due to the poor structure crystallinity. Results elucidated how the structural modifications caused by Zn coprecipitation would affect Zn coordination in Mn oxides and explained the phenomenon that why the fraction of octahedrally coordinated Zn was generally low in natural or biogenic Mn oxides. This study can help understanding Zn association with natural Mn oxides, considering the common association of Zn with natural Mn oxides.

6.2 Future recommendations

(1) The effects of Zn coprecipitation on structure, sorptive reactivity, and transformation were systematically explored in this study. Cd uptake was systematically studied and Zn coprecipitated Mn oxides might have very different sorptive reactivity towards other metal cations (e.g. Ca,Mg) and trace metals with different water exchange rate (e.g. Ni) and adsorption mechanisms (e.g. Pb). For anion sorption, no significant amount of precipitation or ternary complex(es) were observed, but their potential existence can not be ruled out given the detection limits of employed techniques.

(2) During cation adsorption and transformation experiments, both HEPES and MES buffers were used to stabilize pH in the systems. Recent studies have shown that these organic buffers can react with Mn oxides and cause Mn oxide particle dissolution, increased Mn(II/III) contents, and modified layer stacking [192, 212]. Control experiments should be conducted to study how buffers could affect the sorption and transformation experiments by equilibrating buffers with pure or Zn coprecipitated Mn oxides. Although the oxidative and catalytic properties of Zn coprecipitated Mn oxides were investigated during birnessite reaction with Mn^{2+}, more systematic studies are required to explore the effects of Zn coprecipitation on the redox properties of Mn oxides. Electrochemical techniques could be used to measure the redox potential of pure and Zn coprecipitated Mn oxides. Redox probes such as As(III) and Cr(III) can be used to study the redox kinetics and capacity. With altered average oxidation state, particle size, and availability of Mn(III), the interaction between Zn-coprecipitated Mn oxides and redox-activie species can be significantly influenced.

(3) The effects of Zn coprecipitation were different for acid birnessite and δ-MnO_2, probably due to their distinct crystallinity and synthesis conditions. Mn^{2+} oxidation

was magnitudes faster when catalyzed by microbes, and natural Mn oxides are generally considered to be biogenic in origin [18]. Although acid birnessite and δ-MnO_2 have served as analogs of biogenic phyllomanagantes, their actual formation conditions and crystallinity can be very different from both synthetic phases. In Chapter 5, Zn coprecipitation showed some effects on the biogenic Mn oxide production rate and layer Mn(III) and vacancy contents. More research is required to systematically study the effects of Zn coprecipitation on the structure and properties of biogenic Mn oxides produced by bacteria or fungi through different mechanisms (e.g. enzymatic oxidation or reactive oxygen species oxidation). Similar sorption and transformation experiments can be conducted on Zn coprecipitated biogenic Mn oxides and the results can be compared with those from synthetic Mn oxides.

(4) Zn is the least compatible with Mn oxide structure among all heavy metals commonly associated with Mn oxides [2, 74, 78, 117], and is shown by this study to cause great structure modifications during Zn coprecipitation. The effects of other metals on Mn oxide structure have also been studied and extent of structure interruption increased in the order of Co < Ni < Fe [14, 80, 116]. Most of these studies focused on the structure characterization of metal-impacted Mn oxides in the field of material science. The implications of these structural modifications in biogeochemistry are required by relating the metal-impacted structure with the interactions between Mn oxides and other species. In this case, sorption, redox, and transformation experiments can be conducted on Mn oxides under the influence of various metal cations (e.g. Co, Ni, Cu, Fe, Zn). With different structural influence by metals, the further interaction with other species will probably be metal specific. Metal interaction with growing Mn oxides in real environmental systems are even more

complicated and the effects of multiple metal coprecipitation should also be considered. The contribution of each metal might be different considering the distinct atomic radii, charges, CFSE and thus compability with Mn oxide structure.

APPENDIX A. SUPPLEMENTARY MATERIALS FOR CHAPTER 2

A.1 BET surface area analysis

Surface areas of the synthesized Mn oxides were measured on a TriStar 3000 BET Surface Area Analyzer using a 5-point BET method. Ultra-high-pressure nitrogen was applied as the adsorbate and liquid nitrogen as the cryogen. Before the measurement, Mn oxides were purged with a dry He atmosphere at room temperature for 16 hours to remove as much water as possible.

A.2 Zeta potential analysis

10 mg of each Mn oxide sample was suspended in 40 mL DI water and allowed to equilibrate and settle for 24 hours. 0.75 mL of the suspension was mixed with 4 mL of 10 mM NaCl solution and adjusted to different pH values. Zeta potential of the suspension was measured on a Marlvern nano zetasizer (Marlvern Instruments, Ltd).

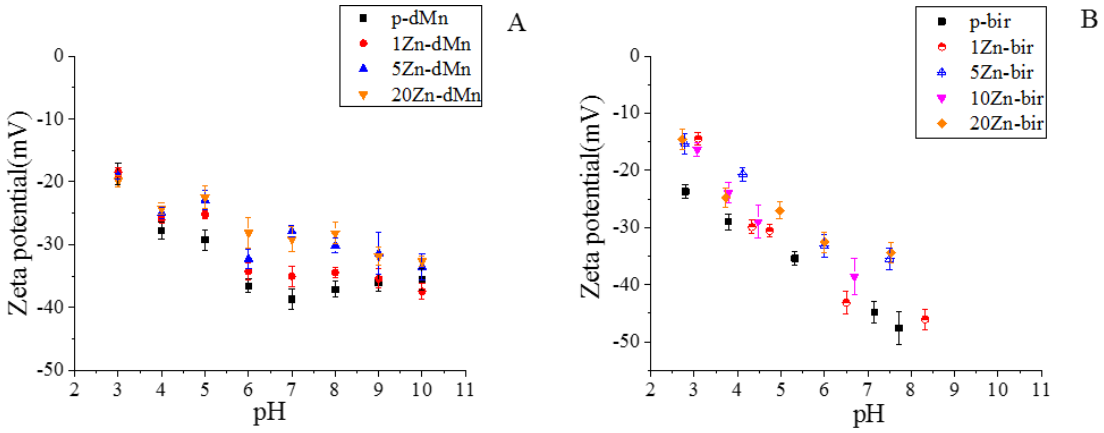

Figure A.1 Zeta potential of pure and Zn-coprecipitated (A) δ-MnO_2 and (B) acid birnessite samples.

A.3 High resolution transmission electron microscopy (HRTEM)

High-resolution transmission electron microscopy (HRTEM) analysis of the synthesized Mn oxide samples were conducted on a JEOL 2010F TEM. A small amount of each sample was dispersed in ethanol and ultrasonicated for ~1 min. Then a drop of the suspension was placed onto a 200-mesh Cu grid with a holey-carbon support film and air dried. To avoid beam damage, image focus was obtained on the carbon film adjacent to the particles of interest, then the beam was moved onto the sample particle.

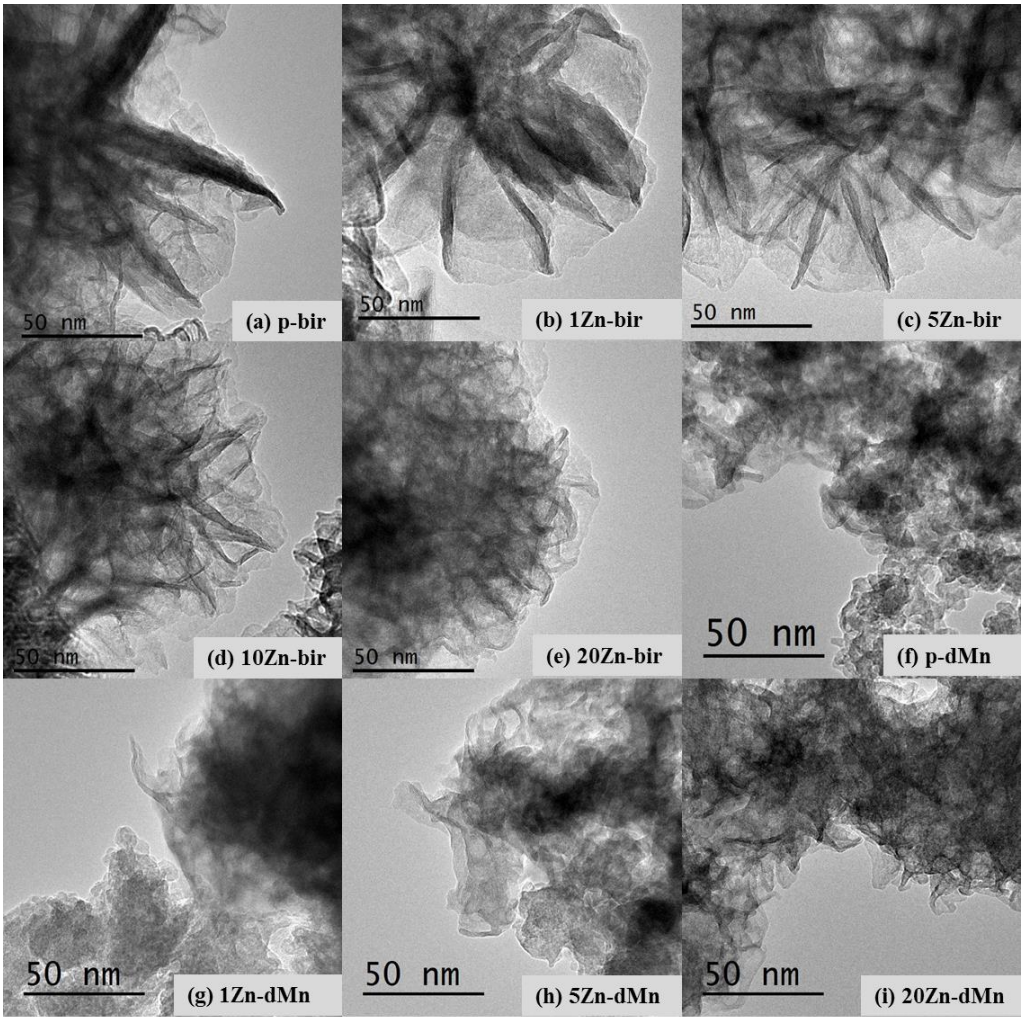

Figure A.2 HRTEM images of pure and Zn-coprecipitated δ-MnO_2 and birnessite.

Table A.1 Number of stacking layers of acid birnessite as determined by HRTEM.

Sample	p-bir	1Zn-bir	5Zn-bir	10Zn-bir	20Zn-bir
Number of stacking layers at different locations	15	10	10/6/5	8/4/8	5/6
	12	12	5	7/8	5
	10	8	5/9/9	6	4
	9	9	8	5/10	4
	8/10	19/12	15/8	7	4/6
	5	13	7	5	5
	10	8	17/10	6	5/5
	5	8	14/11/11	5	5
	7	10	13	5	
	13		8/10/8	3/4	
	9		4/9	11	
	12		4	6	
	11		7	8	
	12		6	6	
	19/14		13/19/8	7	
	10		6/5	10	
	8/10			7	
	11			5	
	9/14			7	
Average	10.6 ± 3.2	10.9 ± 3.4	9.0 ± 3.8	6.6 ± 2.0	4.9 ± 0.7

A.4 X-ray diffraction analysis

X-ray diffraction (XRD) analysis of the acid birnessite samples were conducted on a D8 Advanced X-ray diffractometer (Bruker AXS, Germany) using Mo radiation ($\lambda_{\alpha 1}$ = 0.709 Å). XRD data of the δ-MnO_2 samples were collected at beamline 14A (λ = 7.792947 Å) of National Synchrotron Light Source (NSLS) at Brookhaven National Laboratory (Upton, NY).

A.5 Zn XAS data collection and analysis

Zn K-edge EXAFS analysis was conducted to elucidate Zn coordination environments in the Zn-coprecipitated Mn oxide samples. Zn XAS data collection followed

the same procedure as Mn XAS data collection, and used Zn foil for energy calibration. k^3-weighted Zn K-edge EXAFS and Fourier transformed spectra of Zn-coprecipitated oxide samples were plotted in Figure A.3. Shell-by-shell EXAFS fittings were also conducted and the results are listed in Table A.2. Previous studies have shown that during adsorption to Mn oxides, Zn formed tetrahedrally coordinated complexes (Zn^{IV}) at low Zn loading and octahedrally coordinated complexes (Zn^{VI}) at high Zn loading, and the differences in the coordination environments is also affected by Mn oxide crystallinity [2, 139, 140]. Interestingly, for the Zn-coprecipitated samples in this study, despite of the large Zn concentration range (1–20%), all the Zn-birnessite samples contained only Zn^{VI}, whereas all the Zn-δ-MnO_2 samples only contained Zn^{IV}, all as surface sorbed species at the vacancy sites. Previous studies have shown that Zn presence during biogenic Mn oxide formation only resulted in Zn^{IV} surface complexes regardless of Zn loading [84].

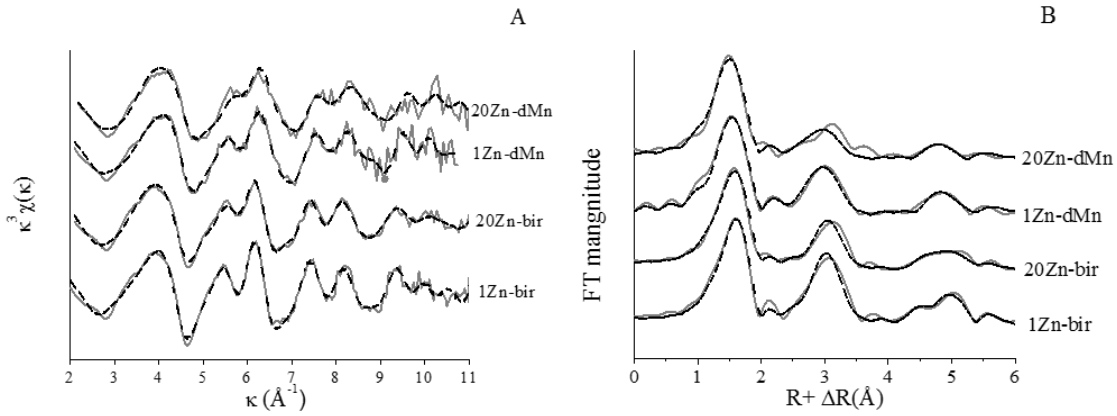

Figure A.3 Zn K-edge EXAFS of pure or Zn-coprecipitated acid birnessite and δ-MnO_2 phases. Raw and fitted data are in gray solid line and black dotted line, respectively.

Table A.2 Zn EXAFS shell-by-shell fitting results for Zn-coprecipitated acid birnessite and δ-MnO_2.

Samples	Residual	Shell	CN	Distance(Å)	σ^2
acid birnessite					
1%Zn	13.1	Zn-O	6.0	2.06	0.011
		Zn-Mn_1	6.8	3.47	0.010
		Zn-Mn_2	12.9	5.45	0.013
20%Zn	13.5	Zn-O	6.0	2.05	0.012
		Zn-Mn_1	5.1	3.48	0.012
		Zn-Mn_2	12.9	5.45	0.015
δ-MnO_2					
1%Zn	10.3	Zn-O	4.3	2.02	0.009
		Zn-Mn_1	6.9	3.48	0.016
		Zn-Mn_2	9.3	5.48	0.018
20%Zn	7.2	Zn-O	4.3	2.02	0.010
		Zn-Mn_1	3.4	3.44	0.014
		Zn-Mn_2	4.7	5.42	0.015

A.6 Pair distribution function analysis

Synchrotron high-energy X-ray total scattering data of the synthesized Mn oxides samples were collected at beamline 11-ID-B (~58.6 keV, λ = 0.2117 Å) of the Advanced Photon Source (APS), Argonne National Laboratory, IL. Conversion of data from 2D to 1D was performed using the program Fit2D [162, 213]. The experimental total scattering structure function *S(Q)*, reduced experimental structure function *f(Q)*, and pair distribution function (PDF), or *G(r)*, were obtained using PDFgetX2 [214]. The PDFs were calculated from the Fourier transforms of these data truncated at 26 $Å^{-1}$.

The PDF, G(r), for all the Zn-coprecipitated birnessite and δ-MnO_2 samples are shown in Figure A.4. Compared to δ-MnO_2, acid birnessite has sharper peaks extending to longer R range, indicating better crystallinity and consistent with TEM and XRD results. The attenuation of G(r) intensity can be used to estimate the size of coherent scattering domain (CSD) [81, 141, 215]. Estimated CSD size is ~30 Å for δ-MnO_2 and ~50 Å for acid brinessite. Zn presence did not change the CSD size for both birnessite and δ-MnO_2 systems.

Figure A.4 (B, D) shows the G(r) in 1–5 Å range. A well-established PDF structural model for Mn oxides was developed by Zhu et. al [141] to describe the atomic pair contributions for the peaks in G(r). Peak positions for all the pure and Zn-coprecipitated birnessite and δ-MnO_2 samples within 5 Å are consistent with those of pure hexagonal birnessite [141]. According to this model, the first peak at ~1.9 Å is attributed to Mn-O atomic pairs within the MnO_6 layers. For the birnessite system, no obvious changes were observed for this peak (Figure A.4 A). Based on Zn EXAFS analysis (Figure A.3, Table A.2), Zn exists as inner-sphere octahedrally coordinated surface complexes below/above vacancy sites for all Zn-coprecipitated birnessite samples, with the first shell Zn^{VI}-O distance of 2.02–2.06 Å. This contributes to the slight increase on the left shoulder of the small peak at ~2.3 Å (Figure A.4A). For the δ-MnO_2 system, the peak at ~1.9 Å decreased in intensity without significant change in peak width and slightly shifted to higher distance with increasing Zn content (Figure 2C). Similar to the birnessite system, there are three potential factors that will affect the intensity, width, and position of this peak. (1) Layer Mn(III): because $Mn(III)_{layer}$-O has slightly longer distance than $Mn(IV)_{layer}$-O in the layer, the presence of more layer Mn(III) will slightly broaden this peak and shift it to higher

distance without significant modification in peak intensity (i.e. Zn 0.88 Å, Mn(III) 0.72 or 0.785 Å and Mn(IV) 0.67 Å) [155]. Our Mn EXAFS analysis suggested the gradual decrease of layer Mn(III) with increasing Zn content (Figure 2.4, Table 2.2), which alone would narrow the peak width and shift it to lower distance without significant change in peak intensity. (2) Change of particle size: Smaller particle size will decrease the overall intensity of all peaks [138]. Since the CSD is not significantly affected in the δ-MnO_2 system, this factor likely had minimal impact. (3) Zn complexation on the oxide surfaces: Similar to the birnessite case, Zn EXAFS analysis indicated that Zn exists as inner-sphere surface complexes (Figure A.3, Table A.2) with the first shell Zn-O distance of ~1.98–2.01 Å (Zn^{IV}). The contribution of ~4 Zn-O atomic pairs at this distance alone will both broaden the peak, shift it to slightly higher distance, and lower the peak intensity (i.e. Zn in tetrahedral coordination vs Mn in octahedral coordination). The overall changes in peak shape and intensity are the combined effects of above mentioned factors.

The peak at ~2.85 Å corresponds to $(Mn\text{-}Mn)_{layer}$ and $(O\text{-}O)_{layer}$ pairs between two edge-sharing octahedra [141]. With increasing Zn content, both birnessite and δ-MnO_2 showed decreased peak intensities and the decrease was more significant for the δ-MnO_2 system (Figure A.4A and C). Increase of layer vacancy sites (i.e. less layer Mn) and/or reduced particle size can both cause such change. As discussed previously, the PDF CSD size for both the birnessite and δ-MnO_2 systems are not affected by Zn addition. Furthermore, Zn-Mn distance (due to Zn sorption) is at higher distance (above ~3.4 Å) for both the birnessite and δ-MnO_2 systems, therefore does not affect this peak. Therefore the change to this peak is more likely due to the increase of layer vacancy sites, consistent with Mn EXAFS fitting results. Similar effects were also observed when Ni was added during

the formation of biogenic Mn oxides [58]. Zn sorption to δ-MnO_2 was also previously shown to expel layer Mn(III) and create more vacancy sites [109].

The peak at ~3.5 Å can be attributed to several atomic pairs: $(Mn\text{-}O)_{layer}$, Mn_{layer}-Mn_{inter}, Mn_{inter}-O_{layer} [141], as well as Zn-Mn_1 due to Zn sorption. For Zn-birnessite system, this peak intensity increased with increasing Zn content with no obvious changes in peak width and position. For Zn-δMnO_2 system, no obvious changes were observed for this peak. Due to the complexity of the contributing atomic pairs, these changes were not further analyzed.

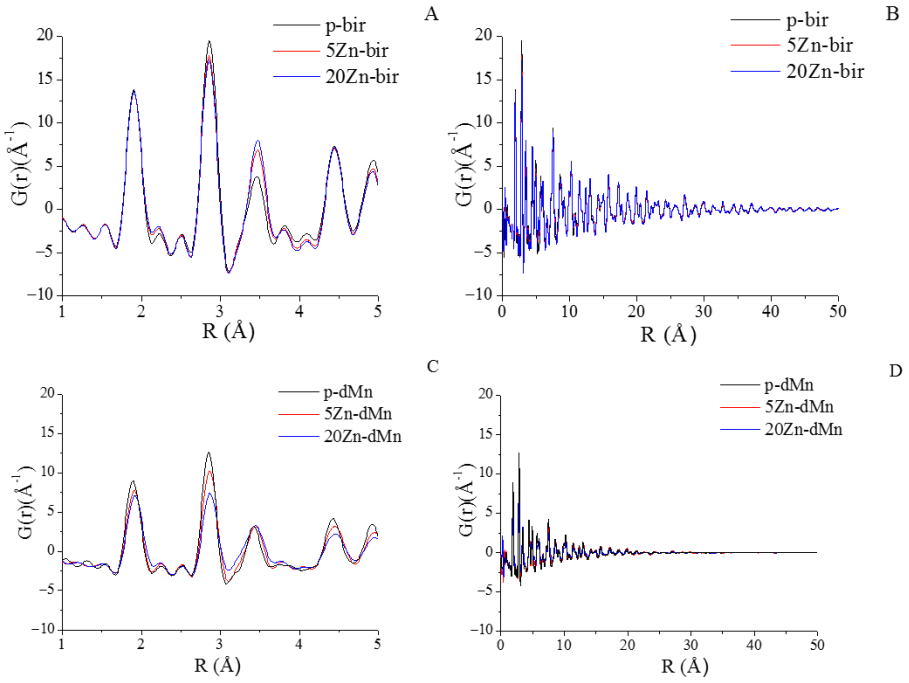

Figure A.4 PDF of pure and Zn-coprecipitated Mn oxides plotted at 5 (left) and 50 Å scales (right). (A, B) acid birnessite, (C, D) δ-MnO_2.

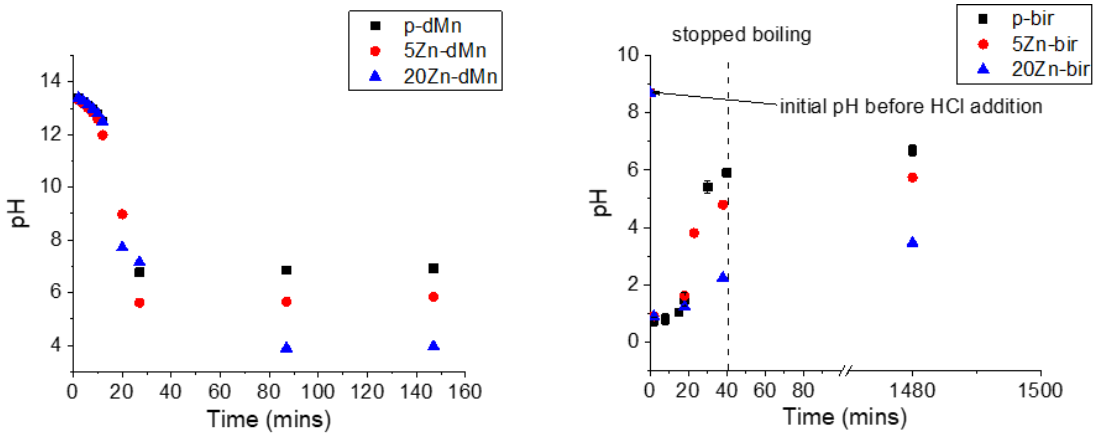

Figure A.5 Change of solution pH during the synthesis of (A) δ-MnO_2 and (B) acid birnessite in the presence of Zn.

APPENDIX B. SUPPLEMENTARY MATERIALS FOR CHAPTER 3

B.1 Solid phase analysis of sorption products

XRD and XAS analysis of adsorption experiment products were conducted to investigate the anion adsorption mechanisms on Zn-treated (adsorbed or coprecipitated) Mn oxides (e.g. precipitation and/or ternary complexes). The suspension after adsorption experiments were filtered using 0.22 μm membrane. The solids were rinsed with deionized (DI) water and freezer dried before XRD experiments using a Panalytical Empyrean multipurpose diffractometer with Cu Kα radiation. For As EXAFS analysis, filtered wet paste were mounted on an acrylic sample holder and sealed with Kapton tape. Samples were stored at -20 °C before experiments. As EXAFS experiments were conducted at Beamlines 5-BM-D and 12-BM-B at Advanced Photon Source (APS; Argonne National Laboratory, Lemont, IL) using Si(111) monochromator detuned by 40% for harmonic rejection. As EXAFS data were collected in fluorescence mode using a Lytle detector (12-BM-B at APS) or a vortex detector (Beamline 5-BM-D at APS). Scanning were done at room temperature. 2~6 scans were conducted and averaged to increase signal/noise. XAS data analysis was performed using the programs SIXPACK [143], Ifeffit [144], and WINXAS [145]. Shell-by-shell fitting of As EXAFS spectra to investigate the coordination environments of adsorbed As.

B.2 Zn and Cd adsorption on pure δ-MnO_2

Zn and Cd adsorption isotherms on pure δ-MnO_2 at pH 6 are shown in Figure B.1. With increasing initial metal concentrations, both show gradual increase in metal uptake. δ-MnO_2 has a higher adsorption capacity towards Zn (C_{max} = 2.01 mmol/g) than Cd (C_{max}

= 1.49 mmol/g). Similarly, higher Zn sorption capacity compared to Cd was also observed during interaction with acid birnessite [151], cryptomelane [216], hausmannite [216], and hydrous Mn and Fe oxides [68, 217]. The affinity of Zn is also higher than Cd towards δ-MnO_2, as indicated by their adsorption equilibrium constant K values (4.70 for Zn and 3.77 for Cd). The adsorption affinity of metal cations towards oxides follows the reverse order of hydrated cation radii[68]. Several studies also revealed the correlation between K value and the first hydrolysis constant of the metal [69-71]. Zn has a smaller ionic radii and acts as a harder Lewis acid than Cd [72]. As a result, Zn has a higher adsorption affinity towards δ-MnO_2 than Cd under the same conditions in this study.

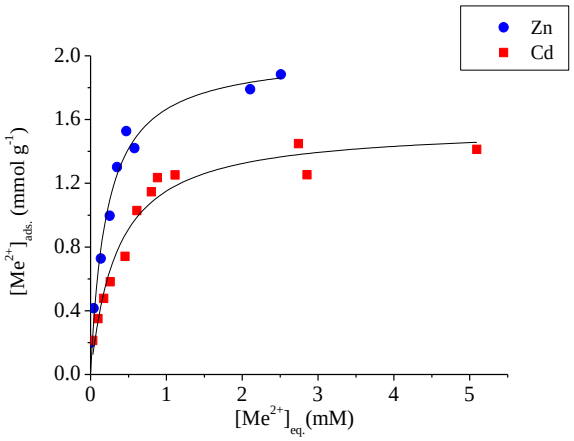

Figure B.1 Cd and Zn adsorption isotherms on pure δ-MnO_2. Solid lines are Langmuir model fitting results.

B.3 Cd and arsenate sorption and normalization by surface area

Specific surface area (SSA) of pure and Zn co-precipitated δ-MnO_2 was measured using a multi-point nitrogen gas (N_2) adsorption BET method. SSA decreased with increasing Zn content during δ-MnO_2 synthesis (221.9 m^2/g for pure, 123.9 for coppt0.05, and 131.6 for coppt0.20 δ-MnO_2[174], mainly due to the great aggregation caused by Zn coprecipitation. Cd and arsenate sorption was normalized by surface area and plotted in Figure B.2. Cd sorption capacity increased from pure to 0.05coppt samples, and then decreased from 0.05coppt to 0.2coppt samples. After normalization by surface area, vacancy site density would be the main reason affecting Cd adsorption on δ-MnO_2. On one hand, Zn-coprecipitation could reduce layer Mn(III) contents and increase vacancy site density. On the other hand, these vacancy sites which was freed from Mn(III) occupation was covered by Zn, preventing further Cd sorption on δ-MnO_2 surface[174]. These two competing factor might be the reason for the first increasing then decreasing trend in Cd adsorption on Zn co-precipitated δ-MnO_2. Arsenate sorption was still enhanced by Zn co-precipitation, even more significant than arsenate adsorption normalized by mass.

However, additional attention is required when normalizing adsorption amount by BET-measured surface area. Direct observations such as XRD and HRTEM show a smaller crystallite size of Zn adsorbed [109] and coprecipitated [84, 174]δ-MnO_2, but BET surface area decreased with increasing Zn content during coprecipitation. Crystallite-scale estimation and experimental BET methods can give very different results when estimating Mn oxide particle size. In previous studies, theoretical calculations were conducted to estimate surface area using crystallite data and MnO_2 formula weight. The results (for example, 746 $m^2\ g^{-1}$ for Na-birnessite [218]) were typically much higher than experimentally determined

values using BET method [24, 57, 63, 219]. Tonkin et al pointed out that BET method might underestimate mineral surface area due to surface modification (e.g. decomposition) during drying in BET method [218]. In this study, Zn co-precipitation decreased the crystallinity of δ-MnO_2 and decreased crystallinity could cause great aggregation [14], which can lead to the decreased BET surface area. δ-MnO_2 particles were sonicated and well dispersed in solutions before adsorption experiments. In addition, both Cd[78] and arsenate[182] can adsorb at interlayer sites, especially Cd. These sites are not accessible by N_2 during N_2-sorption based BET measurement. Therefore, BET measured surface area should be interpreted with caution during metal adsorption on δ-MnO_2.

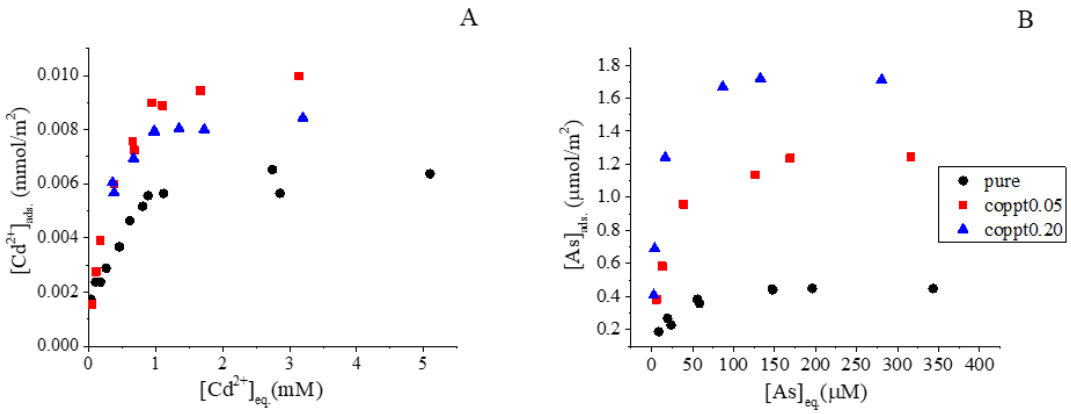

Figure B.2 Cd (A) and arsenate (B) adsorption isotherms on pure and Zn coprecipitated δ-MnO_2. Results were normalized by surface area.

Table B.1 Fitting parameters for phosphate and arsenate sorption isotherms.

Phosphate sorption

Sample	Freundlich			Langmuir		
	K_F	1/n	R^2	K_L	Q_m	R^2
pure	14.8929	0.2367	0.8132	0.0279	81.3143	0.9506
coppt0.05	10.2647	0.4207	0.9391	0.0398	120.4623	0.9565
coppt0.20	61.9954	0.2432	0.9187	0.2542	186.2230	0.9850

Arsenate sorption

Sample	Freundlich			Langmuir		
	K_F	1/n	R^2	K_L	Q_m	R^2
pure	25.3362	0.2702	0.9215	0.0534	109.4505	0.9389
coppt0.05	41.3517	0.2441	0.8853	0.0666	162.1949	0.9930
coppt0.20	67.4671	0.2222	0.8853	0.1443	218.0005	0.9803

Note: K_F represents reaction rate constant of Freundlich isotherm model. n is a parameter relevant to the reaction strength between adsorbed molecules and adsorbent surface. R^2 represents relevant coefficient. K_L represents reaction rate constant of Langmuir isotherm model. Q_m denotes monolayer adsorption capacity.

Table B.2 Fitting parameters for phosphate and arsenate sorption kinetic models.

Phosphate sorption

Sample	Pseudo first-order			Pseudo second-order			Particle diffusion		
	k_1	Q_e	R^2	k_2	Q_e	R^2	k_{id}	C	R^2
pure	0.4217	43.4857	0.9176	0.0128	45.5189	0.9399	3.7861	22.5249	0.8393
coppt0.05	0.6221	65.9621	0.9697	0.0211	67.6473	0.9756	5.0069	36.4563	0.6197
coppt0.20	0.6936	128.688	0.9643	0.0093	132.360	0.9804	9.3262	77.8550	0.6881

Arsenate sorption

Sample	Pseudo first-order			Pseudo second-order			Particle diffusion		
	k_1	Q_e	R^2	k_2	Q_e	R^2	k_{id}	C	R^2
Pure	0.6534	76.7312	0.9824	-	68.2046	0.4257	4.7035	50.6807	0.6806
coppt0.05	0.7433	98.7929	0.9495	-	88.5177	0.6356	6.8173	61.8303	0.6609
coppt0.20	0.5985	137.8668	0.9615	-	119.5760	0.4442	10.236	81.6503	0.7328

Note: k_1 represents reaction rate constant of pseudo first-order adsorption kinetic model. Q_e represents the P adsorbed amount at adsorption equilibrium. R^2 represents relevant coefficient. k_2 represents reaction rate constant of pseudo second-order adsorption kinetic model. K_{id} represents reaction rate constant of piratical diffusion adsorption kinetic model. C is a constant related to boundary layer thickness.

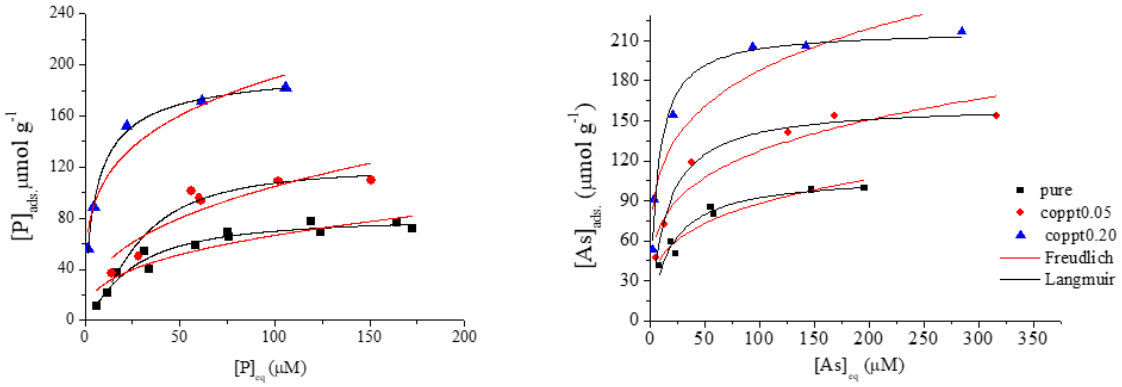

Figure B.3 Phosphate and arsenate adsorption isotherms and comparison between Freudlich and Langmuir model fitting results. Black lines are the fitting results of Langmiur model and red for Freudlich model.

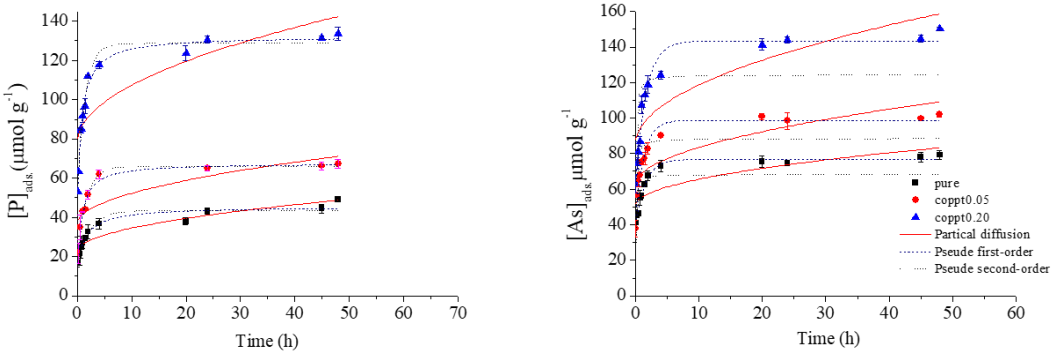

Figure B.4 Phosphate and arsenate adsorption kinetics and comparison of three model fitting results.

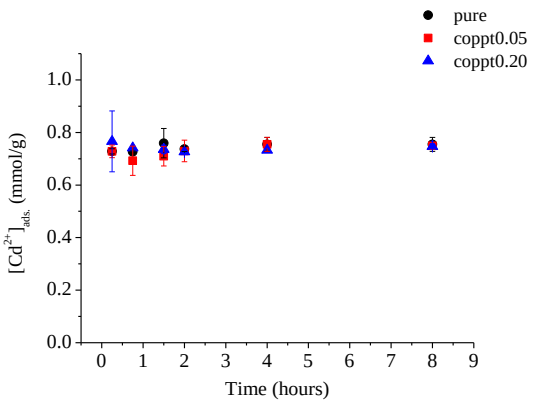

Figure B.5 Cd adsorption kinetics on pure and Zn coprecipitated δ-MnO_2. Reaction conditions are: 0.5 g L^{-1} δ-MnO_2, 1 mM Cd in solutions, 0.1 mM NaCl, pH = 6 (20 mM MES buffer).

APPENDIX C. SUPPLYMENTARY MATERIALS FOR CHAPTER 4

C.1 Identification of mineral phases in transformation products

XRD data of reference compounds (feitknechtite, manganite, pure and Zn substituted hausmannite and hetaerolite) are shown in Figure C.1. Data for transformation products of both pure and Zn coprecipitated birnessite after 18-day reaction were also shown. The transformed solids were identified as a mixture of feitknechitite, manganite, and/or hetaerolite, as marked with asterisks with different colors.

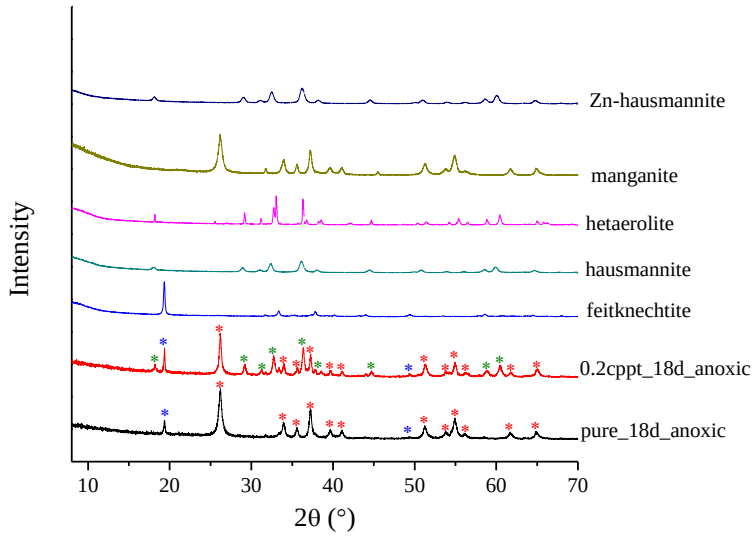

Figure C.1 XRD data of reference compounds, and acid birnessite with or without Zn after 18-day anoxic transformation in the presence of Mn^{2+}. Asterisks with different colors indicate the peaks for hetaerolite (green), feitknechtite (blue), and manganite (red).

Mn EXAFS data of pure and Zn coprecipitated transformation products under both anoxic and oxic conditions were also collected and the k^3-weighted Mn K-edge EXAFS were plotted in Figure C.2. Reference compounds (birnessite, feitknechtite [111], manganite [111] and hetaerolite) were also plotted. The peak evolvement in Mn EXAFS showed the

same transformation trend as revealed by XRD and FT-IR. Linear combination fitting (LCF) was conducted using the reference compounds to obtain the relative proportion of each phase. The fitting of Zn birnessite transformation products did not give reasonable results. It is possible that the hetaerolite phase precipitated in this system is actually a solid solution between hetaerolite and hausmannite with a spinel structure ($Zn(II)_xMn_{1-x}Mn(III)_2O_4$) [111], therefore using hetaerolite as a reference compound in LCF can lead to fitting results with large errors.

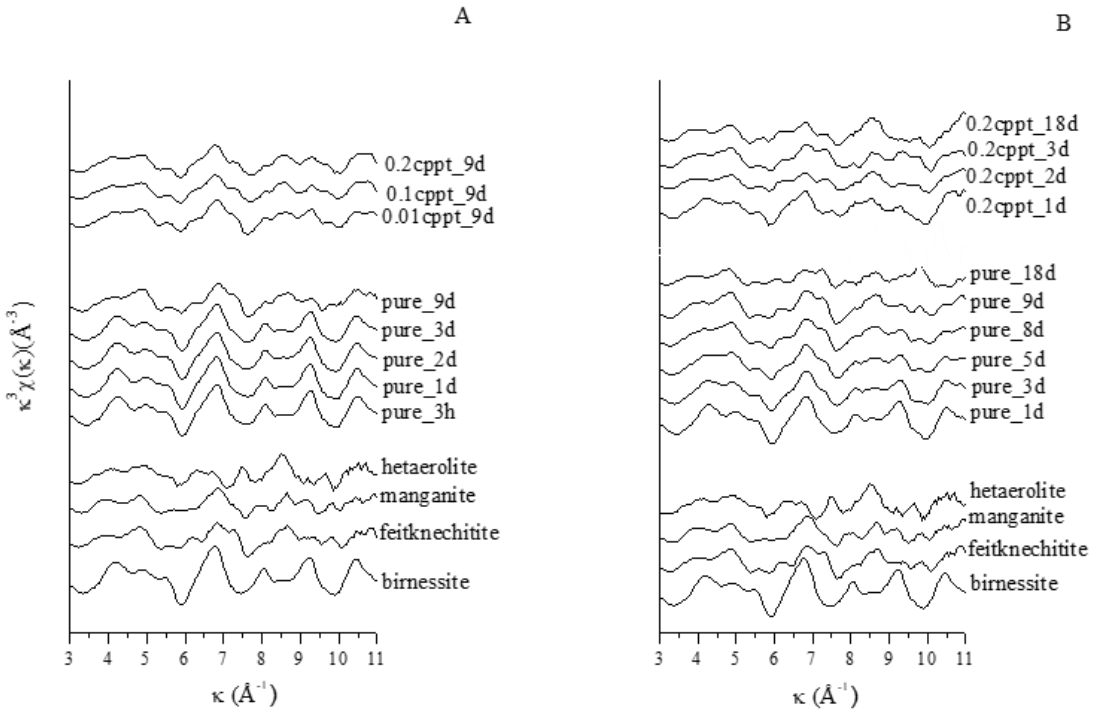

Figure C.2 k^3-weighted Mn EXAFS of pure and 0.2cppt birnessite reductive transformation products under anoxic (A) and oxic (B) conditions.

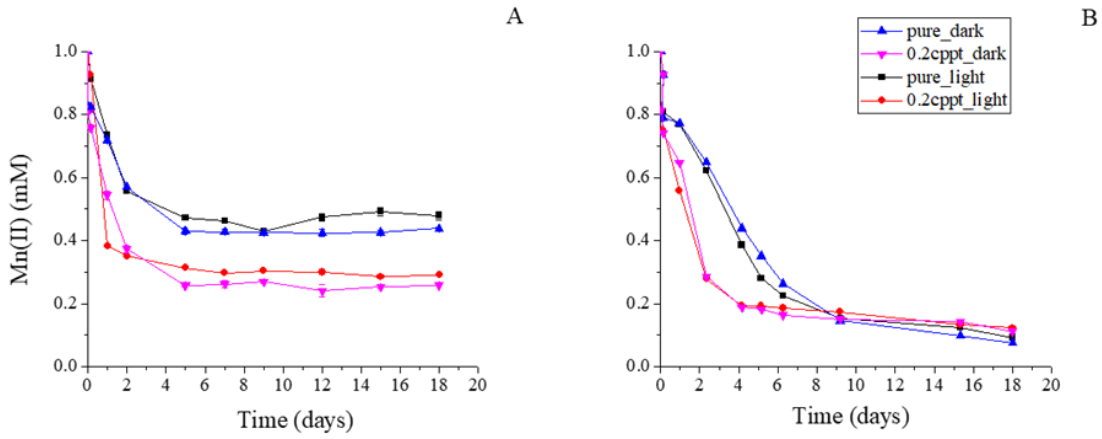

Figure C.3 Comparison of Mn^{2+} concentrations during pure and 0.2cppt acid birnessite transformation under dark and light conditions.

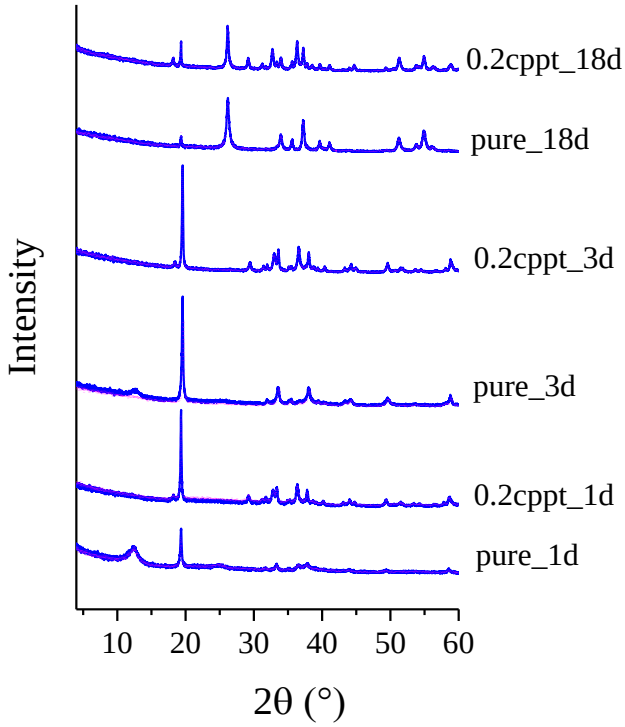

Figure C.4 Comparison of XRD spectra of pure and 0.2cppt acid birnessite anoxic transformation products under dark (blue) and light (pink) conditions. Spectra of samples with same Zn contents and reaction time but different amount of light were overlapping each other to better show the difference.

Table C.1 Linear combination fitting results of Zn EXAFS data on the 0.2cppt birnessite transformation products.

Reaction time (days)	Zn_birnessite (%)	Hetaerolite (%)	R factor	χ^2
0	100	0	0.09	6
0.125	34	66	0.09	5
1	23	77	0.08	6
3	13	87	0.10	11
5	10	90	0.07	6
7	4	96	0.15	39
9	0	100	0.09	6

REFERENCES

1. Taylor, R., R. McKenzie, and K. Norrish, *The mineralogy and chemistry of manganese in some Australian soils.* Soil Research, 1964. **2**(2): p. 235-248.

2. Manceau, A., B. Lanson, and V.A. Drits, *Structure of heavy metal sorbed birnessite. Part III: Results from powder and polarized extended X-ray absorption fine structure spectroscopy.* Geochimica et Cosmochimica Acta, 2002. **66**(15): p. 2639-2663.

3. Huang, P., *Kinetics of redox reactions on manganese oxides and its impact on environmental quality.* Rates of Soil Chemical Processes, 1991(ratesofsoilchem): p. 191-230.

4. Kawashima, M., et al, *Phosphate adsorption onto hydrous manganese (IV) oxide in the presence of divalent cations.* Water research, 1986. **20**(4): p. 471-475.

5. Gadde, R.R. and H.A. Laitinen, *Heavy metal adsorption by hydrous iron and manganese oxides.* Analytical Chemistry, 1974. **46**(13): p. 2022-2026.

6. Nico, P.S. and R.J. Zasoski, *Importance of Mn (III) availability on the rate of Cr (III) oxidation on δ-MnO2.* Environmental science & technology, 2000. **34**(16): p. 3363-3367.

7. Li, H., et al, *Structure and properties of Co-doped cryptomelane and its enhanced removal of Pb 2+ and Cr 3+ from wastewater.* Journal of Environmental Sciences, 2015. **34**: p. 77-85.

8. Manceau, A., M. Lanson, and N. Geoffroy, *Natural speciation of Ni, Zn, Ba, and As in ferromanganese coatings on quartz using X-ray fluorescence, absorption, and diffraction.* Geochimica et Cosmochimica Acta, 2007. **71**(1): p. 95-128.

9. Chang, Y.-Y., J.-W. Lim, and J.-K. Yang, *Removal of As(V) and Cr(VI) in aqueous solution by sand media simultaneously coated with Fe and Mn oxides.* Journal of Industrial and Engineering Chemistry, 2012. **18**(1): p. 188-192.

10. Stone, A.T. and J.J. Morgan, *Reduction and dissolution of manganese (III) and manganese (IV) oxides by organics. 1. Reaction with hydroquinone.* Environmental science & technology, 1984. **18**(6): p. 450-456.

11. Kung, K. and M. McBride, *Electron transfer processes between hydroquinone and hausmannite (Mn3O4).* Clays Clay Miner, 1988. **36**: p. 297-302.

12. Lee, S.H., et al, *Single-Step Synthesis, Characterization, and Application of Nanostructured K x Mn1-y Co y O2-δ with Controllable Chemical Compositions and Crystal Structures.* Chemistry of Materials, 2007. **19**(20): p. 5010-5017.

13. Poizot, P., et al, *Nano-sized transition-metal oxides as negative-electrode materials for lithium-ion batteries.* Nature, 2000. **407**(6803): p. 496-499.

14. Yin, H., et al, *Characterization of Co-doped birnessites and application for removal of lead and arsenite.* Journal of hazardous materials, 2011. **188**(1): p. 341-349.

15. Li, W.N., et al, *Hydrothermal Synthesis of Structure11. s and application for removal of lead and arsenite.es.δ with Controllable C* Advanced Functional Materials, 2006. **16**(9): p. 1247-1253.

16. Zhu, M., *Structure and reactivity study of biotic and abiotic poorly crystalline manganese oxides*. 2010: University of Delaware.

17. Bock, C.W., et al, *Manganese as a replacement for magnesium and zinc: functional comparison of the divalent ions.* Journal of the American Chemical Society, 1999. **121**(32): p. 7360-7372.

18. Tebo, B.M., et al, *Biogenic manganese oxides: properties and mechanisms of formation.* Annu. Rev. Earth Planet. Sci., 2004. **32**: p. 287-328.

19. Drits, V.A., et al, *Structure of synthetic monoclinic Na-rich birnessite and hexagonal birnessite: I. Results from X-ray diffraction and selected-area electron diffraction.* American Mineralogist, 1997. **82**(9): p. 946-961.

20. McKenzie, R., *The surface charge on manganese dioxides.* Soil Research, 1981. **19**(1): p. 41-50.

21. Luther, G., D.T. Ruppel, and C. Burkhard. *Reactivity of dissolved Mn (III) complexes and Mn (IV) species with reductants: Mn redox chemistry without a dissolution step?* in *ACS Symposium Series*. 1998. American Chemical Society.

22. Lanson, B., et al, *Structure of H-exchanged hexagonal birnessite and its mechanism of formation from Na-rich monoclinic buserite at low pH.* American Mineralogist, 2000. **85**(5-6): p. 826-838.

23. Klewicki, J.K. and J.J. Morgan, *Kinetic behavior of Mn (III) complexes of pyrophosphate, EDTA, and citrate.* Environmental science & technology, 1998. **32**(19): p. 2916-2922.

24. Villalobos, M., et al, *Structural model for the biogenic Mn oxide produced by Pseudomonas putida.* American Mineralogist, 2006. **91**(4): p. 489-502.

25. Bargar, J.R., et al, *Biotic and abiotic products of Mn (II) oxidation by spores of the marine Bacillus sp. strain SG-1.* American Mineralogist, 2005. **90**(1): p. 143-154.

26. Zhao, H., et al, *Redox Reactions between Mn (II) and Hexagonal Birnessite Change its Layer Symmetry.* Environmental science & technology, 2016.

27. Post, J.E., *Manganese oxide minerals: Crystal structures and economic and environmental significance.* Proceedings of the National Academy of Sciences, 1999. **96**(7): p. 3447-3454.

28. Zhu, M., et al, *Structural study of biotic and abiotic poorly-crystalline manganese oxides using atomic pair distribution function analysis.* Geochimica et Cosmochimica Acta, 2012. **81**(0): p. 39-55.

29. Spiro, T.G., et al, *Bacteriogenic manganese oxides.* Accounts of chemical research, 2009. **43**(1): p. 2-9.

30. Jung, H., et al, *Photochemically-assisted Synthesis of Birnessite Nanosheets and Their Structural Alteration in the Presence of Pyrophosphate.* ACS Sustainable Chemistry & Engineering, 2017.

31. Von Langen, P.J., et al, *Oxidation kinetics of manganese (II) in seawater at nanomolar concentrations.* Geochimica et Cosmochimica Acta, 1997. **61**(23): p. 4945-4954.

32. Zhu, M., et al, *Structural study of biotic and abiotic poorly-crystalline manganese oxides using atomic pair distribution function analysis.* Geochimica et Cosmochimica Acta, 2012. **81**: p. 39-55.

33. Tebo, B.M., et al, *Geomicrobiology of manganese(II) oxidation.* Trends Microbiol, 2005. **13**(9): p. 421-8.

34. Villalobos, M., et al, *Characterization of the manganese oxide produced by Pseudomonas putida strain MnB1*. Geochimica et Cosmochimica Acta, 2003. **67**(14): p. 2649-2662.

35. Coughlin, R.W. and I. Matsui, *Catalytic oxidation of aqueous Mn (II).* Journal of Catalysis, 1976. **41**(1): p. 108-123.

36. Learman, D., et al, *Formation of manganese oxides by bacterially generated superoxide.* Nature Geoscience, 2011. **4**(2): p. 95-98.

37. Learman, D.R., et al, *Coupled biotic–abiotic Mn(II) oxidation pathway mediates the formation and structural evolution of biogenic Mn oxides.* Geochimica et Cosmochimica Acta, 2011. **75**(20): p. 6048-6063.

38. Davies, S.H. and J.J. Morgan, *Manganese (II) oxidation kinetics on metal oxide surfaces.* Journal of Colloid and Interface Science, 1989. **129**(1): p. 63-77.

39. Murray, J.W., et al, *Oxidation of Mn (II): Initial mineralogy, oxidation state and ageing.* Geochimica et Cosmochimica Acta, 1985. **49**(2): p. 463-470.

40. Luther III, G.W., *Manganese (II) oxidation and Mn (IV) reduction in the environment—two one-electron transfer steps versus a single two-electron step.* Geomicrobiology Journal, 2005. **22**(3-4): p. 195-203.

41. Bargar, J.R., B.M. Tebo, and J.E. Villinski, *In situ characterization of Mn (II) oxidation by spores of the marine Bacillus sp. strain SG-1.* Geochimica et Cosmochimica Acta, 2000. **64**(16): p. 2775-2778.

42. Saratovsky, I., S.J. Gurr, and M.A. Hayward, *The structure of manganese oxide formed by the fungus Acremonium sp. strain KR21-2.* Geochimica et Cosmochimica Acta, 2009. **73**(11): p. 3291-3300.

43. Haack, E.A. and L.A. Warren, *Biofilm hydrous manganese oxyhydroxides and metal dynamics in acid rock drainage.* Environmental science & technology, 2003. **37**(18): p. 4138-4147.

44. Campbell, A.C., et al, *Manganese geochemistry in the Guaymas Basin, Gulf of California.* Geochimica et Cosmochimica Acta, 1988. **52**(2): p. 345-357.

45. Brouwers, G., et al, *Stimulation of Mn2+ oxidation in Leptothrix discophora SS-1 by Cu2+ and sequence analysis of the region flanking the gene encoding putative multicopper oxidase MofA.* Geomicrobiology Journal, 2000. **17**(1): p. 25-33.

46. De Vrind, J., et al, *The Cytochrome c Maturation Operon Is Involved in Manganese Oxidation in Pseudomonas putidaGB-1.* Applied and environmental microbiology, 1998. **64**(10): p. 3556-3562.

47. Mandernack, K.W., J. Post, and B.M. Tebo, *Manganese mineral formation by bacterial spores of the marine Bacillus, strain SG-1: evidence for the direct oxidation of Mn (II) to Mn (IV).* Geochimica et Cosmochimica Acta, 1995. **59**(21): p. 4393-4408.

48. Murray, K.J., et al, *Indirect oxidation of Co(II) in the presence of the marine Mn(II)-oxidizing bacterium Bacillus sp. strain SG-1.* Appl Environ Microbiol, 2007. **73**(21): p. 6905-9.

49. Nelson, Y.M., et al, *Production of biogenic Mn oxides by Leptothrix discophora SS-1 in a chemically defined growth medium and evaluation of their Pb adsorption characteristics.* Applied and Environmental Microbiology, 1999. **65**(1): p. 175-180.

50. Brouwers, G., et al, *Bacterial Mn2+ oxidizing systems and multicopper oxidases: an overview of mechanisms and functions.* Geomicrobiology Journal, 2000. **17**(1): p. 1-24.

51. Hastings, D. and S. Emerson, *Oxidation of manganese by spores of a marine Bacillus: kinetic and thermodynamic considerations.* Geochimica et Cosmochimica Acta, 1986. **50**(8): p. 1819-1824.

52. Mann, S., et al, *Oxidation of manganese and formation of Mn3O4 (hausmannite) by spore coats of a marine Bacillus sp.* Applied and environmental microbiology, 1988. **54**(8): p. 2140-2143.

53. Mandernack, K.W., et al, *Oxygen isotope analyses of chemically and microbially produced manganese oxides and manganates.* Geochimica et Cosmochimica Acta, 1995. **59**(21): p. 4409-4425.

54. Webb, S.M., et al, *Evidence for the presence of Mn (III) intermediates in the bacterial oxidation of Mn (II).* Proceedings of the National Academy of Sciences of the United States of America, 2005. **102**(15): p. 5558-5563.

55. Tang, Y., et al, *Chromium (III) oxidation by biogenic manganese oxides with varying structural ripening.* Environmental Science: Processes & Impacts, 2014. **16**(9): p. 2127-2136.

56. Learman, D.R., et al, *Formation of manganese oxides by bacterially generated superoxide.* Nature Geoscience, 2011. **4**(2): p. 95-98.

57. Webb, S., B. Tebo, and J. Bargar, *Structural characterization of biogenic Mn oxides produced in seawater by the marine Bacillus sp. strain SG-1*. American Mineralogist, 2005. **90**(8-9): p. 1342-1357.

58. Zhu, M., et al, *Cation effects on the layer structure of biogenic Mn-oxides.* Environmental science & technology, 2010. **44**(12): p. 4465-4471.

59. Webb, S., et al, *Determination of uranyl incorporation into biogenic manganese oxides using X-ray absorption spectroscopy and scattering.* Environmental science & technology, 2006. **40**(3): p. 771-777.

60. Lanson, B., et al, *Structure of synthetic Na-birnessite: Evidence for a triclinic one-layer unit cell.* American Mineralogist, 2002. **87**(11-12): p. 1662-1671.

61. Yin, H., et al, *Characterization of Ni-rich hexagonal birnessite and its geochemical effects on aqueous Pb 2+/Zn 2+ and As (III).* Geochimica et Cosmochimica Acta, 2012. **93**: p. 47-62.

62. Power, L.E., Y. Arai, and D.L. Sparks, *Zinc adsorption effects on arsenite oxidation kinetics at the birnessite-water interface*. Environmental science & technology, 2005. **39**(1): p. 181-187.

63. Villalobos, M., I.N. Escobar-Quiroz, and C. Salazar-Camacho, *The influence of particle size and structure on the sorption and oxidation behavior of birnessite: I. Adsorption of As (V) and oxidation of As (III).* Geochimica et Cosmochimica Acta, 2014. **125**: p. 564-581.

64. Drits, V.A., B. Lanson, and A.-C. Gaillot, *Birnessite polytype systematics and identiÞcation by powder X-ray diffraction.* American mineralogist, 2007. **92**(5-6): p. 771-788.

65. Post, J.E. and D.R. Veblen, *Crystal structure determinations of synthetic sodium, magnesium, and potassium birnessite using TEM and the Rietveld method.* American Mineralogist, 1990. **75**(5-6): p. 477-489.

66. Silvester, E., M. Manceau, and V.A. Drits, *Structure of synthetic monoclinic Na-rich birnessite and hexagonal birnessite: II. Results from chemical studies and EXAFS spectroscopy.* American Mineralogist, 1997. **82**: p. 962-978.

67. Post, J.E., *Manganese Oxide Minerals: Crystal Structures and Economic and Environmental Significance.* Proceedings of the National Academy of Sciences of the United States of America, 1999. **96**(7): p. 3447-3454.

68. Trivedi, P. and L. Axe, *Modeling Cd and Zn Sorption to Hydrous Metal Oxides.* Environmental Science & Technology, 2000. **34**(11): p. 2215-2223.

69. Coughlin, B.R. and A.T. Stone, *Nonreversible adsorption of divalent metal ions (MnII, CoII, NiII, CuII, and PbII) onto goethite: effects of acidification, FeII addition, and picolinic acid addition.* Environmental science & technology, 1995. **29**(9): p. 2445-2455.

70. Kraepiel, A.M., K. Keller, and F.M. Morel, *A model for metal adsorption on montmorillonite.* Journal of Colloid and Interface Science, 1999. **210**(1): p. 43-54.

71. Lothenbach, B., G. Furrer, and R. Schulin, *Immobilization of heavy metals by polynuclear aluminium and montmorillonite compounds.* Environmental Science & Technology, 1997. **31**(5): p. 1452-1462.

72. Pan, G. and P.S. Liss, *Metastable-equilibrium adsorption theory: II. Experimental.* Journal of colloid and interface science, 1998. **201**(1): p. 77-85.

73. Boonfueng, T., et al, *Zn sorption mechanisms onto sheathed Leptothrix discophora and the impact of the nanoparticulate biogenic Mn oxide coating.* Journal of colloid and interface science, 2009. **333**(2): p. 439-447.

74. Kwon, K.D., K. Refson, and G. Sposito, *Understanding the trends in transition metal sorption by vacancy sites in birnessite.* Geochimica Et Cosmochimica Acta, 2013. **101**: p. 222-232.

75. Peacock, C.L. and D.M. Sherman, *Sorption of Ni by birnessite: Equilibrium controls on Ni in seawater.* Chemical Geology, 2007. **238**(1): p. 94-106.

76. Peña, J., J.R. Bargar, and G. Sposito, *Copper sorption by the edge surfaces of synthetic birnessite nanoparticles.* Chemical Geology, 2015. **396**: p. 196-207.

77. Villalobos, M., J. Bargar, and G. Sposito, *Mechanisms of Pb (II) sorption on a biogenic manganese oxide.* Environmental science & technology, 2005. **39**(2): p. 569-576.

78. Lanson, B., et al, *Structure of heavy-metal sorbed birnessite: Part 1. Results from X-ray diffraction.* American Mineralogist, 2002. **87**(11-12): p. 1631-1645.

79. Yin, H., et al, *High Co-doping promotes the transition of birnessite layer symmetry from orthogonal to hexagonal.* Chemical Geology, 2015. **410**: p. 12-20.

80. Yin, H., et al, *Effects of Fe doping on the structures and properties of hexagonal birnessites–Comparison with Co and Ni doping.* Geochimica Et Cosmochimica Acta, 2013. **117**: p. 1-15.

81. Yin, H., et al, *Structure and properties of vanadium (V)-doped hexagonal turbostratic birnessite and its enhanced scavenging of Pb 2+ from solutions.* Journal of hazardous materials, 2015. **288**: p. 80-88.

82. Hinkle, M.A., K.G. Dye, and J.G. Catalano, *Impact of Mn (II)-Manganese Oxide Reactions on Ni and Zn Speciation.* Environmental Science & Technology, 2017. **51**(6): p. 3187-3196.

83. Chen, X., et al, *Characterization of manganese oxide octahedral molecular sieve (M-OMS-2) materials with different metal cation dopants.* Chemistry of materials, 2002. **14**(2): p. 940-948.

84. Yu, Q., et al, *Zinc sorption during bio-oxidation and precipitation of manganese modifies the layer stacking of biogenic birnessite.* Geomicrobiology Journal, 2013. **30**(9): p. 829-839.

85. Chang, J., et al, *Zn (II) sequestration by fungal biogenic manganese oxide through enzymatic and abiotic processes.* Chemical Geology, 2014. **383**: p. 155-163.

86. Wang, Y. and A.T. Stone, *Reaction of Mn< sup> III, IV</sup>(hydr) oxides with oxalic acid, glyoxylic acid, phosphonoformic acid, and structurally-related organic compounds.* Geochimica et cosmochimica acta, 2006. **70**(17): p. 4477-4490.

87. Stone, A.T. and J.J. Morgan, *Reduction and dissolution of manganese (III) and manganese (IV) oxides by organics: 2. Survey of the reactivity of organics.* Environmental Science & Technology, 1984. **18**(8): p. 617-624.

88. Stone, A.T., *Reductive dissolution of manganese (III/IV) oxides by substituted phenols.* Environmental science & technology, 1987. **21**(10): p. 979-988.

89. Thamdrup, B., *Bacterial manganese and iron reduction in aquatic sediments*, in *Advances in microbial ecology*. 2000, Springer. p. 41-84.

90. Postma, D., *Concentration of Mn and separation from Fe in sediments—I. Kinetics and stoichiometry of the reaction between birnessite and dissolved Fe (II) at 10 C.* Geochimica et Cosmochimica Acta, 1985. **49**(4): p. 1023-1033.

91. Tu, S., G.J. Racz, and T.B. Goh, *Transformations of synthetic birnessite as affected by pH and manganese concentration.* Clays and Clay Minerals, 1994. **42**(3): p. 321-330.

92. Wang, Q., P. Yang, and M. Zhu, *Structural Transformation of Birnessite by Fulvic Acid under Anoxic Conditions.* Environmental Science & Technology, 2018.

93. Peña, J., et al, *Dissolution of hausmannite (Mn3O4) in the presence of the trihydroxamate siderophore desferrioxamine B.* Geochimica et Cosmochimica Acta, 2007. **71**(23): p. 5661-5671.

94. De Schamphelaire, L., et al, *Minireview: The potential of enhanced manganese redox cycling for sediment oxidation.* Geomicrobiology Journal, 2007. **24**(7-8): p. 547-558.

95. Dai, R., et al, *A comparative study of oxidation of Cr (III) in aqueous ions, complex ions and insoluble compounds by manganese-bearing mineral (birnessite).* Chemosphere, 2009. **76**(4): p. 536-541.

96. FENDORF, S.E., et al, *Inhibitory Mechanisms of Cr (lll) Oxidation by< 5-Mn02.* Journal of Colloid and Interface Science, 1992. **153**(1).

97. Eary, L.E. and D. Rai, *Kinetics of chromium (III) oxidation to chromium (VI) by reaction with manganese dioxide.* Environmental Science & Technology, 1987. **21**(12): p. 1187-1193.

98. Banerjee, D. and H. Nesbitt, *Oxidation of aqueous Cr (III) at birnessite surfaces: Constraints on reaction mechanism.* Geochimica et Cosmochimica Acta, 1999. **63**(11): p. 1671-1687.

99. McCarty, K.M., H.T. Hanh, and K.W. Kim, *Arsenic geochemistry and human health in South East Asia.* Reviews on Environmental Health, 2011. **26**(1): p. 71-78.

100. Luther, G.W., *Manganese(II) Oxidation and Mn(IV) Reduction in the Environment—Two One-Electron Transfer Steps Versus a Single Two-Electron Step.* Geomicrobiology Journal, 2005. **22**(3-4): p. 195-203.

101. Duarte, G., et al *As(III) sorption on iron and aluminum oxy-hydroxide and the implications for arsenic mobility*. 2010.

102. Bissen, M. and F.H. Frimmel, *Arsenic—a review. Part II: oxidation of arsenic and its removal in water treatment.* Acta hydrochimica et hydrobiologica, 2003. **31**(2): p. 97-107.

103. al, S.P.e., *Advances in the treatment of arsenic pollution by environmental mineral materials.* ACTA PET ROLOGICA ET MINERALOGICA, 2008. **27**(3).

104. Fendorf, S.E. and R.J. Zasoski, *Chromium (III) oxidation by. delta.-manganese oxide (MnO2). 1. Characterization.* Environmental Science & Technology, 1992. **26**(1): p. 79-85.

105. Landrot, G., et al, *Chromium(III) oxidation by three poorly-crystalline manganese(IV) oxides. 1. Chromium(III)-oxidizing capacity.* Environ Sci Technol, 2012. **46**(21): p. 11594-600.

106. Yin, H., et al, *Co 2+-exchange mechanism of birnessite and its application for the removal of Pb 2+ and As (III).* Journal of hazardous materials, 2011. **196**: p. 318-326.

107. Kamimura, A., et al, *Oxidation of benzyl alcohols by semi-stoichiometric amounts of cobalt-doped birnessite-type layered MnO 2 under oxygen atmosphere.* Rsc Advances, 2013. **3**(2): p. 468-472.

108. Grangeon, S., et al, *Crystal structure of Ni-sorbed synthetic vernadite: a powder X-ray diffraction study.* Mineralogical Magazine, 2008. **72**(6): p. 1279-1291.

109. Grangeon, S., et al, *Zn sorption modifies dynamically the layer and interlayer structure of vernadite.* Geochimica et Cosmochimica Acta, 2012. **85**: p. 302-313.

110. Lefkowitz, J.P., A.A. Rouff, and E.J. Elzinga, *Influence of pH on the reductive transformation of birnessite by aqueous Mn (II).* Environmental science & technology, 2013. **47**(18): p. 10364-10371.

111. Lefkowitz, J.P. and E.J. Elzinga, *Impacts of Aqueous Mn (II) on the Sorption of Zn (II) by Hexagonal Birnessite.* Environmental science & technology, 2015. **49**(8): p. 4886-4893.

112. Elzinga, E.J., *Reductive transformation of birnessite by aqueous Mn (II).* Environmental science & technology, 2011. **45**(15): p. 6366-6372.

113. Cui, H., et al, *Aging promotes todorokite formation from layered manganese oxide at near-surface conditions.* Journal of soils and sediments, 2010. **10**(8): p. 1540-1547.

114. Polverejan, M., J.C. Villegas, and S.L. Suib, *Higher valency ion substitution into the manganese oxide framework.* Journal of the American Chemical Society, 2004. **126**(25): p. 7774-7775.

115. Liu, L., et al, *Influence of vanadium doping on the supercapacitance performance of hexagonal birnessite.* Journal of Power Sources, 2015. **277**: p. 26-35.

116. Yin, H., et al, *Characterization of Ni-rich hexagonal birnessite and its geochemical effects on aqueous Pb2+/Zn2+ and As(III).* Geochimica et Cosmochimica Acta, 2012. **93**: p. 47-62.

117. Drits, V.A., et al, *Structure of heavy-metal sorbed birnessite: Part 2. Results from electron diffraction.* American Mineralogist, 2002. **87**(11-12): p. 1646-1661.

118. Jenkyns, H.C., *Fossil manganese nodules from the west Sicilian Jurassic.* Eclogae Geologicae Helvetiae, 1970. **63**(3): p. 741-774.

119. Childs, C.W., *Composition of iron-manganese concretions from some New Zealand soils.* Geoderma, 1975. **13**(2): p. 141-152.

120. Manceau, A., et al, *Molecular-scale speciation of Zn and Ni in soil ferromanganese nodules from loess soils of the Mississippi Basin.* Environmental Science & Technology, 2003. **37**(1): p. 75-80.

121. Tan, H., et al, *Characterization of manganese oxide precipitates from Appalachian coal mine drainage treatment systems.* Applied Geochemistry, 2010. **25**(3): p. 389-399.

122. Lanson, B., et al, *Formation of Zn–Ca phyllomanganate nanoparticles in grass roots.* Geochimica et Cosmochimica Acta, 2008. **72**(10): p. 2478-2490.

123. Meng, Y.-T., et al, *Biogenic Mn oxides for effective adsorption of Cd from aquatic environment.* Environmental Pollution, 2009. **157**(8): p. 2577-2583.

124. Dong, D., Y. Li, and X. Hua, *Investigation of Fe, Mn oxides and organic material in surface coatings and Pb, Cd adsorption to surface coatings developed in different natural waters.* Microchemical Journal, 2001. **70**(1): p. 25-33.

125. Yao, W. and F.J. Millero, *Adsorption of Phosphate on Manganese Dioxide in Seawater.* Environmental Science & Technology, 1996. **30**(2): p. 536-541.

126. Violante, A. and M. Pigna, *Competitive sorption of arsenate and phosphate on different clay minerals and soils.* Soil Science Society of America Journal, 2002. **66**(6): p. 1788-1796.

127. Liu, F., A. De Cristofaro, and A. Violante, *Effect of pH, phosphate and oxalate on the adsorption/desorption of arsenate on/from goethite.* Soil Science, 2001. **166**(3): p. 197-208.

128. Baldwin, D.S., et al, *Hydrolysis of an organophosphate ester by manganese dioxide.* Environmental science & technology, 2001. **35**(4): p. 713-716.

129. Watanabe, J.i., et al, *Concurrent sorption of As (V) and Mn (II) during biogenic manganese oxide formation.* Chemical Geology, 2012. **306**: p. 123-128.

130. Marcus, M.A., A. Manceau, and M. Kersten, *Mn, Fe, Zn and As speciation in a fast-growing ferromanganese marine nodule.* Geochimica et Cosmochimica Acta, 2004. **68**(14): p. 3125-3136.

131. Bodeï S., et al, *Formation of todorokite from vernadite in Ni-rich hemipelagic sediments.* Geochimica et Cosmochimica Acta, 2007. **71**(23): p. 5698-5716.

132. Bargar, J.R., et al, *Structural characterization of terrestrial microbial Mn oxides from Pinal Creek, AZ.* Geochimica et Cosmochimica Acta, 2009. **73**(4): p. 889-910.

133. Peña, J., et al, *Mechanisms of nickel sorption by a bacteriogenic birnessite.* Geochimica et Cosmochimica Acta, 2010. **74**(11): p. 3076-3089.

134. Simanova, A.A., et al, *Probing the sorption reactivity of the edge surfaces in birnessite nanoparticles using nickel (II).* Geochimica et Cosmochimica Acta, 2015.

135. Hinkle, M.A., K.G. Dye, and J.G. Catalano, *Impact of Mn (II)-Manganese Oxide Reactions on Ni and Zn Speciation.* Environmental Science & Technology, 2017.

136. Yin, H., et al, *Effects of Co and Ni co-doping on the structure and reactivity of hexagonal birnessite.* Chemical Geology, 2014. **381**: p. 10-20.

137. Yin, H., et al, *Fe-doped cryptomelane synthesized by refluxing at atmosphere: Structure, properties and photocatalytic degradation of phenol.* Journal of hazardous materials, 2015. **296**: p. 221-229.

138. Wang, Q., et al, *Synthesis of Birnessite in the Presence of Phosphate, Silicate, or Sulfate.* Inorganic Chemistry, 2016.

139. Toner, B., et al, *Zinc sorption to biogenic hexagonal-birnessite particles within a hydrated bacterial biofilm.* Geochimica et Cosmochimica Acta, 2006. **70**(1): p. 27-43.

140. Trivedi, P., L. Axe, and T.A. Tyson, *XAS Studies of Ni and Zn Sorbed to Hydrous Manganese Oxide.* Environmental Science & Technology, 2001. **35**(22): p. 4515-4521.

141. Zhu, M., et al, *Structural study of biotic and abiotic poorly-crystalline manganese oxides using atomic pair distribution function analysis.* Geochimica et Cosmochimica Acta, 2012. **81**: p. 39-55.

142. Kwon, K.D., K. Refson, and G. Sposito, *Zinc surface complexes on birnessite: A density functional theory study.* Geochimica et Cosmochimica Acta, 2009. **73**(5): p. 1273-1284.

143. Webb, S.M., *SIXpack: a graphical user interface for XAS analysis using IFEFFIT.* Physica Scripta, 2005. **T115**: p. 1011-1014.

144. Ravel, B. and M. Newville, *ATHENA, ARTEMIS, HEPHAESTUS: data analysis for X-ray absorption spectroscopy using IFEFFIT.* Journal of Synchrotron Radiation, 2005. **12**: p. 537-541.

145. Ressler, T., *WinXAS: a program for X-ray absorption spectroscopy data analysis under MS-Windows.* Journal of synchrotron radiation, 1998. **5**(2): p. 118-122.

146. Manceau, A., M.A. Marcus, and S. Grangeon, *Determination of Mn valence states in mixed-valent manganates by XANES spectroscopy.* American Mineralogist, 2012. **97**(5-6): p. 816-827.

147. Cismasu, A.C., et al, *Composition and structural aspects of naturally occurring ferrihydrite.* Comptes Rendus Geoscience, 2011. **343**(2): p. 210-218.

148. Patil, S., et al, *Protein adsorption and cellular uptake of cerium oxide nanoparticles as a function of zeta potential.* Biomaterials, 2007. **28**(31): p. 4600-4607.

149. Drits, V.A., B. Lanson, and A.-C. Gaillot, *Birnessite polytype systematics and identification by powder X-ray diffraction.* American mineralogist, 2007. **92**(5-6): p. 771-788.

150. Jürgensen, A., et al, *The structure of the manganese oxide on the sheath of the bacterium Leptothrix discophora: An XAFS study.* American Mineralogist, 2004. **89**(7): p. 1110-1118.

151. Wang, Y., et al, *Sorption behavior of heavy metals on birnessite: Relationship with its Mn average oxidation state and implications for types of sorption sites.* Chemical Geology, 2012. **292–293**(0): p. 25-34.

152. Manceau, A., et al, *Natural speciation of Zn at the micrometer scale in a clayey soil using X-ray fluorescence, absorption, and diffraction.* Geochimica et Cosmochimica Acta, 2004. **68**(11): p. 2467-2483.

153. Saratovsky, I., et al, *Manganese oxides: parallels between abiotic and biotic structures.* Journal of the American Chemical Society, 2006. **128**(34): p. 11188-11198.

154. Sherman, D.M. and C.L. Peacock, *Surface complexation of Cu on birnessite (δ-MnO 2): controls on Cu in the deep ocean.* Geochimica et Cosmochimica Acta, 2010. **74**(23): p. 6721-6730.

155. Shannon, R.t., *Revised effective ionic radii and systematic studies of interatomic distances in halides and chalcogenides.* Acta Crystallographica Section A: Crystal Physics, Diffraction, Theoretical and General Crystallography, 1976. **32**(5): p. 751-767.

156. Johnson, E.A. and J.E. Post, *Water in the interlayer region of birnessite: Importance in cation exchange and structural stability.* American Mineralogist, 2006. **91**(4): p. 609-618.

157. Grangeon, S., B. Lanson, and M. Lanson, *Solid-state transformation of nanocrystalline phyllomanganate into tectomanganate: influence of initial layer and interlayer structure.* Acta Crystallographica Section B: Structural Science, Crystal Engineering and Materials, 2014. **70**(5): p. 828-838.

158. Gao, Q., et al, *Preparation of Nanometer-Sized Manganese Oxides by Intercalation of Organic Ammonium Ions in Synthetic Birnessite OL-1*. Chemistry of Materials, 2001. **13**(3): p. 778-786.

159. Li, Y.R., et al, *Synthesis of Copper Birnessite, CuxMnOy ·nH2O with Crystallite Size Control: Impact of Crystallite Size on Electrochemistry*. Journal of The Electrochemical Society, 2016. **163**(2): p. A281-A285.

160. Villalobos, M., et al, *The influence of particle size and structure on the sorption and oxidation behaviour of birnessite: II. Adsorption and oxidation of four polycyclic aromatic hydrocarbons.* Environmental Chemistry, 2014. **11**(3): p. 279-288.

161. Zhang, H., et al, *Size-dependent bandgap of nanogoethite.* The Journal of Physical Chemistry C, 2011. **115**(36): p. 17704-17710.

162. Hammersley, A., et al, *Two-dimensional detector software: from real detector to idealised image or two-theta scan.* International Journal of High Pressure Research, 1996. **14**(4-6): p. 235-248.

163. Wang, Y., et al, *Sorption behavior of heavy metals on birnessite: relationship with its Mn average oxidation state and implications for types of sorption sites.* Chemical Geology, 2012. **292**: p. 25-34.

164. Zhao, W., et al, *Pb2+ adsorption on birnessite affected by Zn2+ and Mn2+ pretreatments.* Journal of Soils and Sediments, 2010. **10**(5): p. 870-878.

165. Lucht, K.P. and J.L. Mendoza-Cortes, *Birnessite: A Layered Manganese Oxide To Capture Sunlight for Water-Splitting Catalysis.* The Journal of Physical Chemistry C, 2015. **119**(40): p. 22838-22846.

166. Kang, Q., et al, *Effect of Interlayer Spacing on the Activity of Layered Manganese Oxide Bilayer Catalysts for the Oxygen Evolution Reaction.* Journal of the American Chemical Society, 2017.

167. Jenne, E.A., *Controls on Mn, Fe, Co, Ni, Cu, and Zn concentrations in soils and water: the significant role of hydrous Mn and Fe oxides.* ADVANCES IN CHEM SER, NO 73, PP 337-387, 1968. 51 P, 6 FIG, 1 TAB, 257 REF., 1968.

168. Manceau, A., et al, *Structural mechanism of Co2+ oxidation by the phyllomanganate buserite.* American Mineralogist, 1997. **82**(11-12): p. 1150-1175.

169. Manceau, A., S. Llorca, and G. Calas, *Crystal chemistry of cobalt and nickel in lithiophorite and asbolane from New Caledonia.* Geochimica et Cosmochimica Acta, 1987. **51**(1): p. 105-113.

170. Kwon, K.D., K. Refson, and G. Sposito, *Surface complexation of Pb (II) by hexagonal birnessite nanoparticles.* Geochimica et Cosmochimica Acta, 2010. **74**(23): p. 6731-6740.

171. Tripathy, S.S., J.-L. Bersillon, and K. Gopal, *Adsorption of Cd2+ on hydrous manganese dioxide from aqueous solutions.* Desalination, 2006. **194**(1–3): p. 11-21.

172. Kawashima, M., et al, *Phosphate adsorption onto hydrous manganese(IV) oxide in the presence of divalent cations.* Water Research, 1986. **20**(4): p. 471-475.

173. Qin, Z., et al, *Local structure of Cu 2+ in Cu-doped hexagonal turbostratic birnessite and Cu 2+ stability under acid treatment.* Chemical Geology, 2017.

174. Zhao, S., et al, *Effect of Zn2+ presence during mineral formation on the structure of layered Mn oxides*, in *Chemical Geology*.

175. Murphy, J. and J. Riley, *A modified single solution method for determination of phosphate uptake by rye.* Soil Sci. Soc. Amer. Proc. 48, 1952: p. 31-36.

176. Lenoble, V., et al, *Arsenite oxidation and arsenate determination by the molybdene blue method.* Talanta, 2003. **61**(3): p. 267-276.

177. Balistrieri, L.S. and T. Chao, *Adsorption of selenium by amorphous iron oxyhydroxide and manganese dioxide.* Geochimica et Cosmochimica Acta, 1990. **54**(3): p. 739-751.

178. Mustafa, S., M.I. Zaman, and S. Khan, *pH effect on phosphate sorption by crystalline MnO 2.* Journal of colloid and interface science, 2006. **301**(2): p. 370-375.

179. Mustafa, S., M.I. Zaman, and S. Khan, *Temperature effect on the mechanism of phosphate anions sorption by β-MnO 2.* Chemical Engineering Journal, 2008. **141**(1): p. 51-57.

180. Ouvrard, S., M.-O. Simonnot, and M. Sardin, *Reactive behavior of natural manganese oxides toward the adsorption of phosphate and arsenate.* Industrial & engineering chemistry research, 2002. **41**(11): p. 2785-2791.

181. Sparks, D.L., *Evrionmental Soil Chemistru*. 2002: Academic Press.

182. Manning, B.A., et al, *Arsenic (III) oxidation and arsenic (V) adsorption reactions on synthetic birnessite.* Environmental Science & Technology, 2002. **36**(5): p. 976-981.

183. Deschamps, E., et al, *Arsenic sorption onto soils enriched in Mn and Fe minerals.* Clays and Clay Minerals, 2003. **51**(2): p. 197-204.

184. Lafferty, B.J., et al, *Arsenite oxidation by a poorly crystalline manganese-oxide. 2. Results from X-ray absorption spectroscopy and X-ray diffraction.* Environmental science & technology, 2010. **44**(22): p. 8467-8472.

185. Zeng, L., X. Li, and J. Liu, *Adsorptive removal of phosphate from aqueous solutions using iron oxide tailings.* Water Research, 2004. **38**(5): p. 1318-1326.

186. Tanada, S., et al, *Removal of phosphate by aluminum oxide hydroxide.* Journal of colloid and interface science, 2003. **257**(1): p. 135-140.

187. Dixit, S. and J.G. Hering, *Comparison of arsenic (V) and arsenic (III) sorption onto iron oxide minerals: implications for arsenic mobility.* Environmental science & technology, 2003. **37**(18): p. 4182-4189.

188. Takamatsu, T., M. Kawashima, and M. Koyama, *The role of Mn2+-rich hydrous manganese oxide in the accumulation of arsenic in lake sediments.* Water Research, 1985. **19**(8): p. 1029-1032.

189. Zhu, M., et al, *Quantum chemical study of arsenic (III, V) adsorption on Mn-oxides: Implications for arsenic (III) oxidation.* Environmental science & technology, 2009. **43**(17): p. 6655-6661.

190. Madison, A.S., B.M. Tebo, and G.W. Luther, *Simultaneous determination of soluble manganese (III), manganese (II) and total manganese in natural (pore) waters.* Talanta, 2011. **84**(2): p. 374-381.

191. Ravel, B. and M. Newville, *ATHENA, ARTEMIS, HEPHAESTUS: data analysis for X-ray absorption spectroscopy using IFEFFIT.* Journal of synchrotron radiation, 2005. **12**(4): p. 537-541.

192. Elzinga, E.J. and A.B. Kustka, *A Mn-54 radiotracer study of Mn isotope solid–liquid exchange during reductive transformation of vernadite (δ-MnO2) by aqueous Mn (II).* Environmental science & technology, 2015. **49**(7): p. 4310-4316.

193. Kim, S.C. and W.G. Shim, *Catalytic combustion of VOCs over a series of manganese oxide catalysts.* Applied Catalysis B: Environmental, 2010. **98**(3): p. 180-185.

194. Subbaraman, R., et al, *Trends in activity for the water electrolyser reactions on 3d M (Ni, Co, Fe, Mn) hydr (oxy) oxide catalysts.* Nature materials, 2012. **11**(6): p. 550-557.

195. Kang, Q., et al, *Effect of Interlayer Spacing on the Activity of Layered Manganese Oxide Bilayer Catalysts for the Oxygen Evolution Reaction.* Journal of the American Chemical Society, 2017. **139**(5): p. 1863-1870.

196. Lin, R., et al, *Catalyst characterization and activity of Ag–Mn complex oxides.* Applied Catalysis A: General, 2001. **220**(1): p. 165-171.

197. Kang, M., et al, *Cu–Mn mixed oxides for low temperature NO reduction with NH 3.* Catalysis Today, 2006. **111**(3): p. 236-241.

198. Li, Y.-F., S.-C. Zhu, and Z.-P. Liu, *Reaction network of layer-to-tunnel transition of MnO2.* Journal of the American Chemical Society, 2016. **138**(16): p. 5371-5379.

199. Lefkowitz, J.P. and E.J. Elzinga, *Structural alteration of hexagonal birnessite by aqueous Mn (II): Impacts on Ni (II) sorption.* Chemical Geology, 2017. **466**: p. 524-532.

200. Cornell, R., *The influence of some divalent cations on the transformation of ferrihydrite to more crystalline products.* Clay Minerals, 1988. **23**(3): p. 329-332.

201. Ebinger, M. and D. Schulze, *The influence of pH on the synthesis of mixed Fe-Mn oxide minerals.* Clay Minerals, 1990. **25**(4): p. 507-518.

202. Ford, R.G., K. Kemner, and P.M. Bertsch, *Influence of sorbate-sorbent interactions on the crystallization kinetics of nickel-and lead-ferrihydrite coprecipitates.* Geochimica et Cosmochimica Acta, 1999. **63**(1): p. 39-48.

203. Giovanoli, R. and R.M. Cornell, *Crystallization of metal substituted ferrihydrites.* Journal of Plant Nutrition and Soil Science, 1992. **155**(5): p. 455-460.

204. Glasby, G.P., *Manganese: predominant role of nodules and crusts*, in *Marine geochemistry*. 2006, Springer. p. 371-427.

205. Goldberg, E.D., *Marine geochemistry 1. Chemical scavengers of the sea.* The Journal of Geology, 1954: p. 249-265.

206. Fuller, C.C. and J.R. Bargar, *Processes of zinc attenuation by biogenic manganese oxides forming in the hyporheic zone of Pinal Creek, Arizona.* Environmental science & technology, 2014. **48**(4): p. 2165-2172.

207. Manceau, A., et al, *Natural speciation of Mn, Ni, and Zn at the micrometer scale in a clayey paddy soil using X-ray fluorescence, absorption, and diffraction.* Geochimica et Cosmochimica Acta, 2005. **69**(16): p. 4007-4034.

208. Aronson, B.J., et al, *Synthesis, characterization, and electrochemical properties of magnesium birnessite and zinc chalcophanite prepared by a low-temperature route.* Chemistry of materials, 1999. **11**(4): p. 949-957.

209. Zafiriou, O.C., B.M. Voelker, and D.L. Sedlak, *Chemistry of the superoxide radical (O2-) in seawater: Reactions with inorganic copper complexes.* The Journal of Physical Chemistry A, 1998. **102**(28): p. 5693-5700.

210. Voelker, B.M., D.L. Sedlak, and O.C. Zafiriou, *Chemistry of superoxide radical in seawater: Reactions with organic Cu complexes.* Environmental science & technology, 2000. **34**(6): p. 1036-1042.

211. Yin, H., et al, *Coordination geometry of Zn2+ on hexagonal turbostratic birnessites with different Mn average oxidation states and its stability under acid dissolution.* Journal of Environmental Sciences, 2017.

212. Ling, F.T., et al, *Transformations from triclinic to hexagonal birnessite at circumneutral pH induced through pH control by common biological buffers.* Chemical Geology, 2015. **416**: p. 1-10.

213. Hammersley, A., *FIT2D V9. 129 Reference Manual V3. 1.* Inter Rep ESRF98HA01, ESRF, Grenoble, 1998.

214. Qiu, X., J.W. Thompson, and S.J. Billinge, *PDFgetX2: a GUI-driven program to obtain the pair distribution function from X-ray powder diffraction data.* Journal of Applied Crystallography, 2004. **37**(4): p. 678-678.

215. Nandy, A. and S. Pradhan, *Effects of monovalent cation doping on the structure, microstructure, lattice distortion and magnetic behavior of single crystalline NdMnO 3 compounds.* Dalton Transactions, 2015. **44**(39): p. 17229-17240.

216. Feng, X.H., et al, *Adsorption and redox reactions of heavy metals on synthesized Mn oxide minerals.* Environmental Pollution, 2007. **147**(2): p. 366-373.

217. Pretorius, P.J. and P.W. Linder, *The adsorption characteristics of δ-manganese dioxide: a collection of diffuse double layer constants for the adsorption of H+, Cu2+, Ni2+, Zn2+, Cd2+ and Pb2+.* Applied Geochemistry, 2001. **16**(9): p. 1067-1082.

218. Tonkin, J.W., L.S. Balistrieri, and J.W. Murray, *Modeling sorption of divalent metal cations on hydrous manganese oxide using the diffuse double layer model.* Applied Geochemistry, 2004. **19**(1): p. 29-53.

219. Tang, X., et al, *Synthesis and capacitive property of hierarchical hollow manganese oxide nanospheres with large specific surface area.* Journal of Power Sources, 2009. **193**(2): p. 939-943.